Aerospace Applications of Noise Covariance Identification with Autocovariance Least Squares

Kimberly A. Hinson

A dissertation
submitted in partial fulfillment of the
requirements for the degree of

Doctor of Philosophy

University of Washington

2025

Reading Committee:
Kristi Morgansen, Chair
Mehran Mesbahi
Krithika Manohar

Program Authorized to Offer Degree:
Aeronautics and Astronautics

University of Washington

Abstract

Aerospace Applications of Noise Covariance Identification with Autocovariance Least Squares

Kimberly A. Hinson

Chair of the Supervisory Committee:
Professor Kristi Morgansen
Department of Aeronautics and Astronautics

State estimation is necessary to support state feedback control applications whenever measuring the full state is prevented by environment or cost. Estimator performance depends on an accurate model of the stochastic process, however in practice noise covariances are not known and are hard to determine. The Autocovariance Least Squares (ALS) technique is a direct correlation method that identifies a system's noise covariance matrices. ALS poses a least squares problem using a linear or non-linear system model and experimentally observed measurement innovations. This dissertation addresses fielded vehicles for which ALS can be used to inform the design of state estimation filters.

There are unique noise identification challenges with aerospace vehicles including the conditioning of the ALS problem, measurement of atmospheric disturbances, uncertainty in the dynamic model, and the cost and time required for data collection. Extensions of the ALS technique are developed to address these challenges. The extensions are applied to design state estimation filters for four aerospace systems for both simulated and experimentally collected data. The systems considered are the University of Washington's two gust load alleviation wind tunnel test-beds; the 3 ft × 3 ft Model for Aeroelastic Response to Gust Excitation and the Kirsten Wind Tunnel Large Wing test-bed, a simulated narrow body commercial aircraft, and flight test data from a wide body commercial aircraft.

TABLE OF CONTENTS

LIST OF FIGURES

Figure Number Page

LIST OF TABLES

Table Number Page

ACKNOWLEDGMENTS

This thesis is the culmination of years of study that was influenced and supported by many individuals. I am grateful to my advisor, Kristi Morgansen for giving me an opportunity as a non-traditional PhD student, for technical guidance and research direction, for enabling me to continue a career I love in parallel with academic growth, and for unwavering patience through life's events. Thank you to Mehran Mesbahi and Eli Livne for engineering guidance and mentorship. As a member of the Nonlinear Dynamics and Control Lab I appreciate the friendships, and community I have gained. Particular thanks to Jake Quenzer, Natalie Brace, John Berg, Eddie Ting, Brian Beechinor, Alison Zongolowicz, and Ena Hodzic.

Thank you to my colleagues at The Boeing Company on the 777X Primary Control Laws team and the KC-46 Boom Control Law team for their patience and encouragement. I am grateful for the support of my Boeing managers who have allowed me the flexibility to study as a graduate student and have remained invested in my academic and professional development. I am especially appreciative to the following individuals for their technical discussion and mentorship; Brian Rupnik, Paul Strefling, Richard Golob, Jung Soon Jang, Tristan Flanzer, Abe Pachikara, and Kioumars Najmabadi. This effort was made possible by funding from the Learning Together Program.

On a personal note, many friends and family members made space in their lives so that I could dedicate time to learning. I want to thank my Mom and Dad for a lifetime of encouragement. Thank you to Meghan Lyle for listening through every success and failure. Thank you to Gwen Lapham and Cara Chin whose support can be measured in laps of Green Lake. I deeply appreciate Hannah Yates who on numerous occasions swept my children off on adventures. Finally, I can't thank Brian enough for his steadfast love and support.

DEDICATION

to Honor, for always asking,“Why?” and to Ira, for “Already knowing”

Chapter 1

INTRODUCTION

In most applications of state feedback control, measurement of the full system state is impractical, and controller implementation must rely on state estimation. The accuracy of state estimation filtering directly impacts a dynamic system's closed loop performance, making effective and efficient design of filters essential to achieve performance specifications. Applications of state feedback control span many industries, from transportation to medicine to agriculture. In the work of this dissertation, we focus primarily on state estimation for aerospace vehicle control tasks including stability augmentation, disturbance rejection, and load alleviation. The techniques developed herein also have applications for other vehicle functions reliant on state estimation such as autonomy and path planning. The work here is particularly driven by considerations of practical implementation of estimation such as large state dimension, limited data, and unknown environmental effects. Results of the tools developed in this research will be demonstrated both for constructed data from models and for data from fielded commercial systems.

A stochastic system model is a natural choice to capture many random phenomena including vibration, turbulence, electrical noise, and acoustics. State estimation for a stochastic system requires an accurate model of the system dynamics, including the properties of the noise. Noise enters the state-space model as process noise through the state equation as a disturbance and measurement noise through the measurement equation,

$$\begin{aligned} x_{k+1} &= Ax_k + Bu_k + Gw_k \\ y_k &= Cx_k + v_k \end{aligned} \tag{1.1}$$

with state, $x_k \in \mathbb{R}^n$, control, $u_k \in \mathbb{R}^m$, process disturbance model, $G \in \mathbb{R}^{n \times g}$, process noise, $w_k \in \mathbb{R}^g$, measurements $y_k \in \mathbb{R}^p$, and measurement noise, $v_k \in \mathbb{R}^p$, as shown in Fig. 1.1.

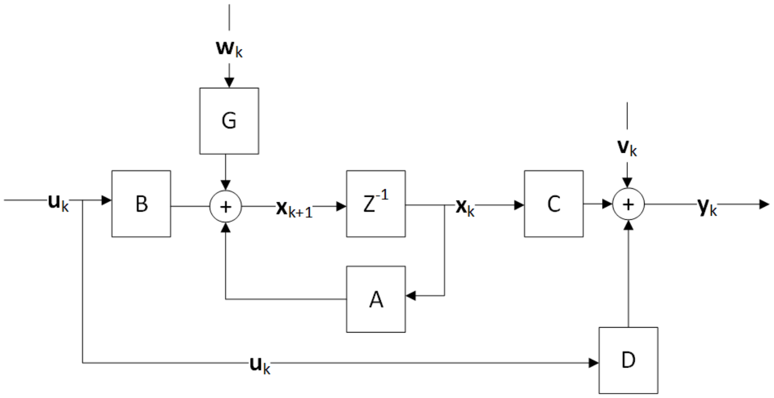

Figure 1.1: Discrete time state space model with process and measurement noise.

The system's noise influences the achievable estimate quality through the Cramér-Rao inequality [1] which defines the lower bound on the expected value of the error of an unbiased estimate as,

$$P \equiv E\{(\hat{x} - x)(\hat{x} - x)^T\} \geq F^{-1}$$

where P is the estimate error covariance matrix, x is the state, $\hat{x}$ is the estimate of the state, and F is the Fisher information matrix. The Fisher information matrix is a function of the probability density function, $p(y|x)$, where the observation, y, is stochastic due to measurement noise. When the variance of the noise is large, the Fisher information matrix is small and the achievable estimate will have larger expected errors.

In practical applications, it is rare to have accurate knowledge of the process and measurement noise covariances of a system model [2, 3]. Process noise is particularly hard to characterize. When the noise covariances are unavailable, a Kalman filter loses its optimal guarantee. In this situation, a sub-optimal Kalman filter may be designed by empirically "tuning" noise covariance matrices based on the expected or desired estimate behavior. The Autocovariance Least Squares (ALS) technique [4, 5, 6, 7] identifies the noise covariances from test data; which in turn can be used to design optimal estimators. Anchoring the stochastic system to test data enables the use of optimal design techniques like the Kalman filter.

The equations of motion of an aerospace vehicle are generally nonlinear. However, in certain circumstances the nonlinear dynamics can be approximated with adequate accuracy using small perturbation theory to linearize the equations of motion about a trim condition [8, 9]. This approach allows for linear control and estimation techniques which typically reduce the complexity of the system. A less complex vehicle systems design reduces the software development and testing burden. In other aerospace applications, such as high angle of attack flight, rapid variations in vehicle weight, or aggressive maneuvering, linear approximations are not reasonable. These scenarios motivate nonlinear control and estimation approaches such as an Extended Kalman filter or Unscented Kalman filter.

The application of the ALS technique to classes of systems with high dimension and nonlinear dynamics, particularly aerospace vehicles, presents challenges that are explored in this dissertation. When both rigid and aeroelastic modes are critical to the dynamics, the aircraft system model will be large. Furthermore, the eigenvalues of that model can span a wide frequency range. Aerospace vehicles typically operate over a wide range of conditions; aircraft span a range of airspeed, mach, and altitudes, while spacecraft operate within and outside of Earth's atmosphere. The availability of measurement data, considering location of sensors on the vehicle, quantity of sensors, and affordability of collecting large sets of data throughout the operational envelope presents an additional challenge. These challenges will be addressed with extensions to the ALS convex optimization problem.

1.1 Literature Review

The development of noise covariance identification techniques throughout the last century follows that of state estimation to enable modern state feedback control techniques. Several estimation approaches benefit from better knowledge of the stochastic model. The Gauss-Markov theorem proves that the linear least squares solution weighted by the inverse of observation error covariance produces the minimum variance estimate [1]. Maximum likelihood estimation identifies unknowns by maximizing the probability of the observations. Bayesian estimation extends maximum likelihood estimation through usage of *a priori* estimates. The Kalman filter builds on minimum variance estimation by incorporating a stochastic dynamic process model. The Kalman filter is chosen for state estimation in this dissertation because it is proven to provide an optimal estimate, is capable of scaling for high order systems, and with the Extended Kalman filter, can be extended for nonlinear dynamics. This section discusses relevant work on optimal estimation and on noise covariance identification techniques, including the ALS technique.

1.1.1 Optimal Estimation and the Kalman Filter

The advent of modern control theory and state feedback control techniques necessitated full knowledge of system states for control law design. For some systems the states can be directly measured, or determined from an algebraic combination of measurements. More often, some or all of the states are not directly measurable due to dynamic complexities, harsh operating conditions, or cost. Research in optimal estimation emerged in parallel with modern control theory to develop state estimation algorithms. The equations for the linear Kalman filter and the fixed-interval Kalman smoother are presented in this section.

Estimation for nonlinear state dynamics has also been developed. Two common nonlinear estimation algorithms are the Extended Kalman filter (EKF) and the Unscented Kalman filter (UKF). The EKF is based on the assumption that the error dynamics can be represented with sufficient accuracy by a first order Taylor series expansion [1]. While the EKF does not guarantee an optimal estimate, it performs well with a good initial state estimate. The UKF is more computationally demanding, but performs better for highly nonlinear systems [10, 1].

Linear Kalman Filter

The Kalman filter, described by Kalman [11] and Kalman and Bucy [12] is an optimal linear quadratic estimation algorithm for zero mean Gaussian noise processes. Over the decades since its introduction, the Kalman filter and its variations have remained the popular state estimation method due to performance and computational efficiency [13]. The Kalman filter has been applied broadly since the latter half of the 20th century, including early application on NASA's Apollo program [14]. The Kalman filter employs a prediction-correction algorithm where a prediction is made based on the dynamics and corrected with the Kalman gain as measurements are observed. The Kalman filter is proven to calculate the maximum likelihood estimate of the state [1, 15, 16, 17].

The following derivation of the discrete time linear Kalman filter will be used in this dissertation. Beginning with a system model structure as shown in Eq. (1.1) and the following assumption,

Assumption 1 *The noise terms, w_k and v_k, are uncorrelated zero-mean Gaussian white-noise processes with error covariance matrices, Q_k and R_k, defined such that*

$$\begin{aligned} E\left\{w_k w_k^T\right\} &= \begin{cases} 0, & k \neq j \\ Q_k, & k = j \end{cases} \\ E\left\{v_k v_k^T\right\} &= \begin{cases} 0, & k \neq j \\ R_k, & k = j. \end{cases} \end{aligned}$$

Estimates of the state will be obtained using a standard *a priori* recursive Kalman filter [1] where the state estimate, $\hat{x}_k$, is given by

$$\hat{x}_{k+1} = A\hat{x}_k + Bu_k + AK_k\left(y_k - C\hat{x}_k\right) \tag{1.2}$$

with Kalman gain, K_k, given by

$$K_k = P_k C^T \left(C P_k C^T + R_k\right)^{-1}. \tag{1.3}$$

Defining the state estimate error as $\varepsilon_k \equiv x_k - \hat{x}_k$ with covariance $P_k = E\{\varepsilon_k \varepsilon_k^T\}$, the covariance evolves according to

$$P_{k+1} = AP_kA^T - AK_kCP_kA^T + GQ_kG^T. \tag{1.4}$$

Linear Kalman Smoother

When real-time estimates are not required during operation, post-processing with a linear Kalman smoother generates lower variance estimates [18, 1, 19]. Smoothing combines two Kalman filters, a forward-time filter and backward-time filter, over the interval of data.

The following derivation of the discrete time steady state linear Kalman smoother will be used in this paper. A steady state assumption is made such that the system matrices and covariances do not change with time. Beginning with a systems model from Eq. (1.1), the forward propagation equations are that of the the linear Kalman filter, Eqs. (1.2) - (1.4). The subscript 'f' is appended to these equations to denote forward propagation,

$$\begin{aligned} K_f &= P_f C^T \left(C P_f C^T + R_v \right)^{-1} \\ P_f &= A P_f A^T - A K_f C P_f A^T + G Q_w G^T \\ \hat{x}_{k+1} &= A \hat{x}_{f,k} + B u_k + A K_f \left(y_k - C \hat{x}_{f,k} \right). \end{aligned} \tag{1.5}$$

Similar to the forward filter, the covariance of the backward filter is found by solving a Riccati equation. Where the steady-state Hamiltonian is,

$$\mathscr{H} = \begin{bmatrix} A^{-1} & A^{-1} G Q_w G^T \\ C^T R_v^{-1} C A^{-1} & A^T + C^T R^{-1} C A^{-1} G Q_w G^T \end{bmatrix} \tag{1.6}$$

whose eigenvector decomposition takes the form,

$$\mathscr{H} = \begin{bmatrix} W_{11} & W_{12} \\ W_{21} & W_{22} \end{bmatrix} \begin{bmatrix} \Lambda & 0 \\ 0 & \Lambda^{-1} \end{bmatrix} \begin{bmatrix} W_{11} & W_{12} \\ W_{21} & W_{22} \end{bmatrix}^{-1} \tag{1.7}$$

where Λ is a diagonal matrix of the eigenvalues outside of the unit circle and the W terms are block elements of the eigenvector matrix. Then, the backward propagation equations are,

$$\begin{aligned} K_b &= \mathscr{P}_b^+ G \left[G^T \mathscr{P}_b^+ G + Q_w^{-1} \right]^{-1} \\ \mathscr{P}_b^+ &= W_{21} W_{11}^{-1} \\ \mathscr{P}_b^- &= \mathscr{P}_b^+ - C^T R^{-1} C \\ \hat{\chi}_{b,k}^- &= A^T [I - K_b G^T][\hat{\chi}_{b,k+1}^+ - \mathscr{P}_b^+ B u_k] \end{aligned} \tag{1.8}$$

The smoother is defined as,

$$\begin{aligned} K &= P_f^+ \mathscr{P}_b^- [I + P_f^+ \mathscr{P}_b^-]^{-1} \\ P &= [I - K] P_f^+ \\ \hat{x}_k &= [I - K]\, \hat{x}_{f,k}^+ + P \hat{\chi}_{b,k}^- . \end{aligned} \tag{1.9}$$

Extended Kalman Filter

Many real world systems have nonlinear dynamics. The Extended Kalman filter is a popular and well demonstrated approach for the nonlinear estimation problem. The Extended Kalman filter relies on an assumption that the error dynamics can be approximated sufficiently well by a first order Taylor series expansion [20, 1]. This assumption has been demonstrated to be true for many systems when the true state is sufficiently close to the state estimate [15]. Beginning with a nonlinear model structure represented by,

$$\begin{aligned} \dot{x}(t) &= f(x(t), u(t), t) + g(t) w(t) \\ y(t) &= h(x(t), t) + v(t) \end{aligned} \tag{1.10}$$

where $w(t) \sim N(0, Q(t))$ and $v(t) \sim N(0, R(t))$. The Kalman gain, K_k is given by,

$$\begin{aligned} K_k =& P_k^- H_k^T(\hat{x}_k^-) [H_k(\hat{x}_k^-) P_k^- H_k^T(\hat{x}_k^-) + R_k]^{-1} \\ H_k(\hat{x}_k^-) \equiv& \left. \frac{\partial h}{\partial x} \right|_{\hat{x}_k^-} . \end{aligned} \tag{1.11}$$

The update equations are

$$\begin{aligned} \hat{x}_k^+ =& \hat{x}_k^- + K_k [y_k - h(\hat{x}_k^-)] \\ P_k^+ =& [I - K_k H_k(\hat{x}_k^-)] P_k^- . \end{aligned} \tag{1.12}$$

The estimate propagates according to

$$\begin{aligned} \dot{\hat{x}} =& f(\hat{x}(t), u(t), t) \\ \dot{P}(t) =& F(t) P(t) + P(t) F^T(t) + g(t) Q(t) g^T(t) \\ F(t) \equiv& \left. \frac{\partial f}{\partial x} \right|_{\hat{x}(t), u(t)} . \end{aligned} \tag{1.13}$$

1.1.2 Noise Covariance Identification

In physical systems represented by linear models such as Eq. (1.1), the process disturbance model, G, process noise, w_k, and measurement noise, v_k, are commonly unknown. For some applications, the measurement noise covariance matrix, R_v, may be identifiable through lab based sensor experiments, but the lab environment may not be representative of the measurement noise covariance in an operational scenario. In practice, to set the Kalman gain, K_k, of an estimator the designer may heuristically tune the process noise covariance matrix, Q_w, and the measurement noise covariance matrix, R_v, to achieve desired state estimate characteristics. As shown by Heffes [21] and Nishimura [22], erroneous values for the noise covariance matrices lead to sub-optimal state estimates. Numerous methods for noise covariance identification have been developed over the last five to six decades as necessitated by optimal estimation and control techniques [3]. Consistently, across the range of approaches, the identification of the elements of Q_w is more challenging than that of R_v [23]. Noise covariance identification methods can be classified into four categories, correlation techniques, maximum likelihood estimation techniques, Bayesian techniques, and covariance matching methods [24]. Recent works [25, 26, 27], consider a Policy Optimization algorithm to directly learn the steady-state optimal Kalman gain for systems with unknown noise covariances.

Correlation Techniques

Correlation techniques for identification of nose covariance matrices begin with an asymptotically stable sub-optimal filter and evaluate the error of the resultant measurement prediction sequence. The measurement prediction sequence is also referred to in the literature as the innovations. This category of noise identification techniques was introduced by Mehra in [23] and [2]. Mehra's technique is a multi-step process which provides unbiased estimates of the noise covariance matrices as the length of the innovation sequence approaches infinity. Typically correlation techniques are capable of identifying all elements of the measurement covariance matrix, R_v, but may be limited in identifying the elements of the process noise matrix, Q_w, by the number of measurements.

Berry and Sauer [28] built on Mehra's approach by extending it to nonlinear systems. Bélanger [29] presents a weighted correlation method which extends Mehra's approach for linear time varying models with correlated measurement and process noises using basis matrices with unknown weights. Neethling and Young [30] responded to Bélanger with a Monte-Carlo least squares improvement. The ALS method [4], a single step correlation technique, will be discussed in detail in Section 1.1.3.

Maximum Likelihood Estimation Techniques

Maximum likelihood estimation [31], solves for the noise statistics by maximizing a probability density function of the measurement residuals of a filter. Mehra [2] describes an adaptive filter which identifies the covariance matrices by maximizing a likelihood function. Three versions of likelihood functions are considered:

1. Joint Maximum Likelihood Estimate: states and unknown covariance matrices are estimated simultaneously by maximizing

   $$p(x_k, Q_w, R_v | y_0 ... y_k), \tag{1.14}$$

   with respect to x_k, Q_w, and R_v.

2. Marginal Maximum Likelihood Estimate: unknown covariance matrices are estimated simultaneously by maximizing

   $$p(Q_w, R_v | y_0 ... y_k), \tag{1.15}$$

   with respect to Q_w, and R_v.

3. Conditional Mode Estimate: states are estimated simultaneously by maximizing

   $$p(x_k | y_o ... y_k), \tag{1.16}$$

   with respect to x_k.

Of the three functions, the Marginal Maximum Likelihood Estimate is the simplest. Focusing on that approach and using Bayes rule,

$$p(Q_w, R_v|y_0...y_k) = \frac{p(y_0...y_k|Q_w, R_v)p(Q_w, R_v)}{p(y_0...y_k)} \tag{1.17}$$

then the marginal likelihood estimate is the maximum of,

$$L(Q_w, R_v) = \log(p(Q_w, R_v|y_0...y_k)) \tag{1.18}$$

where

$$\left\{\frac{\partial}{\partial x}\log[L(Q_w, R_v)]\right\}\bigg|_{\hat{x}} = 0 \tag{1.19}$$

and

$$\frac{\partial^2}{\partial x \partial x^T}\log[L(Q_w, R_v)] < 0. \tag{1.20}$$

Each of the maximum likelihood estimate approaches are computationally expensive, requiring nonlinear programming [32, 3], and are not guaranteed to converge. A common simplification is to limit the set of unknowns. Dempster [33] proposes the Expectation Maximization (EM) algorithm which is used by Shumway and Stoffer [34]. The EM algorithm begins with the smoothed estimation of the state given an estimate of the initial state and noise covariance matrices. Next, the unknown parameters are estimated with maximum likelihood estimation using the state estimates obtained from the expectation step.

Bayesian Techniques

Initial study of covariance matrix identification used a Bayesian adaptive filter approach. Magill [35] and Hilborn [36] describe a recursive algorithm to determine the a-posteriori probability distribution and concurrently find the states and unknowns in an augmented state vector from a finite set of possibilities. When the vector of unknowns is limited to the covariance matrices, the probability density of x_k, Q_w, and R_v is written as

$$p(x_k, Q_w, R_v|y_0...y_k) = p(x_k|Q_w, R_v, y_0...y_k)p(Q_w, R_v|y_0...y_k). \tag{1.21}$$

The first term, $p(x_k|Q_w, R_v, y_0...y_k)$, is the probability distribution of the state, x_k for a given pair of Q_w and R_v. The second term, $p(Q_w, R_v|y_0...y_k)$, is evaluated as,

$$p(Q_w, R_v|y_0...y_k) = \frac{p(y_k|Q_w, R_v, y_0...y_{k-1})p(Q_w, R_v|y_0...y_{k-1})}{\int_\Gamma p(y_k|Q_w, R_v, y_0...y_{k-1})p(Q_w, R_v|y_0...y_{k-1})d\Gamma} \tag{1.22}$$

where Γ is the set of unknowns. The estimate of the state, $\hat{x}_k$, is calculated from the probability distribution, $p(x_k|y_o....y_k)$ by integrating over the set of unknowns and evaluating the expected value over x_k,

$$\begin{aligned}\hat{x}_k &= E_{x_k} p(x_k|y_0....y_k) \\ &= E_{x_k} \int_\Gamma p(x_k|Q_w, R_v, y_0....y_k)p(Q_w, r_v|y_0....y_k)d\Gamma \\ &= \int_\Gamma \hat{x}_k(Q_w, R_v)p(Q_w, R_v|y_0...y_k)d\Gamma.\end{aligned} \tag{1.23}$$

The estimated state is the sum of estimates for the entire set of Q_w and R_v weighted by their probability density function. In practice this algorithm is computationally prohibitive for a large set of unknowns, Γ. In the case that Q_w and R_v come from a known finite set the solution is feasible. Matisko and Havlena [37] combine Bayesian principles and Monte-Carlo numerical methods to estimate noise covariances for a collection of simulated systems.

Covariance Matching Techniques

Covariance matching techniques estimate the state and identify the noise covariance matrices by aligning the covariances of the state estimate residuals with their theoretical covariance,

$$E[\mathscr{Y}_k \mathscr{Y}_k] = E[(y_k - C\hat{x}_{k|k+1})(y_k - C\hat{x}_{k|k+1})]. \tag{1.24}$$

Myers and Tapley [38] present the adaptive limited memory filter which is shown for linear time varying models with time varying covariance matrices. In general, covariance matching techniques progress through four steps: estimate R_v from the innovations, estimate the filter state and covariance, P, estimate the prediction state, and finally estimate Q_w through approximations of process noise, w_k. This technique in Myers and Tapley [38] is not guaranteed to converge to the true covariance matrix values.

1.1.3 Autocovariance Least Squares

Odelson [4, 5, 39] develops the ALS technique, a direct correlation method. Similar to indirect correlation methods, the ALS technique results in covariance estimates with low variance. Its advantage over indirect correlation methods is that ALS a single step procedure. The least squares problem takes the structure of a convex semidefinite programming problem. The least squares problem can be simplified to a quadratic programming problem when the covariance matrices are diagonal. Rajamani and Rawlings [6, 7] derive the one-column version of the ALS technique and introduce the optimal minimum variance weighting for the ALS problem. This weighting depends on the unknown covariance matrices, Q_w, R_v, and the G matrix. An iterative solution is proposed beginning with an initial guess of Q_w, R_v, and G for the least squares weighting. The identified matrices from the ALS solutions with weighting from the initial guess are then used in a second solution, which is repeated until convergence. This approach is not guaranteed to converge and may be intractable for large systems. Zagrobelny [40] proposes two improvements to simplify the ALS approach for practical applications. First, an observability matrix singular value decomposition based approach to remove poorly observable states. Second, a feasible-generalized least squares method which approximates the optimal minimum variance weighting of the ALS problem from the data set.

The time invariant ALS techniques developed by Odelson, Rajamani, and Rawlings [39, 7] are extended to time varying and nonlinear systems by Rajamani [6], Lima and Rawlings [41], Ge and Kerrigan [19], and Abdel-Hafez [42]. They each demonstrate that with a reasonable initial selection of the state and covariance matrices a sliding window ALS problem can be structured. Similar to the Extended Kalman filter, the nonlinear dynamics are approximated by a time varying linearization about the state estimate.

1.2 Contributions of this dissertation

In this dissertation, four extensions to the ALS technique are derived and demonstrated. Each of the extensions addresses one or more challenges encountered with the ALS solution for an aerospace system including, ill-conditioning of the ALS problem, unknown atmospheric disturbances, uncertainty in the dynamic model, and limited data availability. The benefits of noise identification are realized in subset of the applications for which optimal estimation is beneficial, particularly where accurate noise covariance statistics notably impact the quality of an estimate. In this section we will highlight benefits for sensor selection and management, atmospheric disturbance characterization, and model uncertainty.

Sensor Selection, Fault Detection, and Management

Modern aerospace vehicles rely on integrated control systems which require accurate information about the vehicle's states. Hardware redundancy in the sensor suite is common for critical sensors, but is subject to weight, spatial, and financial limitations [43]. Multiple, identical sensor components enables sensor health monitoring by limit checking and voting [43]. Wilsky [44] describes a standard voting scheme with at least 3 redundant inputs, which eliminates a sensor if it's output does not align with the remaining two votes in the set. A cluster of sensors may be combined to create one value used by the control law through averaging, mid-value select, or an observer.

Similar sensors, or sensors that are co-located are subject to common cause failures [45]. When independent estimate can be generated from a dissimilar sensors, installed on a different part of the vehicle, it can be used to assess the health of the primary measurement source. Dissimilar sensors may be combined to create analytical redundancy, with a detection filter, single Kalman filter, or with a bank of Kalman filters [46]. Accurate state estimation is necessary to enable comparison between estimated and measured values for selection, detection and monitoring.

In Section 4.1 the ALS identified process and measurement noise of a system is used to generate independent sensor estimates for a commercial aircraft simulated data set. In Section 4.3 the ALS problem is solved with an additional constraint extension to identify the states across a set of operating conditions. This work will be published in [47].

Atmospheric Disturbance Characterization

Turbulent airflow in the atmosphere drives energy into the aircraft; exciting both rigid body and flexible dynamic modes, increasing loads, and lowering ride quality, [48, 49]. The pursuit to understand and characterize atmospheric turbulence and gusts reaches back over a century to Wilson's article "Theory of an Aeroplane Encountering Gusts"[50] in Part II of the initial NACA report. Wilson's report establishes the equations of motion that govern an aircraft in discrete gusts. Research of gusts and turbulence can be divided into two subsets:

1. Establishing the range of turbulence encountered as a function of flight regime to establish design and certification requirements, and
2. Gust measurements for use by real time active control algorithms.

In Etkin's Wright Brothers Lecture [51] he describes the advancements in the research up to the 1980s. He includes extensive data collection in flight test, theoretical developments and modeling. Notably the Dryden and von Kármán continuous gust velocity power spectral density models [52, 53] which are used widely in industry and academia for commercial and military vehicles.

The Dryden turbulence model, introduced in 1952 by [54], specifies turbulence as a rational power spectral density,

$$\Phi(\Omega)_{dry} = \sigma_v^2 \frac{L_v}{\pi} \frac{1 + 3L_v^2\Omega^2}{[1 + (L_v\Omega)^2]^2}. \tag{1.25}$$

The von Kármán turbulence model, originally published in 1957 [55], specifies turbulence as an irrational power spectral density,

$$\Phi(\Omega)_{vK} = \sigma_v^2 \frac{L_v}{\pi} \frac{1 + \frac{8}{3}(1.339L_v\Omega)^2}{[1 + (1.339L_v\Omega^2]^{11/6}}. \tag{1.26}$$

The Dryden and von Kármán models are shown in Fig. 1.2, where σ_v is the root mean square gust velocity, Ω is the spatial frequency, and L_v is the scale of turbulence in the lateral direction. The von Kármán model gives a better fit to measured data, while the Dryden model allows for the derivation of an exact shaping filter for white noise to the model's spectral shape [53]. For flight at altitudes above 2000 ft, MIL-F-8785C recommends $L_v = 1750\ ft$ and provides root mean square gust amplitude probabilities as a function of altitude [56].

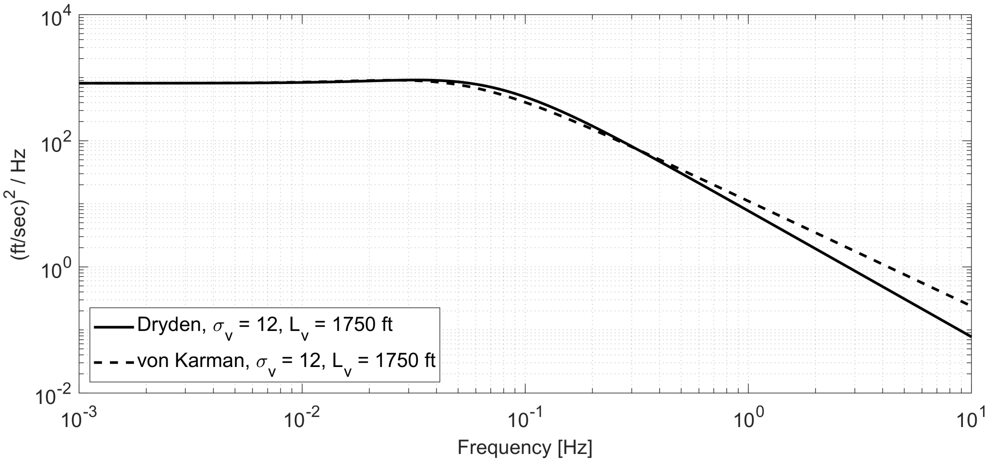

Figure 1.2: Comparison of Dryden and von Kármán gust velocity power spectral density models.

Extensive effort has been directed towards the design of load alleviation, modal suppression, and ride quality control techniques [57] as well as towards the investigation of which flexible dynamics are most objectionable to the human [58, 59]. A load alleviation control algorithm deflects wing surfaces to modify the lift distribution with the arrival of a discrete gust. Successful load alleviation reduces the critical loads and results in weight savings to the vehicle [60, 61, 62]. A modal suppression control algorithm commands control surfaces to increase the damping of the aeroelastic modes of the vehicle, including the reduction of biodynamic coupling [63, 64, 65, 66, 67, 68]. Ride quality control algorithms aim to improve the pilot and passenger comfort, including reducing airsickness [69, 70]. These three control types are affected by, and are required to perform, in the presence of atmospheric disturbances. Knowledge of the atmospheric disturbance enables quantitative demonstration of the in-flight control law performance as well as comparison of in-flight control law performance to analytical predictions.

Measurement of the atmosphere by a vehicle moving rapidly through it is challenging. Historically, the most frequent records of turbulence are Pilot Reports or PIREPs [71], which contain assessment of atmospheric conditions, reported to air traffic control as the aircraft encounters them. PIREPs, also called Air Reports (AIREPs), are qualitative and do not contain a quantitative measure of the atmosphere. To improve turbulence modeling capabilities, the Federal Aviation Administration funded the development of an *in situ* turbulence measurement and reporting system for commercial aircraft [72]. This approach uses existing aircraft sensors and available communication channels to record turbulence intensity, measured as the eddy dissipation rate (EDR). The EDR is the International Civil Aviation Organization standard for measurement of turbulence intensity. A sizable data set has been collected, enabling the creation of more reliable turbulence maps [73]. The EDR data is statistical, with the aim of meteorological model development. It does not capture individual atmospheric disturbance time histories as desired for this dissertation. Experimentally, Humbolt et al. [52] measured turbulence with flow vanes and differential pressure sensors on a boom that extended ahead of the vehicle. Similarly, Hunter et al. [74] sensed gusts with an angle of attack vane on a boom in front of a test aircraft. Numerous studies, [75, 76, 77, 78, 79] have demonstrated the use of a Light Detection And Ranging sensor (LIDAR) both to provide a sensor input to the control algorithm of upcoming atmospheric disturbance and to give the crew advance notice of turbulent conditions. However, these experimental methods depend on the addition of a dedicated novel sensor set that is not standard for a flight test vehicle.

In Section 4.2 ALS is used to identify the process and measurement noise for the Kirsten Wind Tunnel gust load alleviation test-bed. Knowledge of the noise properties is combined with a colored noise Kalman filter approach to estimate the gust imparted on the test-bed model by the gust generation system. This work is published in [80]. In Section 4.4 ALS is used to identify the process and measurement noise covariance for a high order commercial aircraft model from flight test data. These covariances are used with a colored noise Kalman filter to estimate atmospheric disturbances encountered in turbulent flight. The underlying models and flight test data used in this analysis are proprietary. The results shared in this dissertation have been normalized and non-dimensionalized and will be published in [81]. Additionally, this work will be fully documented in an internal Boeing publication.

Model Uncertainty

The cost and complexity of modern aerospace systems necessitates a model based design approach. A significant amount of engineering effort is centered around the analysis, lab test, wind tunnel test, ground test, and flight test to develop accurate models. Optimal estimation relies on the accuracy of dynamic models. Despite significant effort, all models have some level of uncertainty. For example, linear simplifications are common for vehicles with nonlinear dynamics.

In this research an approach is proposed using a Kullback–Leibler (K-L) divergence based metric to assess the optimality of an estimate. When ALS identified process and measurement noise covariances are used in the estimator design, this metric indicates the level of model uncertainty. It will be shown that the optimality of an estimate can be used as a tool to quantify uncertainty in the model used to generate it. In some cases the quantified uncertainty points to adjusting model parameters and in others it indicates a need to adjust the modeling approach. Model uncertainty is further investigated by posing a nonlinear parameter estimation problem and solving the time varying ALS problem to identify the noise covariances. The Extend Kalman filter designed with the identified noise covariances then estimates the unknown or uncertain parameter.

The K-L divergence metric is used to compare state estimator performance in each Section of Chapter 4. Specifically, the K-L divergence metric is utilized to evaluate model uncertainty in the damping of the Kirsten Wind Tunnel Large Wing test-bed in Section 4.2. This work is published in [82, 83]. The results of this K-L divergence study are compared with results from a time variant ALS tuned Extended Kalman filter.

1.3 Organization

This dissertation is organized as follows. In Chapter 2 the ALS technique is derived for both the time invariant and time varying cases. In Chapter 3 four extensions of the ALS technique are derived to accommodate the challenges of aerospace problems. Illustrative examples with simple system dynamics are presented for each extension. In Section 3.1 the conditioning of the ALS problem is considered with approaches for evaluating the conditioning and methods for improving the ALS solutions. The colored noise Kalman filter for disturbance estimation is derived in Section 3.2. Section 3.3 proposes the use of a K-L divergence metric to quantify the optimality of a set of estimators and evaluate potential uncertainty in a model. Additional constraints on the least squares problem are investigated in Section 3.4 with the aim of solving the ALS problem for a set of conditions. Finally, in Chapter 4 the methods discussed in Chapter 3 are a applied to several aerospace vehicles, including two gust load alleviation test-beds and two commercial aircraft.

Chapter 2

AUTOCOVARIANCE LEAST SQUARES

In this section, two versions of the ALS technique are derived. First, the linear time invariant ALS problem which is applied throughout this dissertation when system dynamics can be approximated linearly. Second, the linear time variant ALS problem (LTV-ALS) which is applied to systems with time varying or nonlinear dynamics.

2.1 ALS for systems with time invariant dynamics

The linear time invariant ALS derivation begins with the following assumption.

Assumption 2 *The pair* (A, C) *from the system model, Eq.* (1.1) *is observable.*

As a consequence of observability, there exists a constant, stabilizing (sub-optimal) Kalman gain, L. The dynamics of the state estimate error, $\varepsilon_k = x_k - \hat{x}_k$, can then be expressed as

$$\varepsilon_{k+1} = \underbrace{(A - ALC)}_{\bar{A}} \varepsilon_k + \underbrace{\begin{bmatrix} G & -AL \end{bmatrix}}_{\bar{G}} \underbrace{\begin{bmatrix} w_k \\ v_k \end{bmatrix}}_{\bar{w}} . \tag{2.1}$$

Assumption 1 from the derivation of the Kalman filter in Section 1.1.1 is repeated here for this derivation. Defining the measurement innovations as

$$\mathscr{Y}_k = y_k - C\hat{x}_k, \tag{2.2}$$

one can then express the system dynamics in terms of the estimator error and the innovations as

$$\begin{aligned} \varepsilon_{k+1} &= \bar{A}\varepsilon_k + \bar{G}\bar{w}_k \\ \mathscr{Y}_k &= C\varepsilon_k + v_k. \end{aligned} \tag{2.3}$$

Furthermore, with a stabilizing Kalman gain, L, the initial conditions of Eq. (2.1) can be neglected after sufficient time has passed: $E\{\varepsilon_k\} \rightarrow 0$, $cov(\varepsilon_k) \rightarrow P^-$. To determine the estimate of the noise covariance terms, we will utilize the autocovariance of the innovations, specifically the expected value of the innovations at a given time relative to the innovations time-shifted by j time steps (also termed "lags"), $\mathscr{C}_j$:

$$\mathscr{C}_j = E\big[\mathscr{Y}_k \mathscr{Y}_{k+j}^T\big]. \tag{2.4}$$

We can then construct the elements of the autocovariance column matrix, $\hat{b}$, which are autocovariances for a range of lags from $j = 0$ to N:

$$\hat{b} = \begin{bmatrix} \mathscr{C}_0 \\ \vdots \\ \mathscr{C}_{N-1}^T \end{bmatrix}. \tag{2.5}$$

Using Eq. (2.1), the autocovariance can be expressed as

$$\begin{aligned} E\big[\mathscr{Y}_k \mathscr{Y}_k^T\big] &= C P^- C^T + R_v \\ E\big[\mathscr{Y}_{k+j} \mathscr{Y}_k^T\big] &= C \bar{A}^j P^- C^T - C \bar{A}^{j-1} A L R_v \end{aligned} \tag{2.6}$$

where P^-, the steady-state covariance matrix, is the solution of the Lyapunov equation, [1]

$$P^- = \bar{A} P^- \bar{A}^T + \bar{G} \begin{bmatrix} Q_w & 0 \\ 0 & R_v \end{bmatrix} \bar{G}^T. \tag{2.7}$$

Now define the matrix $\mathscr{A}$ as

$$\begin{aligned} \mathscr{A} &= \Big[\mathscr{A}_1 \, \mathscr{A}_2\Big] \\ \mathscr{A}_1 &= \Big[C \otimes \mathscr{O}(I_{n^2} - \bar{A} \otimes \bar{A})^{-1}\Big] \mathscr{D}_n \\ \mathscr{A}_2 &= \Big[C \otimes \mathscr{O}(I_{n^2} - \bar{A} \otimes \bar{A})^{-1}(AL \otimes AL) + (I_p \otimes \Gamma)\Big] \mathscr{D}_p \end{aligned} \tag{2.8}$$

where $\otimes$ is the Kronecker tensor product. The terms $\mathscr{O}$ and Γ are defined as

$$\mathscr{O} = \begin{bmatrix} C \\ C\bar{A} \\ \vdots \\ C\bar{A}^{N-1} \end{bmatrix}, \quad \Gamma = \begin{bmatrix} I_p \\ -CAL \\ -C\bar{A}AL \\ \vdots \\ -C\bar{A}^{N-2}AL \end{bmatrix}. \tag{2.9}$$

The matrices $\mathscr{D}_p$ and $\mathscr{D}_n$ are duplication matrices composed of zeros and ones that ensure symmetry of the estimated covariance matrices. Duplication matrix $\mathscr{D}_j \in \mathbb{R}^{j^2 \times \frac{j(j+1)}{2}}$ is constructed such that $(R_v)_s = \mathscr{D}_j (R_v)_{ss}$ where the subscript s is used to represent the column-wise stacking and the subscript ss is used to represent the column-wise stacking of only the symmetric $\frac{j(j+1)}{2}$ elements of Q_w and R_v.

To determine values for the noise covariance terms, a positive semidefinite constrained least squares problem is constructed as follows:

$$\phi(Q_w, R_v) = \min_{Q_w, R_v} \left\| \mathscr{A} \begin{bmatrix} (Q_w)_{ss} \\ (R_v)_{ss} \end{bmatrix} - \hat{b} \right\|_2^2 \tag{2.10}$$

where $\mathscr{A}$ is defined in Eq. (2.8) and $\hat{b}$ is the stacked first column of the autocovariance matrix, as defined in Eq. (2.5). There are many approaches to solve a least squares convex optimization problem of this type, [84]. The least squares problem can be cast as a quadratic programming problem, when Q_w and R_v are diagonal positive semidefinite matrices. A semidefinite programming solution is used when Q_w and R_v are not diagonal.

Note, in the absence of constraints, the solution of Eq. (2.10) is given by

$$\begin{bmatrix} (Q_1)_{ss} \\ (R_1)_{ss} \\ \vdots \\ (Q_n)_{ss} \\ (R_n)_{ss} \end{bmatrix} = \mathscr{A}^{\dagger} \begin{bmatrix} \hat{b}_1 \\ \vdots \\ \hat{b}_n \end{bmatrix}, \tag{2.11}$$

where $\mathscr{A}^\dagger = (\mathscr{A}^T\mathscr{A})^{-1}\mathscr{A}^T$ is the Moore-Penrose inverse [85]. Error between the finite length observed autocovariance column matrix, Eq. (2.5), and the measurement noise for an infinite length data set, lead to proportional uncertainty in Q_w and R_v through $\mathscr{A}^\dagger$.

2.2 *ALS for systems with time varying dynamics*

The ALS technique is extended for systems with nonlinear or time varying dynamics in [6, 41, 19, 42]. Consistent with the approach of the Extended Kalman filter, time varying linear approximations of the nonlinear dynamics at time step k are defined as,

$$H_k \equiv \frac{\partial h(x_k)}{\partial x_k^T}\bigg|_{\hat{x}_k^-} \qquad F_k \equiv \frac{\partial f(x_k, u_k)}{\partial x_k^T}\bigg|_{\hat{x}_k^-, u_k} \qquad G_k \equiv g(\hat{x}_k^-, u_k). \tag{2.12}$$

Unlike the linear time invariant case, the estimate error covariance, P_k, does not reach steady-state. However, the ALS technique can be extended to time variant system dynamics for the following assumption.

Assumption 3 *The sequence of Extended Kalman filter gains, L_k, as defined in Eq.* (1.11) *with the dynamic approximations as defined in Eq.* (2.12) *result in a sequence, $\bar{F}_k = (F_k - F_k L_k H_k)$ for which the product, $\prod_{k=0}^{j} \bar{F}_i \approx 0$ as j becomes large.*

Next, the innovations are defined as,

$$\begin{aligned}
\mathscr{Y}_k &= H_k(\prod_{i=0}^{k-1} \bar{F}_i)\varepsilon_0 + H_k(\prod_{i=1}^{k-1} \bar{F}_i\bar{G}_0\bar{w}_0 + \prod_{i=2}^{k-1} \bar{F}_i\bar{G}_1\bar{w}_1 + \ldots + \bar{G}_{k-1}\bar{w}_{k-1}]) + v_k \\
\mathscr{Y}_{k+j} &= H_{k+j}(\prod_{i=0}^{k+j-1} \bar{F}_i)\varepsilon_0 + \ldots \\
&\ldots + H_{k+j}(\prod_{i=1}^{k+j-1} \bar{F}_i\bar{G}_0\bar{w}_0 + \prod_{i=2}^{k+j-1} \bar{F}_i\bar{G}_1\bar{w}_1 + \ldots + \bar{G}_{k+j-1}\bar{w}_{k+j-1}]) + v_{k+j}
\end{aligned} \tag{2.13}$$

where, similar to the time invariant case, $\varepsilon_k = x_k - \hat{x}_k$, $\bar{G}_k = [G_k \quad -F_k L_k]$, and $\bar{w}_k = [w_k \quad v_k]^T$. As a result of Assumption 3, the initial estimate error, ε_0, is neglected in $\mathscr{Y}_{k+j}$

when $j > 0$. The the expected values of the autocovariances are,

$$\begin{aligned}
E\big[\mathscr{Y}_k\mathscr{Y}_k^T\big] &= H_k(\prod_{i=1}^{k-1}\bar{F}_i\bar{G}_0 + \ldots + \bar{G}_{k-1})\bar{Q}_w(\bar{G}_0^T\prod_{i=1}^{k-1}\bar{F}_i^T + \ldots + \bar{G}_{k-1}^T)H_k^T + R_v \\
E\big[\mathscr{Y}_{k+j}\mathscr{Y}_k^T\big] &= H_{k+j}(\prod_{i=1}^{k+j-1}\bar{F}_i\bar{G}_0 + \ldots + \prod_{i=k}^{k+j-1}\bar{F}_i\bar{G}_{k-1})\bar{Q}_w(\bar{G}_0^T\prod_{i=1}^{k-1}\bar{F}_i^T + \ldots + \bar{G}_{k-1}^T)H_k^T \ldots \\
&\quad - H_{k+j}(\prod_{i=k+1}^{k+j-1}\bar{F}_i)F_kL_kR_v
\end{aligned} \tag{2.14}$$

where the covariance of $\bar{w}$ is $\bar{Q}_w = \begin{bmatrix} Q_w & 0 \\ 0 & R_v \end{bmatrix}$ and for all $j \leq k$ the $\prod_{i=k}^{j}\bar{F}_i \equiv I$. The autocovariance matrix, $\mathcal{R}_k(N)$ is defined as the expectation of the innovations at different time lags over a defined window, N.

$$\mathcal{R}_k(N) = E\left[\mathscr{Y}_k\mathscr{Y}_k^T \quad \ldots \quad \mathscr{Y}_{k+N-1}\mathscr{Y}_k^T\right]^T \tag{2.15}$$

Then, combining Eq. (2.13) and Eq. (2.14) the autocovariance matrix is expressed as,

$$\mathcal{R}_k(N) = \Gamma\Omega_1 \underset{i=1}{\overset{k}{\oplus}} Q_w\Omega_1^T\Gamma_1^T + \Gamma\Omega_2 \underset{i=1}{\overset{k}{\oplus}} R_v\Omega_2^T\Gamma_1^T + \Psi R_v \tag{2.16}$$

where $\oplus$ is the Kronecker sum defined as $\oplus_{i=1}^{k} Q_w = (I_k \otimes Q_w)$.

The term, Γ, from Eq. (2.16) is

$$\Gamma = \begin{bmatrix} H_k(\prod_{i=1}^{k-1}\bar{F}_i) & \ldots & H_k \\ \vdots & \ddots & \vdots \\ H_{k+N-1}(\prod_{i=1}^{k+N-2}\bar{F}_i & \ldots & H_{k+N-1}(\prod_{i=k}^{k+N-2}\bar{F}_i \end{bmatrix} \tag{2.17}$$

and Γ_1 is the first block row of Γ,

$$\Gamma_1 = \left[(\prod_{i=1}^{k-1}\bar{F}_i)H_k^T \quad \ldots \quad H_k^T\right]. \tag{2.18}$$

The Ω terms are defined as

$$\Omega_1 = \begin{bmatrix} G_0 & \ldots & 0 \\ \vdots & \ddots & \vdots \\ 0 & \ldots & G_{k-1} \end{bmatrix} \qquad \Omega_2 = \begin{bmatrix} -F_0L_0 & \ldots & 0 \\ \vdots & \ddots & \vdots \\ 0 & \ldots & -F_{k-1}L_{k-1} \end{bmatrix}. \tag{2.19}$$

Finally, Ψ is defined as

$$\Psi = \begin{bmatrix} I \\ -H_{k+1}F_kL_k \\ \vdots \\ -H_{k+N-1}(\prod_{i=k+1}^{k+N-2}\bar{F}_i)F_kL_k \end{bmatrix}. \tag{2.20}$$

Here the subscript s will be used to represent column-wise stacking of matrix elements which is necessary to pose the least squares autocovariance problem. The estimate of the autocovariance matrix from observed data is,

$$\hat{b}_k = [\hat{\mathcal{R}}_k(N)]_s = E\begin{bmatrix} \mathscr{Y}_k\mathscr{Y}_k^T & \dots & \mathscr{Y}_{k+N-1}\mathscr{Y}_k^T \end{bmatrix}_s^T. \tag{2.21}$$

The noise covariances are factored out of the autocovariance matrix, $\mathcal{R}_k(N) = \mathscr{A}_k \begin{bmatrix} (Q_w)_s \\ (R_v)_s \end{bmatrix}$. Defining $\mathscr{A}_k = [\mathscr{A}_{k1} \quad \mathscr{A}_{k2}]$ where

$$\begin{aligned} \mathscr{A}_{k1} &= (\Gamma_1\Omega_1 \otimes \Gamma\Omega_1)_s \\ \mathscr{A}_{k2} &= (\Gamma_1\Omega_2 \otimes \Gamma\Omega_2)_s + I_p \otimes \Psi. \end{aligned} \tag{2.22}$$

Now a positive semidefinite constrained least squares problem is constructed with unknowns Q_w and R_v at time step k.

$$\phi_k = \min_{Q_w,R_v} \left\| \mathscr{A}_k \begin{bmatrix} (Q_w)_s \\ (R_v)_s \end{bmatrix} - \hat{b}_k \right\|_2^2 \tag{2.23}$$

Considering a sliding window about each time step, the time varying ALS problem is formulated for data with length N_d as,

$$\phi(Q_w, R_v) = \min_{Q_w,R_v} \left\| \begin{bmatrix} \mathscr{A}_k \\ \vdots \\ \mathscr{A}_{N_d-N+1} \end{bmatrix} \begin{bmatrix} (Q_w)_s \\ (R_v)_s \end{bmatrix} - \begin{bmatrix} \hat{b}_k \\ \vdots \\ \hat{b}_{N_d-N+1} \end{bmatrix} \right\|_2^2. \tag{2.24}$$

Chapter 3

EXTENSIONS OF ALS FOR AEROSPACE SYSTEMS

The application of ALS to aerospace systems for Kalman filter design presents unique challenges due to the nature of system dynamics and the cost and difficulty of collecting large undisturbed data sets. In this chapter, four extensions to the standard ALS problem from Chapter 2 are presented. First, in Section 3.1 adaptations for ill-conditioned ALS problems are discussed. In Section 3.2, ALS is combined with a colored noise Kalman filter approach to estimate the states and an unknown disturbance. Next, in Section 3.3 ALS and a K-L divergence metric are used to evaluate model uncertainty. Finally, in Section 3.4 a noise covariance constrained ALS problem is derived. This ALS problem formulation enables the simultaneous solution of the noise covariances at multiple operating conditions.

Each of these extensions is demonstrated for one or more aerospace systems in Chapter 4. In this section, simple mass-spring-damper systems are used as illustrative examples.

3.1 Ill-Conditioned Autocovariance Least Squares

An ALS problem, Eq. (2.10), can meet Assumption 2 for observability, yet not accurately identify elements of the process noise covariance matrix due to the variance in the solution set. Solution sets with large variance can be misleading when limited data is available. The accuracy of the identified covariances is a function of the condition number,

$$\rho_{\mathscr{A}} = \frac{\sigma_{max}}{\sigma_{min}}, \tag{3.1}$$

where σ_{max} and σ_{min} are the largest and smallest singular values of the $\mathscr{A}$ matrix from Eq. (2.10). Ill-conditioning of the ALS problem is common when the frequency of the eigenvalues of the system span more than an order of magnitude. A frequency span of this size is common in aerospace systems, for example an aircraft phugoid mode and short period mode or the structural modes of a large commercial aircraft.

Recall that the optimal weighting of the ALS problem, as derived by Rajamani and Rawlings [6, 7], requires an iterative approach that is not guaranteed to converge. It is proposed here that, inspection of the system dynamics can indicate a scaling factor which sufficiently improves the accuracy of the solutions. The scaled state estimate dynamics are expressed as

$$\varepsilon_{k+1} = \underbrace{(A - AL\beta C)}_{\bar{A}_\beta} \varepsilon_k + \underbrace{\begin{bmatrix} G & -AL \end{bmatrix}}_{\bar{G}} \underbrace{\begin{bmatrix} w_k \\ \beta v_k \end{bmatrix}}_{\bar{w_\beta}} . \tag{3.2}$$

Defining the scaled measurement innovations as

$$\mathscr{Y}_k = \beta y_k - \beta C \hat{x}_k, \tag{3.3}$$

the system dynamics are then expressed in terms of the estimator error and the innovations as

$$\begin{aligned} \varepsilon_{k+1} &= \bar{A}_\beta \varepsilon_k + \bar{G} \bar{w}_{\beta k} \\ \mathscr{Y}_k &= \beta C \varepsilon_k + \beta v_k. \end{aligned} \tag{3.4}$$

Using Eq. (3.4), the scaled autocovariance can be expressed as

$$\begin{aligned} E\left[\mathscr{Y}_k \mathscr{Y}_k^T\right] &= \beta C P^- (\beta C)^T + R_{v\beta} \\ E\left[\mathscr{Y}_{k+j} \mathscr{Y}_k^T\right] &= \beta C \bar{A}_\beta^j P^- (\beta C)^T - \beta C \bar{A}_\beta^{j-1} A L R_{v\beta} \end{aligned} \tag{3.5}$$

where P^-, the steady-state covariance matrix, is the solution of the Lyapunov equation

$$P^- = \bar{A}_\beta P^- \bar{A}_\beta^T + \bar{G} \begin{bmatrix} Q_w & 0 \\ 0 & R_{v\beta} \end{bmatrix} \bar{G}^T. \tag{3.6}$$

Now define the matrix $\mathscr{A}_\beta$ as

$$\begin{aligned} \mathscr{A}_\beta &= \begin{bmatrix} \mathscr{A}_{\beta 1} \; \mathscr{A}_{\beta 2} \end{bmatrix} \\ \mathscr{A}_{\beta 1} &= \left[\beta C \otimes \mathscr{O}_\beta (I_{n^2} - \bar{A}_\beta \otimes \bar{A}_\beta)^{-1}\right] \mathscr{D}_n \\ \mathscr{A}_{\beta 2} &= \left[\beta C \otimes \mathscr{O}_\beta (I_{n^2} - \bar{A}_\beta \otimes \bar{A}_\beta)^{-1} (AL \otimes AL) + (I_p \otimes \Gamma_\beta)\right] \mathscr{D}_p \end{aligned} \tag{3.7}$$

where $\mathscr{O}_\beta$ and Γ_β are defined as

$$\mathscr{O}_\beta = \begin{bmatrix} \beta C \\ \beta C \bar{A}_\beta \\ \vdots \\ \beta C \bar{A}_\beta^{N-1} \end{bmatrix}, \quad \Gamma_\beta = \begin{bmatrix} I_p \\ -\beta C A L \\ -\beta C \bar{A}_\beta A L \\ \vdots \\ \beta C \bar{A}_\beta^{N-2} A L \end{bmatrix}. \tag{3.8}$$

To determine values for the noise covariance terms, a scaled least squares problem is constructed as,

$$\phi(Q_w, R_{v\beta}) = \min_{Q_w, R_{v\beta}} \left\| \mathscr{A}_\beta \begin{bmatrix} (Q_w)_{ss} \\ (R_{v\beta})_{ss} \end{bmatrix} - \hat{b} \right\|. \tag{3.9}$$

The complexity of scaling the ALS problem by inspection depends on the size and density of the C matrix. When possible, a diagonal scaling matrix is the simplest solution. For some dynamic systems, the condition number of the ALS problem cannot be improved due to the inter-dependence of its outputs on specific states. In these cases, modification to the sensor set is necessary. For some dynamics, G can be chosen such that process noise does not directly rely on the observability of certain states. An example of this simplification is routing w_k into a derivative state as is done in the example below.

Illustrative Example

Consider the dynamics of a two mass-spring-damper system as shown in Fig. 3.1 and described by,

$$\begin{aligned} \begin{bmatrix} \dot{x} \\ \ddot{x} \\ \dot{z} \\ \ddot{z} \end{bmatrix} &= \begin{bmatrix} 0 & 1 & 0 & 0 \\ -\frac{\kappa_1+\kappa_2}{m_1} & \frac{-(b_1+b_2)}{m_1} & \frac{\kappa_2}{m_1} & \frac{b_2}{m_1} \\ 0 & 0 & 0 & 1 \\ \frac{\kappa_2}{m_2} & \frac{b_2}{m_2} & -\frac{\kappa_2}{m_2} & \frac{-b_2}{m_2} \end{bmatrix} \begin{bmatrix} x \\ \dot{x} \\ z \\ \dot{z} \end{bmatrix} + \begin{bmatrix} 0 \\ 0 \\ 0 \\ \frac{1}{m_2} \end{bmatrix} f_1(t) + \begin{bmatrix} 0 & 0 \\ 1 & 0 \\ 0 & 0 \\ 0 & 1 \end{bmatrix} w(t) \\ y &= \begin{bmatrix} 1 & 0 & 0 & 1 \\ 0 & 0 & 1 & 0 \end{bmatrix} \begin{bmatrix} x \\ \dot{x} \\ z \\ \dot{z} \end{bmatrix} + v(t), \end{aligned} \tag{3.10}$$

where $w(t)$ and $v(t)$ are white noise processes. The stiffness, $\kappa_1 = [5,\ 25,\ 50]$, and mass, $m_1 = [1.5,\ 1.25,\ 1]$, are varied to demonstrate the effect of the frequency of the system's eigenvalues on the conditioning of the ALS problem. The other constants are, $b_1 = 1.2$, $\kappa_2 = 0.5$, $m_2 = 2$, and $b_2 = 0.5$. To study the conditioning of the ALS problem for these three systems, 200 datasets were generated by simulating the linear dynamics at 100 Hz with process and measurement noise covariance,

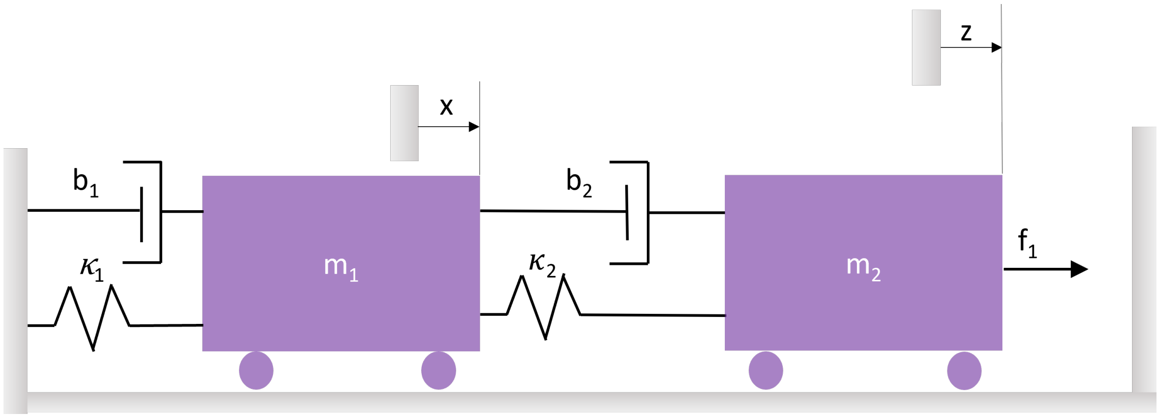

Figure 3.1: Two mass, spring, and damper system.

$$Q_w = \begin{bmatrix} 2 & 0 \\ 0 & 2 \end{bmatrix} \quad R_v = \begin{bmatrix} 0.5 & 0 \\ 0 & 0.5 \end{bmatrix}. \tag{3.11}$$

The ALS problem is then solved for each of the systems for 20 to 300 lags. The conditioning of this ALS problem, $\rho_{\mathscr{A}}$, was expected to degrade with increasing frequency separation of the eigenvalues of Eq. (3.10). This is shown in Fig. 3.2 where the fourth singular value decreases as the value of $\frac{\kappa_1}{m_1}$ increases. Shown on the right plot of Fig. 3.2, a scaling matrix,

$$\beta = \begin{bmatrix} 200 & 0 \\ 0 & 1 \end{bmatrix}^{\frac{1}{2}} \tag{3.12}$$

is multiplied by the output matrix, C, to improve the ALS problem conditioning. The solutions of the four ALS problems $\frac{\kappa_1}{m_1} = [3.33,\ 20,\ 50,\ 50 : \beta_{scaled}]$ are shown in Fig. 3.3 and Fig. 3.4. The accuracy of the mean of the Q_{11} solutions decreases and variance of the Q_{11} solutions increases as $\frac{\kappa_1}{m_1}$ increases. In the third column, $\frac{\kappa_1}{m_1} = 50$, the mean at 300 lags has significant error. The other

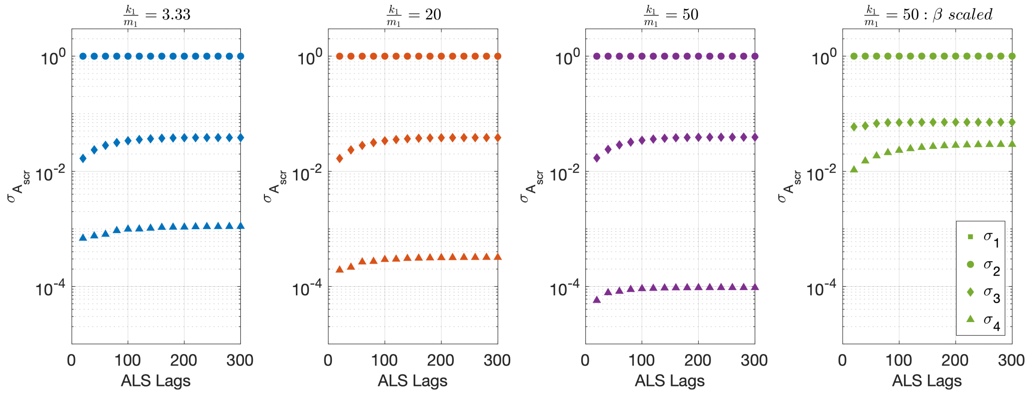

Figure 3.2: Singular values of $\mathscr{A}$ for variation in $\frac{k_1}{m_1}$ and β scaling.

covariance terms, Q_{22}, R_{11}, and R_{22} converge quickly to an accurate value. In the right column, the solutions are shown with β scaling for the system with $\frac{\kappa_1}{m_1} = 50$. Here the accuracy of the Q_{11} solution at 300 lags is significantly improved. As a result of the change in conditioning, the Q_{22} and R_{22} solutions require more lags to converge than in the unscaled problem. Considering the

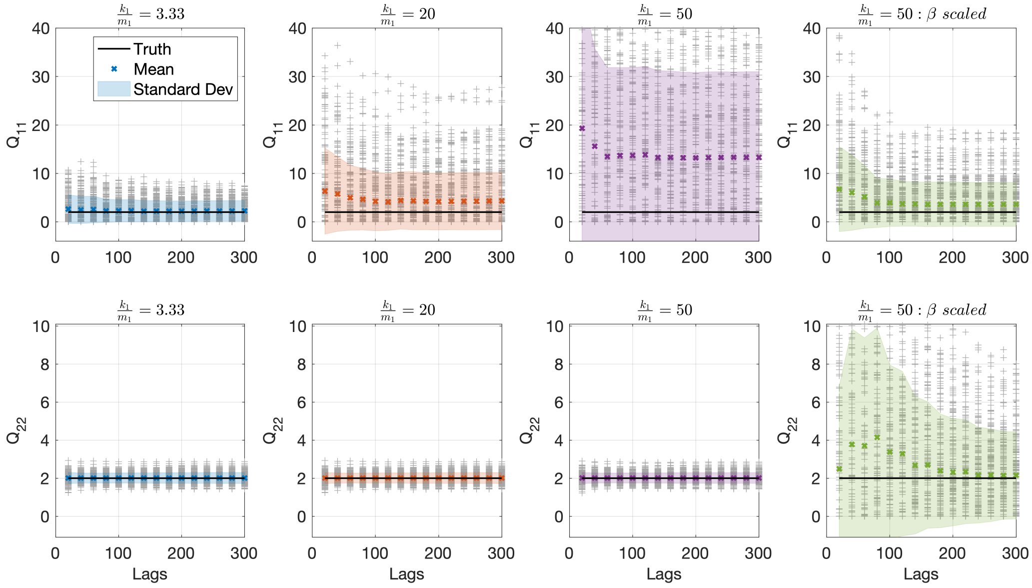

Figure 3.3: Process noise covariance for variation in $\frac{k_1}{m_1}$ and β scaling.

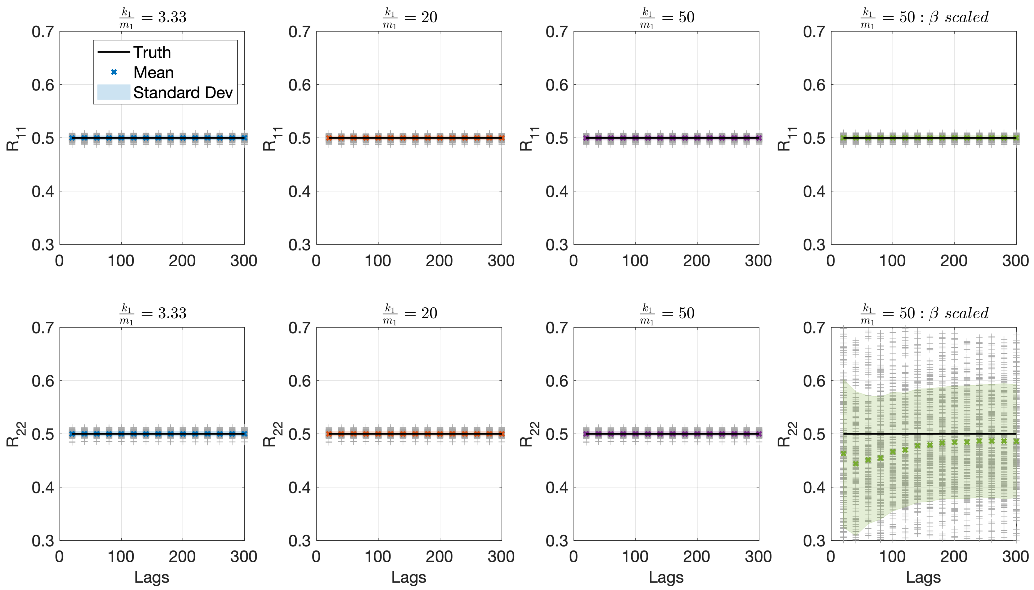

Figure 3.4: Measurement noise covariance for variation in $\frac{k_1}{m_1}$ and β scaling.

unconstrained least squares problem's solution, Eq. (2.11), the rows of $\mathscr{A}^\dagger$, provide insight into the evolution of the Q_w and R_v solutions as a function of lags. In Fig. 3.5, the rows of $\mathscr{A}^\dagger$ that correspond with the Q_{11} and Q_{22} terms are shown for lags, $j = 20 - 300$ for the three system mass and stiffness variations. The coefficients for $j = 300$ are shown with black diamonds and 'o's for $j = 20 - 280$. For the solutions with fewer lags, the corresponding $\mathscr{A}^\dagger$ terms are larger. These larger terms make the least squares solution more sensitive to imperfections in the autocovariance column matrix, Eq. (2.5), which occur with finite length data sets. Increasing the number of lags decreased the sensitivity of Q_w and R_v to errors in the autocovariance column matrix.

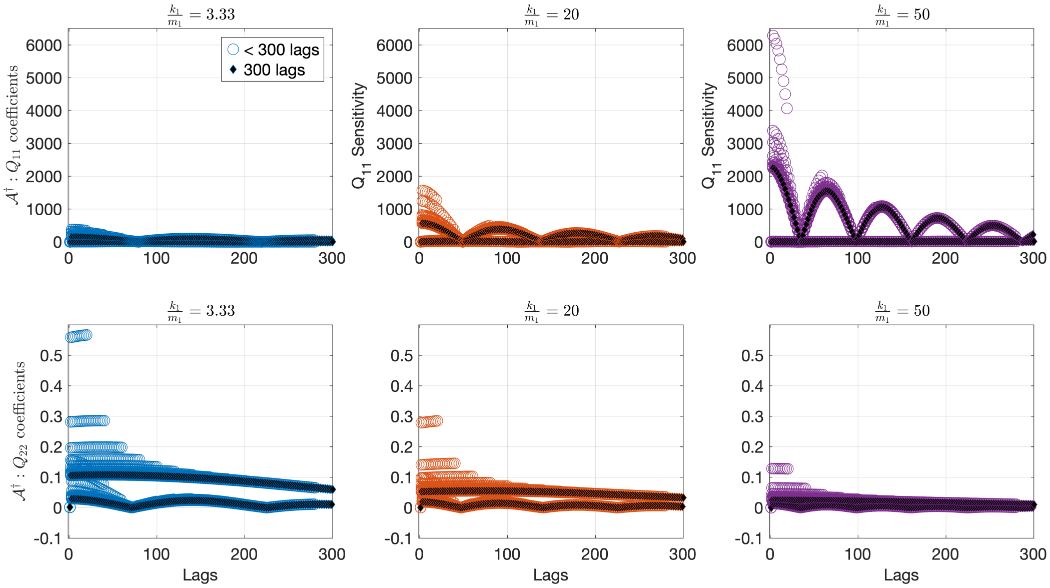

Figure 3.5: Coefficients of sensitivity to errors in autocovariance column matrix.

3.2 Colored Noise Kalman Filter

Atmospheric turbulence as modeled in Eq. (1.25) and Eq. (1.26) with a non-constant spectral density is considered as *colored* process noise. In Lewis [17] and Crassidis [1], an augmented state shaping filter is proposed for the case of non-white process noise. Using spectral factorization theorem, $\Phi(z)$ can be restated as,

$$\Phi(z) = H(z)H^T(z^{-1}) \tag{3.13}$$

where $H(z)$ is a square, rationale, asymptotically stable spectral factor. When $H(z)$ is driven by white noise its output will have spectral density, $\Phi(z)$. Given a state realization for $H(z)$,

$$H(z) = H'(zI - A')^{-1}G' + D', \tag{3.14}$$

then the noise, w_k can be represented as,

$$\begin{aligned} x'_{k+1} &= A'x'_k + G'w'_k \\ w_k &= H'x'_k + D'w'_k. \end{aligned} \tag{3.15}$$

Combining the ALS approach to noise covariance identification and the colored noise shaping filter, we construct a Kalman filter for atmospheric gust estimation. In Eq. (1.1), the control, u_k can be divided into aircraft control surface inputs and atmospheric inputs, $[B]u_k = [B_{cs} \quad B_g][u_{cs} \quad u_g]^T$ and $[D]u_k = [D_{cs} \quad D_g][u_{cs} \quad u_g]^T$. Then letting $GH' = B_g$ and $GD' = 0$. To model the atmospheric disturbance as colored noise instead of as an input, we augmenting Eq. (1.1) with Eq. (3.15),

$$\begin{aligned} \begin{bmatrix} x_{k+1} \\ x'_{k+1} \end{bmatrix} &= \begin{bmatrix} A & B_g \\ 0 & A' \end{bmatrix} \begin{bmatrix} x_k \\ x'_k \end{bmatrix} + \begin{bmatrix} B_{cs} \\ 0 \end{bmatrix} u_{cs} + \begin{bmatrix} G & 0 \\ 0 & G' \end{bmatrix} \begin{bmatrix} w_k & w'_k \end{bmatrix} \\ z_k &= \begin{bmatrix} C & D_g \end{bmatrix} \begin{bmatrix} x_k \\ x'_k \end{bmatrix} + D_{cs} u_{cs} + v_k \end{aligned} \tag{3.16}$$

where the last element of the process noise, w'_k, is uncorrelated with v_k. For the flexible aircraft in atmospheric turbulence, the shaping filter is chosen as a two state random bias filter, $x_{k+1} = 0$, with the following format,

$$\begin{bmatrix} x'_{k+1} \end{bmatrix} = \begin{bmatrix} \chi'_{1,k+1} \\ \chi'_{2,k+1} \end{bmatrix} = \begin{bmatrix} 1 & \Delta t \\ 0 & 1 \end{bmatrix} \begin{bmatrix} \chi'_{1,k} \\ \chi'_{2,k} \end{bmatrix} + \begin{bmatrix} 0 & 0 \\ 0 & 1 \end{bmatrix} w'_k. \tag{3.17}$$

Other shaping filters such as the Dryden model, Eq. (1.25), or a low pass filter approximation could be explored as alternative candidates. The random bias shaping filter was chosen for simplicity. The noise covariances, $E\left[w_k w_k^T\right]$ and $E\left[v_k v_k^T\right]$ are the solutions to the ALS problem for the aircraft flying in smooth air. For and aircraft flying in turbulent air, the augmented state will capture the dynamics of the colored noise disturbance.

Illustrative Example

To demonstrate a colored noise Kalman filter for disturbance estimation, consider the mass-spring-damper system shown in Fig. 3.6.

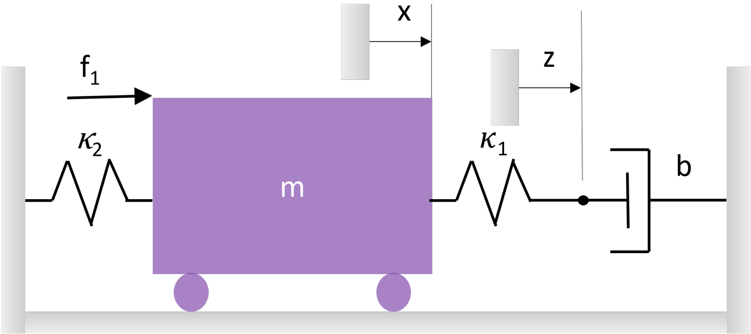

Figure 3.6: Mass-spring-damper schematic.

The dynamics of this system are modeled as,

$$\begin{bmatrix} \dot{x} \\ \ddot{x} \\ \dot{z} \end{bmatrix} = \begin{bmatrix} 0 & 1 & 0 \\ -\frac{\kappa_1+k_2}{m} & 0 & \frac{\kappa_1}{m} \\ \frac{\kappa_1}{b} & 0 & -\frac{\kappa_1}{b} \end{bmatrix} \begin{bmatrix} x \\ \dot{x} \\ z \end{bmatrix} + \begin{bmatrix} 0 \\ \frac{1}{m} \\ 0 \end{bmatrix} f_1(t) + \begin{bmatrix} 0 & 0 \\ 1 & 0 \\ 0 & 1 \end{bmatrix} w(t)$$
$$y = \begin{bmatrix} 0 & 0 & 1 \end{bmatrix} \begin{bmatrix} x \\ \dot{x} \\ z \end{bmatrix} + v_k, \tag{3.18}$$

where $m = 5$, $k_1 = 5$, $k_2 = 10$, and $b = 0.7$. The process noise, $w(t)$, and the measurement noise, $v(t)$, are white noise processes with covariances,

$$Q = \begin{bmatrix} 0.2 & 0 \\ 0 & 0.2 \end{bmatrix}, \quad R = 0.5. \tag{3.19}$$

The colored noise Kalman filter state space model is defined as,

$$\begin{bmatrix} \dot{x} \\ \ddot{x} \\ \dot{z} \\ \dot{\chi} \end{bmatrix} = \begin{bmatrix} 0 & 1 & 0 & 0 \\ -\frac{\kappa_1+k_2}{m} & 0 & \frac{\kappa_1}{m} & \frac{1}{m} \\ \frac{\kappa_1}{b} & 0 & -\frac{\kappa_1}{b} & 0 \\ 0 & 0 & 0 & 0 \end{bmatrix} \begin{bmatrix} x \\ \dot{x} \\ z \\ \chi \end{bmatrix} + \begin{bmatrix} 0 & 0 & 0 \\ 1 & 0 & 0 \\ 0 & 1 & 0 \\ 0 & 0 & 1 \end{bmatrix} \begin{bmatrix} w(t) & w'(t) \end{bmatrix}$$

$$y = \begin{bmatrix} 0 & 0 & 1 & 0 \end{bmatrix} \begin{bmatrix} x \\ \dot{x} \\ z \\ \chi \end{bmatrix} + v_k, \tag{3.20}$$

where χ is the augmented state shaping filter modeled as a random bias filter. For this simulated example, the true covariances are used, with the third diagonal element of the process noise covariance matrix, Q_w, arbitrarily chosen as 10. The resulting state estimates are shown in Fig. 3.7. The ideal Kalman filter, with known noise covariances and knowledge of the input disturbance is shown in gold. As expected, the ideal Kalman filter estimate error meets the 3σ error covariance bounds shown by black dashed lines. The colored noise Kalman filter, with known noise covariances and no knowledge of the the input disturbance is shown in orange. The colored noise estimate of the input, shown on the top for Fig. 3.7, tracks the disturbance well, with a delay. The colored noise state estimates exhibit slightly larger errors that the ideal estimates. Notably, the $\dot{\hat{x}}$ estimate displays an increase in error when the input is ramped in and out. The increase in error is expected for the sub-optimal colored noise Kalman filter. The measurement and measurement estimates are shown in Fig. 3.8. The innovations from both of the Kalman filters fall with in the expected 3σ bounds, $CPC^T + R$, for most of the 50 second simulation.

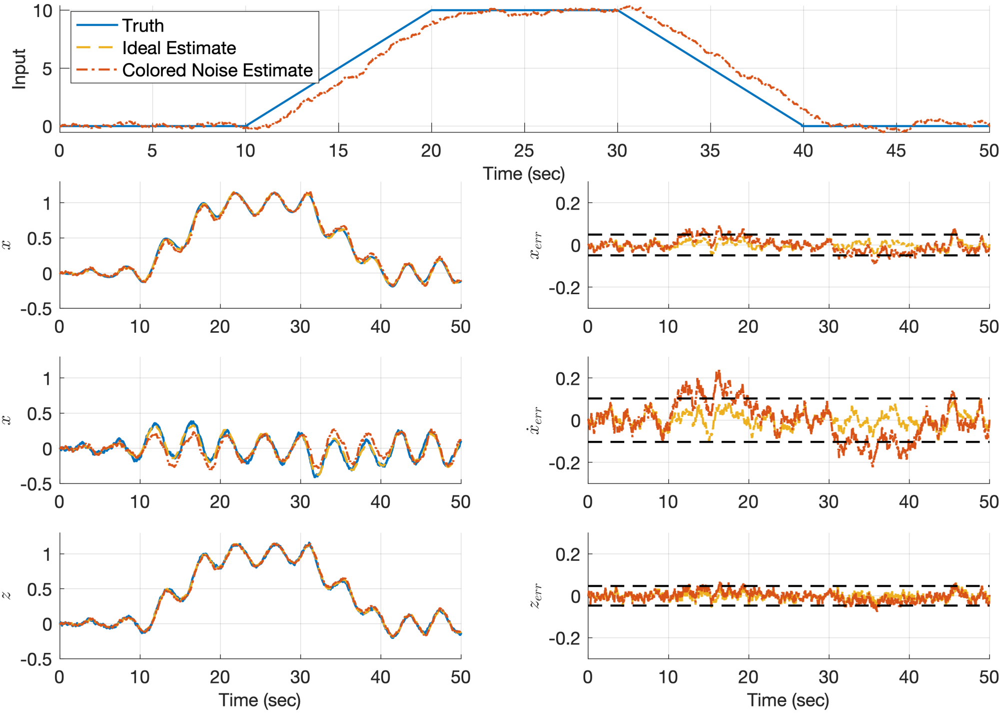

Figure 3.7: Colored noise state estimates for mass-spring-damper.

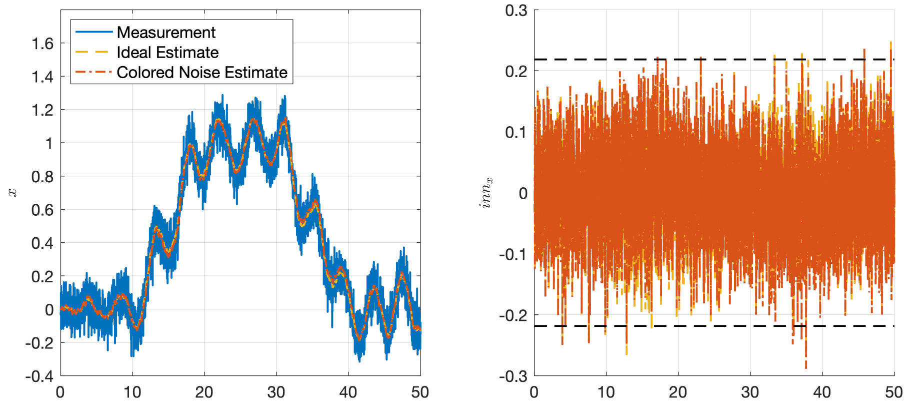

Figure 3.8: Colored noise measurement estimates for mass-spring-damper.

3.3 Model Uncertainty

A K-L divergence metric is proposed to assess the performance of a Kalman filter and characterize uncertainty relative to a given model, [83]. When ALS identified process and measurement noise covariances are used for estimator design, the K-L divergence metric indicates the level of model uncertainty. It will be shown here that the quality of an estimate can be used as a tool to identify uncertainty sources in the model used to generate the estimate. In some cases the metric points to adjusting model parameters and in others it indicates a need to adjust the modeling approach.

The literature contains numerous established techniques for system identification from test data. These consistently rely on test data collected during specific maneuvers with specific excitation inputs. In contrast, this technique prefers steady state data of the vehicle operating without specific inputs. General operating data is sufficient instead of a dedicated test campaigns for system identification.

A K-L divergence state estimate performance metric,

$$\begin{aligned}
\Sigma_t =& CPC^T + R \\
\Sigma_m =& \frac{1}{N_d} \sum_{i=1}^{N_d} \mathscr{Y}_k \mathscr{Y}_k^T \\
E_{opt} =& \frac{1}{2} (\mathrm{tr}(\Sigma_t^{-1} \Sigma_m) + (\mu_t - \mu_m)^T \Sigma_t^{-1} (\mu_t - \mu_m) - k + \ln \frac{\det(\Sigma_t)}{\det(\Sigma_m)}
\end{aligned} \tag{3.21}$$

where k is the number of measurements and μ is the mean of the measurements, is used to assess estimator performance. For an optimal estimate, the measured error covariance, Σ_m, of an estimate will be equivalent to the theoretical error covariance, Σ_t. When the estimate is not optimal, the sub-optimal performance is quantified by the K-L divergence metric as a function of the two multivariate normal distributions [86]. A smaller E_{opt} value indicates a more optimal estimate.

In practical applications, the dynamic model is not perfectly known. When there are errors in the state-space model used for ALS identification of noise covariances matrices, the identified process noise covariance will compensate for those errors in the model. The result is a set of sub-optimal estimates. In the upcoming examples it will be demonstrated that ALS can be combined with this K-L divergence metric to select a more accurate dynamic model and improve estimate accuracy.

Illustrative Example

In order to demonstrate the use of the K-L divergence metric to characterize model error, consider the mass-spring-damper system from Eq. (3.18). For this example, the damping, b, is unknown to the Kalman filter designer. Eight Kalman filters were defined for eight state-space models with consistent $k_1 = 1$, $k_2 = 2$, $m = 5$, and variation in damping, $b = [0.5,\ 1,\ 1.5,\ 2,\ 2.5,\ 3,\ 3.5,\ 4]$. Two hundred simulated linear dynamic data sets were generated with Eq. (3.18).

The ALS problem was solved for 200 data sets in each damping group up to 400 lags. In Fig. 3.9 each of these solutions is shown with a grey '+', the mean of the solutions for each lag is shown with a bold '×', and the standard deviation is shaded. The true simulated covariance is denoted by the black line. The mean of each solution set at 400 lags is shown in Table 3.1, where the first row is the simulated covariance. The rows of the table are shaded to correspond with Fig. 3.9. Notice that the identified process noise covariance changes significantly to account for error between the simulated dynamics and the Kalman filter model. In comparison, the measurement noise covariance variation is much smaller. The dynamic models with larger errors have larger standard deviation in their solutions and the mean drifts with increasing lags, instead of converging to a consistent value. When an accurate dynamic model is used, ALS correctly identifies the noise covariances.

Eight Kalman filters are designed with the identified Q_w and R_v matrices. The performance of these Kalman filters is compared for four input profiles: a step, a doublet, a frequency chirp, and a frequency dwell in Fig. 4.40. Each of the Kalman filters is evaluated for each input profile using the K-L divergence metric, Eq. (3.21). A smaller E_{opt} indicates a higher performing estimate. For all of the input profiles the accurate model has the lowest E_{opt} and the E_{opt} value increases as the error in the model increases. Notice that for the accurate model, $b = 2$, the value of E_{opt} is approximately constant for all input profiles. In this simulated case, where the model is exact and the noise is zero mean, white noise, this result approaches optimal. The models with error have variation in the E_{opt} because some input profiles expose the modeling error more than others input profiles.

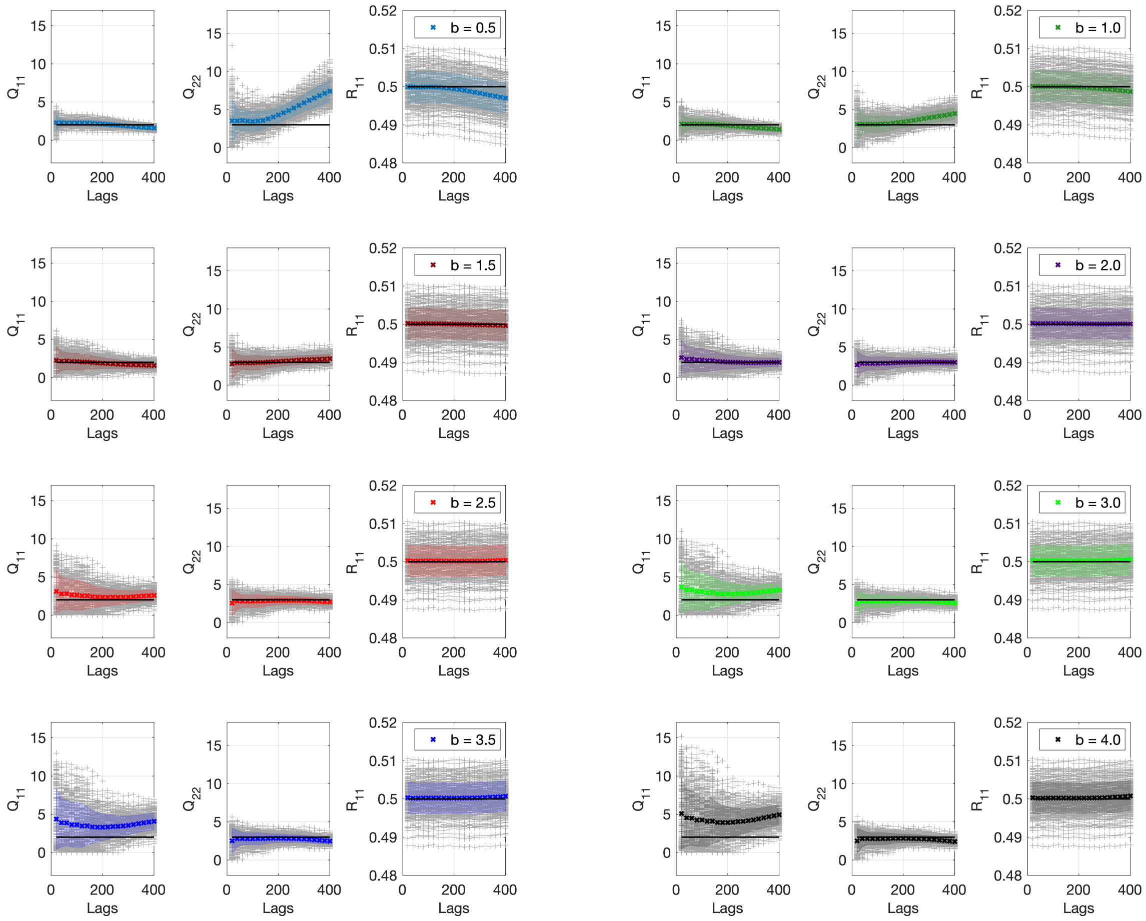

Figure 3.9: Identified noise covariances, Q_w & R_v, for each model variation ('+' represents each solution, shading represents standard deviation, and '×' represents mean of solutions).

Table 3.1: Simulated and identified noise covariances.

Damping (b)	Q_{11}	Q_{22}	R
Simulated	**2**	**3**	**0.5**
0.5	1.570	7.407	0.497
1.0	1.405	4.474	0.499
1.5	1.587	3.473	0.500
2.0	2.004	2.998	0.500
2.5	2.584	2.738	0.500
3.0	3.282	2.582	0.501
3.5	4.070	2.485	0.501
4.0	4.926	2.421	0.501

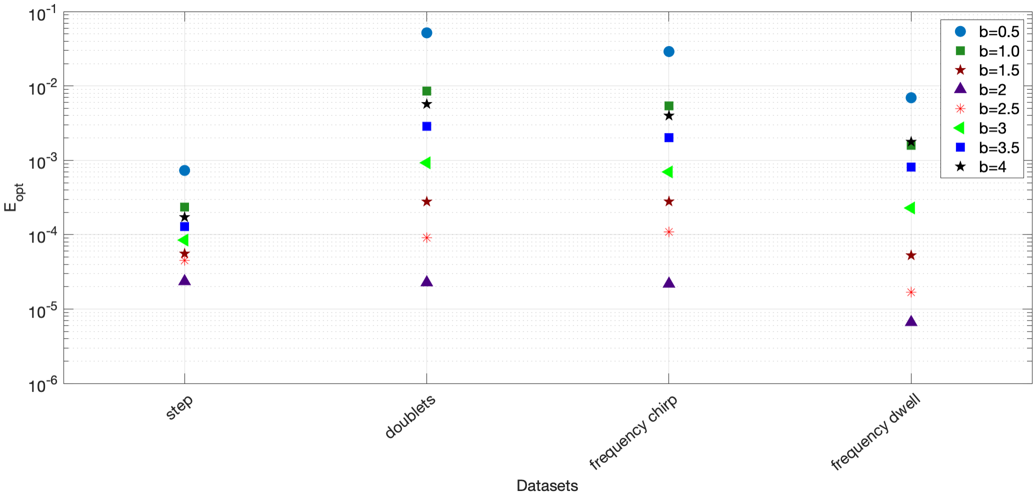

Figure 3.10: Optimality comparison by input type.

3.4 Additional Constraints

The ALS problem, Eq. (2.10), is extended to simultaneously identify noise covariances at multiple operating conditions by including a noise covariance constraint. As an example of where this scenario may be relevant, consider an aircraft where a physics-based analytical model is developed at multiple operating conditions subject to a common set of assumptions. Deviations between the model and the true system may exist for reasons including inaccuracies in an aerodynamic derivative or a linear approximation of nonlinear dynamics. These deviations may be captured in a state space model as part of the system process noise. Further, the covariance of this process noise may have a parameterized structure that can be identified. The noise covariance constraint becomes a model that informs the Kalman gain design for the set of operating conditions. The approach is demonstrated to be viable by convergence of the ALS algorithm over the set of operating conditions. Additionally, when the model fits the data well, interpolation for the Kalman gain at operating conditions in between the ALS solution conditions is feasible. In this section, we provide the mathematical structure we are considering for the set of system models corresponding to different operating conditions as well as the allowed structure of the process noise covariance that we will explore.

Consider a series of linear discrete systems, $\Sigma_i = (A_i, B_i, C_i)$, $i = 1, \ldots, n$, where

$$\begin{aligned} x_{k+1} &= A_i x_k + B_i u_k + G w_k \\ y_k &= C_i x_k + v_k \end{aligned} \tag{3.22}$$

with state, $x_k \in \mathbb{R}^n$, control, $u_k \in \mathbb{R}^m$, process disturbance model, $G \in \mathbb{R}^{n \times g}$, process noise, $w_k \in \mathbb{R}^g$, measurements $y_k \in \mathbb{R}^p$, and measurement noise, $v_k \in \mathbb{R}^p$.

Assumption 4 *For each system, i, w_k and v_k, are uncorrelated zero-mean, Gaussian white-noise processes with constant covariance matrices, Q_i and R_i.*

Additionally, the noise covariances are constrained such that,

$$\begin{aligned} Q_i &= Q_0 + Q_\lambda \lambda_i \\ R_i &= R_0 + R_\lambda \lambda_i, \end{aligned} \tag{3.23}$$

where $\lambda_i \in \mathbb{R}$ is a parameter that varies throughout the series $i = 1, \ldots, n$. The noise covariance model terms, $Q_0 \in \mathbb{R}^{g\times g}$, $Q_\lambda \in \mathbb{R}^{g\times g}$, $R_0 \in \mathbb{R}^{p\times p}$, $R_\lambda \in \mathbb{R}^{p\times p}$, are the unknown constants to be solved for in the constrained ALS problem.

Following the standard ALS algorithm from Chapter 2, without the noise covariance constraints given in Eq. (3.23). The least squares objective function for a single operating condition, i, is,

$$\phi(Q_i, R_i) = \min_{Q_i, R_i} \left\| \mathscr{A}_i \begin{bmatrix} (Q_i)_{ss} \\ (R_i)_{ss} \end{bmatrix} - \hat{b}_i \right\|_2^2 . \tag{3.24}$$

Next, Eq. (3.24) is expanded to simultaneously solve for the set of operating conditions, $i = 1, \ldots, n$.

$$\phi(Q, R) = \left\| \begin{bmatrix} \mathscr{A}_1 & & 0 \\ & \ddots & \\ 0 & & \mathscr{A}_n \end{bmatrix} \begin{bmatrix} (Q_1)_{ss} \\ (R_1)_{ss} \\ \vdots \\ (Q_n)_{ss} \\ (R_n)_{ss} \end{bmatrix} - \begin{bmatrix} \hat{b}_1 \\ \vdots \\ \hat{b}_n \end{bmatrix} \right\|_2^2 . \tag{3.25}$$

The noise covariance terms for the set of systems, Σ_i, are then found from the solution to the constrained optimization problem formulated as,

$$\begin{aligned} \min_{Q,R} \quad & \phi(Q, R) \\ \text{s.t.} \quad & Q_i = Q_0 + Q_\lambda \lambda_i \\ & R_i = R_0 + R_\lambda \lambda_i, \ \forall i \\ & Q_i \geq 0 \\ & R_i \geq 0. \end{aligned} \tag{3.26}$$

Illustrative Example

Consider the mass-spring-damper system described by Eq. (3.18) and pictured in Fig. 3.6 where $\kappa_1 = 1$, $\kappa_2 = 2$, $m = 5$, and w_k and v_k are white noise processes. For this example seven operating conditions will be considered where the coefficient of damping, b, is known to vary with temperature and is modeled as $b = [1, \ldots, 7]$.

The ALS problem was formatted to be solved simultaneously at all of operating conditions. The diagonal elements of the process noise covariance, Q_w, were constrained to follow affine model as a function of temperature, T, and the measurement noise covariance was constrained to be invariant with temperature,

$$\begin{aligned} Q_{11} &= Q_{10} + Q_{1T}T_i \\ Q_{22} &= Q_{20} + Q_{2T}T_i \\ R &= R_i, \quad \forall i. \end{aligned} \tag{3.27}$$

In this simulated example, 100 data sets were generated at each of the seven operating conditions. These data sets were recorded at 100 Hz and were 300 seconds in length. The ALS problem for the set of operating conditions, Eq. (3.25), constrained by Eq. (3.27), was solved up to 600 lags. The results for the terms of the process noise covariance model were shown in Fig. 3.11 and Fig. 3.12 and where the grey '+' represented the solutions to each individual ALS problem, the blue '×' represented the mean of the solutions, and the shading represented the standard deviation of the solutions. The simulated truth was shown with the black line.

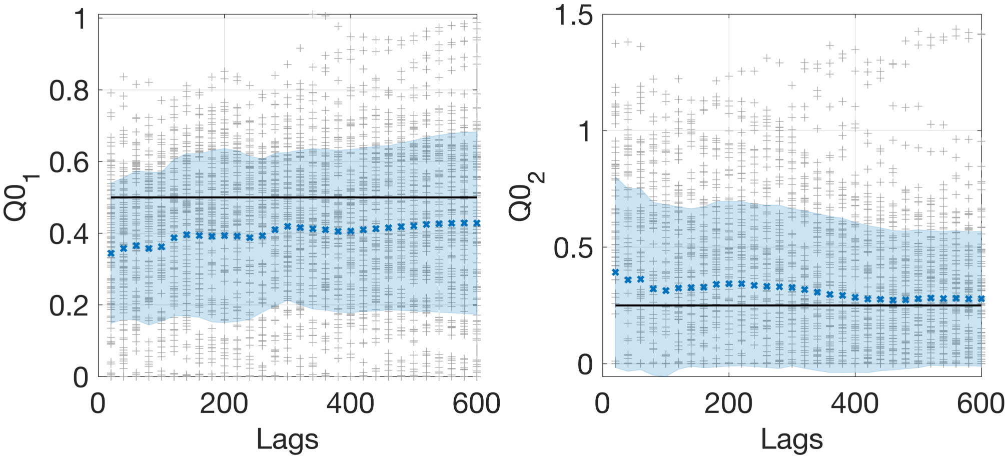

Figure 3.11: Mass-spring-damper: Constrained ALS identified Q_{i0}.

An overview of the full series of ALS solutions is shown in Fig. 3.13. The constrained solutions aligned well with the simulated truth across the operating conditions.

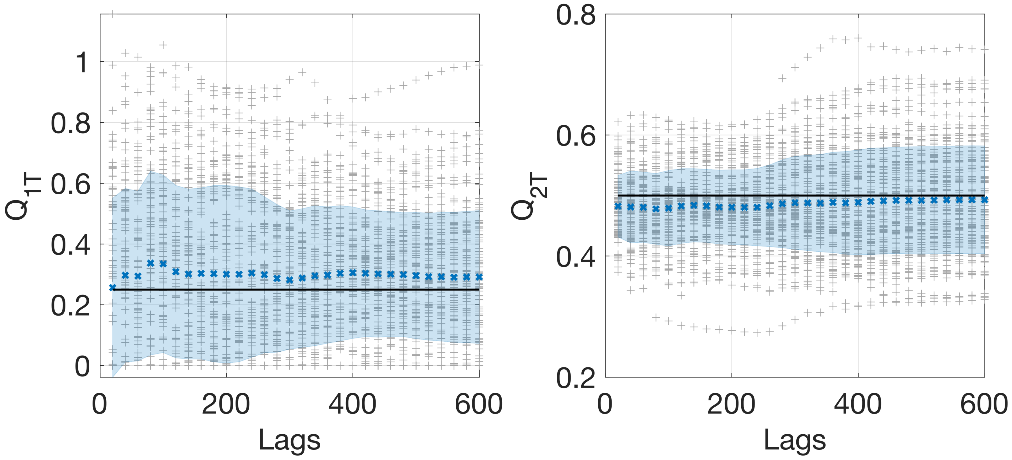

Figure 3.12: Mass-spring-damper: Constrained ALS identified Q_{iT}.

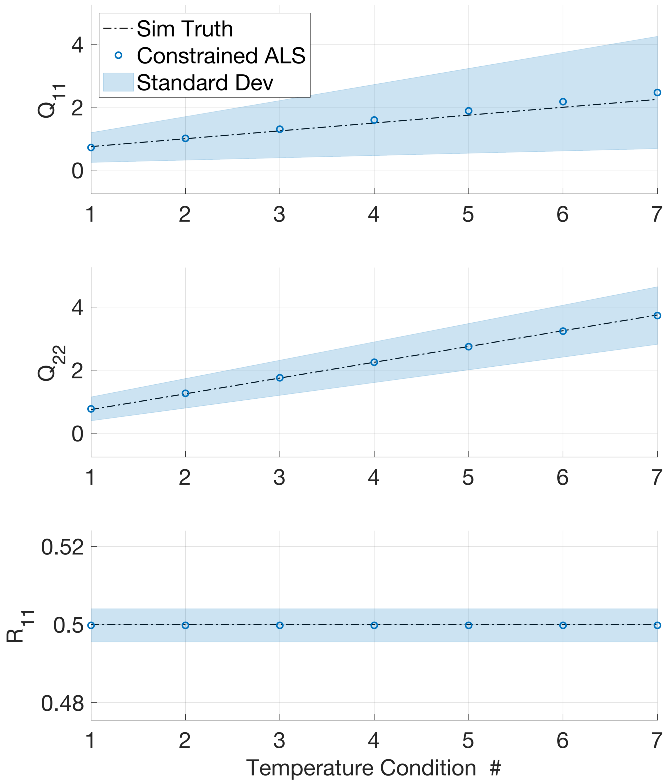

Figure 3.13: Mass-spring-damper: Constrained ALS identified covariances at 7 temperatures.

Chapter 4

AEROSPACE APPLICATIONS

In this chapter the ALS extensions described in Chapter 3 are applied to aerospace platforms. Four vehicles are considered, two wind tunnel test-beds and two conventional aircraft. The University of Washington has developed two gust load alleviation test-beds, one for the 3 ft × 3 ft wind tunnel and one for the Kristen Wind Tunnel. The first aircraft is a simulation of the rigid body dynamics of a narrow body commercial aircraft and the second is a flexible wide body commercial aircraft. For each vehicle, Kalman filters designed with ALS identified noise covariances, demonstrate the contributions of this dissertation: sensor selection and management, atmospheric disturbance characterization, and model uncertainty characterization.

4.1 Narrow Body Commercial Aircraft

In a collaboration between University of Washington, the Boeing ecoDemonstrator program, the Boeing Commercial Airplane Flight Controls organization, and the Joint Center for Aerospace Technology Innovation an investigation of the application of ALS to a typical commercial aircraft was conducted. This collaboration investigated the use of ALS to design estimation algorithms of aircraft states from independent sensor sources. An approximate model of the 2021 Boeing ecoDemonstrator, shown in Fig. 4.1, was used in this application. For this example, inertial sensor measurements were filtered to estimate the aircraft angle of attack. The estimated angle of attack was sourced from a different set of sensors installed on a different area of the aircraft and thus independent (i.e. robust against common failures) from the vane measured angle of attack. This estimate could be used in a sensor selection algorithm to monitor the primary sensor health.

The longitudinal dynamics of a typical commercial aircraft was linearly modeled about a trim

Figure 4.1: Boeing 2021 ecoDemonstrator, [87].

condition as,

$$\begin{bmatrix} V_{k+1} \\ \alpha_{k+1} \\ q_{k+1} \\ \theta_{K+1} \end{bmatrix} = A \begin{bmatrix} V_k \\ \alpha_k \\ q_k \\ \theta_k \end{bmatrix} + Bu_k + Gw_k, \qquad \begin{bmatrix} \theta_k \\ q_k \\ n_{xk} \\ n_{yk} \end{bmatrix} = C \begin{bmatrix} V_k \\ \alpha_k \\ q_k \\ \theta_k \end{bmatrix} + v_k, \tag{4.1}$$

where V was the calibrated airspeed, α was the angle of attack, q was the pitch rate, θ was the pitch angle, n_x was the longitudinal acceleration, and n_z was the normal acceleration. The input vector, u_k, was comprised of the control surface deflections, thrust, and gust inputs. This commercial aircraft had multiple sets of measurements available for feedback control, the four outputs in Eq. (4.1) were specifically selected as they all came from an inertial sensor suite. The longitudinal rigid body dynamics of a typical aircraft consisted of two oscillatory modes; the phugoid mode and the short period mode, [8]. For this commercial aircraft model, the phugoid mode had a frequency on the order of 0.01 Hz and the short period mode had a frequency on the order 0.50 Hz.

The time invariant ALS approach from Chapter 2 was demonstrated in this subsection. Using an approximate linear longitudinal dynamic aircraft model, two families of simulated data were created. The first set had a diagonal process noise covariance and the second set had a symmetric process noise covariance with non-zero terms off the diagonal. The measurement noise covariance matrix was diagonal for both sets. The simulated data sets had a time step of 0.1 sec. First, 50 simulated data sets, 2000 seconds in length were generated with diagonal noise covariance matrices,

$$Q = \begin{bmatrix} 12.0 & 0 & 0 \\ 0 & 0.5 & 0 \\ 0 & 0 & 2.0 \end{bmatrix}, \qquad R = \begin{bmatrix} 1.0 & 0 & 0 & 0 \\ 0 & 3.0 & 0 & 0 \\ 0 & 0 & 0.3 & 0 \\ 0 & 0 & 0 & 0.15 \end{bmatrix}. \tag{4.2}$$

The measurements and innovations of an example data set are shown in Fig. 4.2.

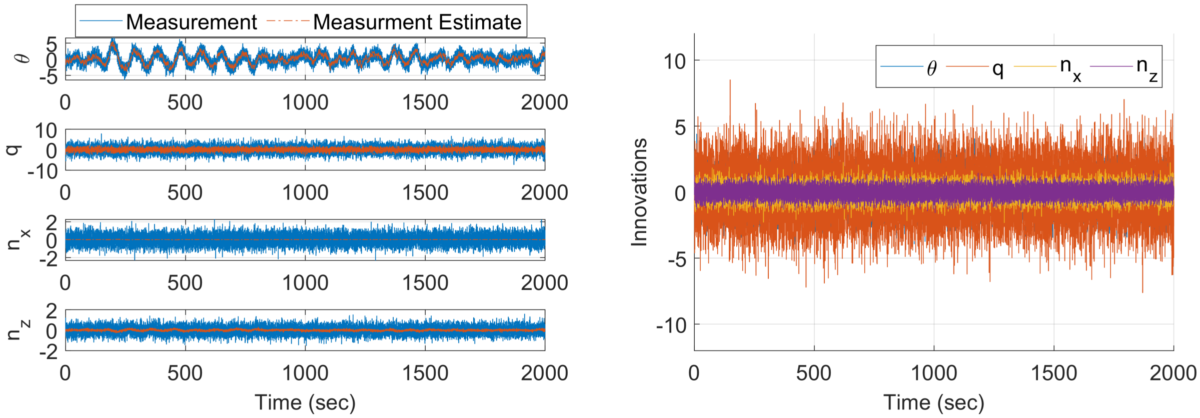

Figure 4.2: Example simulated data set for ecoDemonstrator ALS problem.

The innovations were for the initial, suboptimal Kalman gain based on Eq. (1.3) and Eq. (1.4) with,

$$Q = \begin{bmatrix} 1 & 0 & 0 \\ 0 & 1 & 0 \\ 0 & 0 & 1 \end{bmatrix}, \qquad R = \begin{bmatrix} 1 & 0 & 0 & 0 \\ 0 & 1 & 0 & 0 \\ 0 & 0 & 1 & 0 \\ 0 & 0 & 0 & 1 \end{bmatrix}. \tag{4.3}$$

As desired, the innovations were zero mean. The least squares problem was solved first as a quadratic programming problem and next as a semidefinite programming problem. In the first example, with a diagonal process noise covariance matrix, both solutions methods were appropriate. The quadratic programming solution was less computationally demanding. The ALS problem was solved for each data set up to 200 lags, or 20 seconds (approximately 0.2 cycles of the slowest mode) back in time. The quadratic programming solutions are shown in Fig. 4.3 and Fig. 4.4. In these figures each individual solution is shown by a grey '+', the mean of the solutions is shown with a blue '×', and the standard deviation of the solutions is shown with the blue shading. For the quadratic programming approach the identified covariances converged to the true values with minimal errors. The semidefinite programming solutions are shown in Fig. 4.5 and Fig. 4.6. For the semidefinite programming case the off diagonal terms were not constrained to zero. As a result, errors are observed in the solutions, notably the Q_{13}, Q_{23}, Q_{31} and Q_{32} solutions did not converge to their true values. The mean of solutions at 200 lags are are shown in Table 4.1.

Table 4.1: ALS identified noise covariances of a simulated aircraft: diagonal Q_w.

	Simulated	Quadratic Programming	Semidefinite Programming
Q_{11}	12.0	12.0387	13.6930
Q_{12}	0	0	0.0143
Q_{13}	0	0	-0.7733
Q_{21}	0	0	0.0143
Q_{22}	0.5	0.4920	0.5413
Q_{23}	0	0	0.1478
Q_{31}	0	0	-0.7733
Q_{32}	0	0	0.1478
Q_{33}	2.0	2.0528	2.0996
R_{11}	1.0	0.9997	0.9997
R_{22}	3.0	2.9967	2.9965
R_{33}	0.30	0.3000	0.300
R_{44}	0.15	0.1499	0.1498

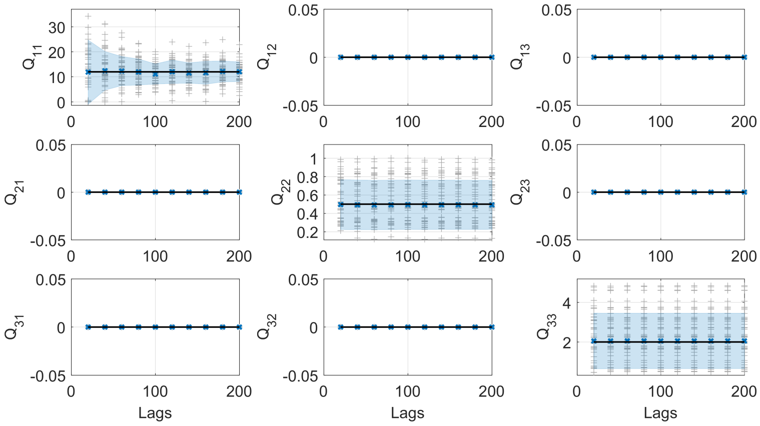

Figure 4.3: Process noise covariance solutions: quadratic programming, diagonal Q_w.

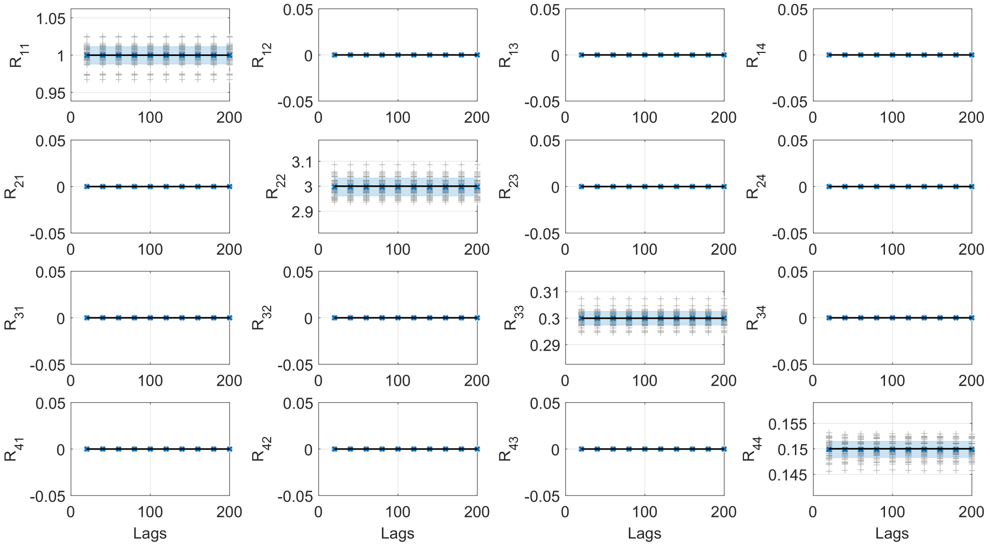

Figure 4.4: Measurement noise covariance solutions: quadratic programming, diagonal Q_w.

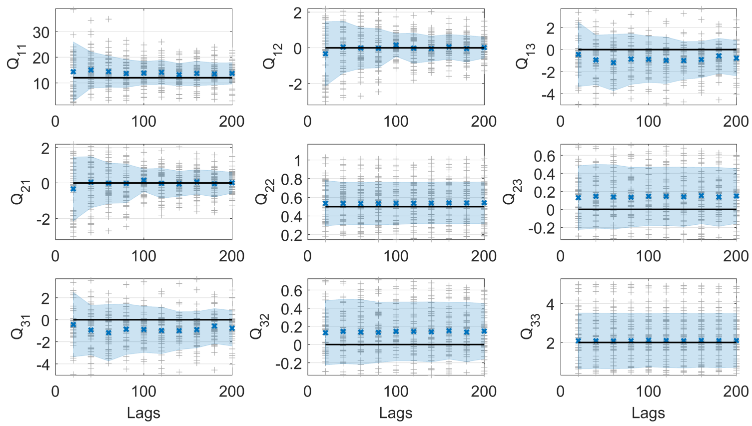

Figure 4.5: Process noise covariance solutions: semidefinite programming, diagonal Q_w.

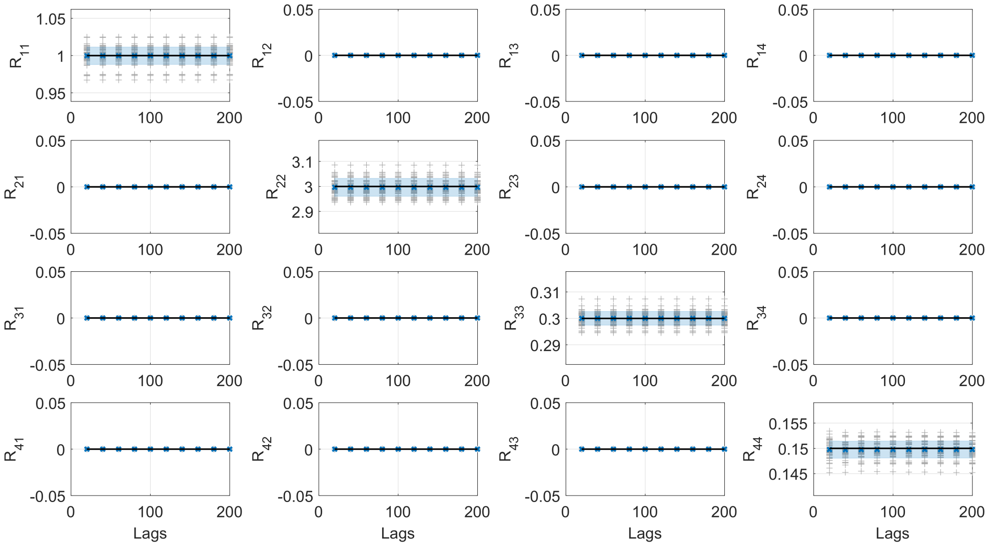

Figure 4.6: Measurement noise covariance solutions: semidefinite programming, diagonal Q_w.

Next, 50 simulated data sets were generated with a symmetric process noise covariance matrix,

$$Q = \begin{bmatrix} 12.0 & 0.1 & 0.4 \\ 0.1 & 0.5 & 0.7 \\ 0.4 & 0.7 & 2.0 \end{bmatrix}, \tag{4.4}$$

and the measurement covariance matrix from Eq. (4.2). The least squares problem was solved first as a quadratic programming problem and next as a semidefinite programming problem. In this second example, the quadratic programming approach was inappropriate, because the non-diagonal least squares problem cannot be simplified to a quadratic programming problem. However, the true structure of the noise covariance matrix was unknown to the designer and the solution approach must be selected based on knowledge of the system and engineering judgment. The quadratic programming solutions are shown in Fig. 4.7 and Fig. 4.8. The off-diagonal terms did not converge to the correct value because the quadratic programming approach assumed they were zero. This incorrect assumption also drove error into the diagonal terms, notably the Q_{22} values converged to the incorrect noise covariance. The semidefinite programming solutions are shown in Fig. 4.9 and Fig. 4.10. For the semidefinite programming approach the identified covariances converged to the true values with minimal errors. The mean of solutions at 200 lags are shown in Table 4.2.

Table 4.2: ALS identified noise covariances of a simulated aircraft: symmetric Q_w.

	Simulated	Quadratic Programming	Semidefinite Programming
Q_{11}	12.0	11.1842	13.5694
Q_{12}	0.1	0	0.1599
Q_{13}	0.4	0	0.2041
Q_{21}	0.1	0	0.1599
Q_{22}	0.5	0.2584	0.4907
Q_{23}	0.7	0	0.6298
Q_{31}	0.4	0	0.2041
Q_{32}	0.7	0	0.6298
Q_{33}	2.0	1.9317	2.0881
R_{11}	1.0	0.9997	0.9997
R_{22}	3.0	2.9968	2.9960
R_{33}	0.30	0.3000	0.3001
R_{44}	0.15	0.1504	0.1499

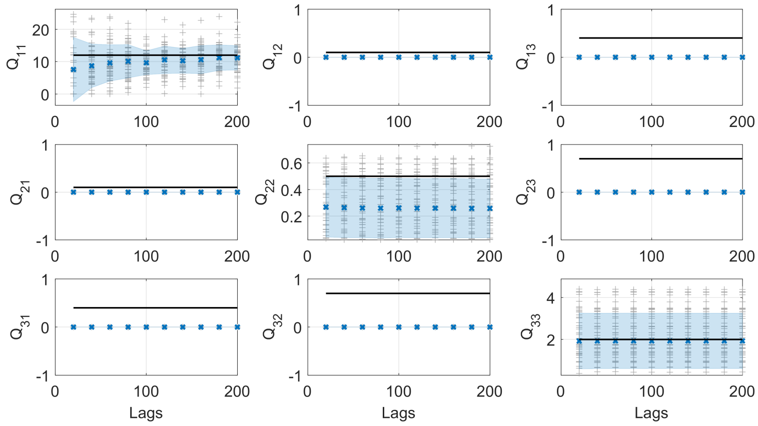

Figure 4.7: Process noise covariance solutions: quadratic programming, symmetric Q_w.

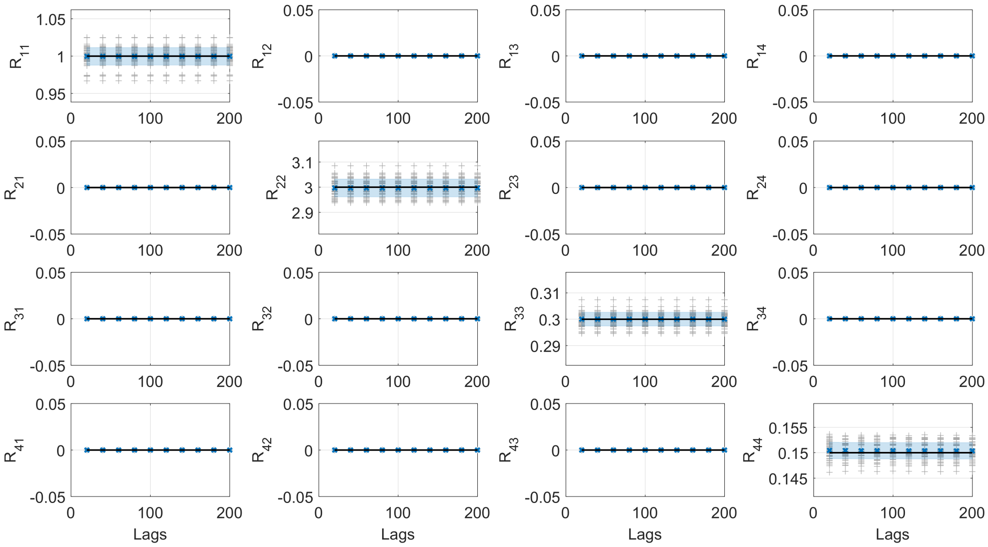

Figure 4.8: Measurement noise covariance solutions: quadratic programming, symmetric Q_w.

Two linear Kalman filters were designed with the ALS identified Q_w and R_v shown in Table 4.2. A comparison of the estimated $\hat{\alpha}$ and vane measured α is shown in Fig. 4.11 for a time history with an oscillatory elevator input. In this example, both estimates tracked the truth and the innovations stay within the 3σ bounds denoted in Fig. 4.11 by black dashed lines.

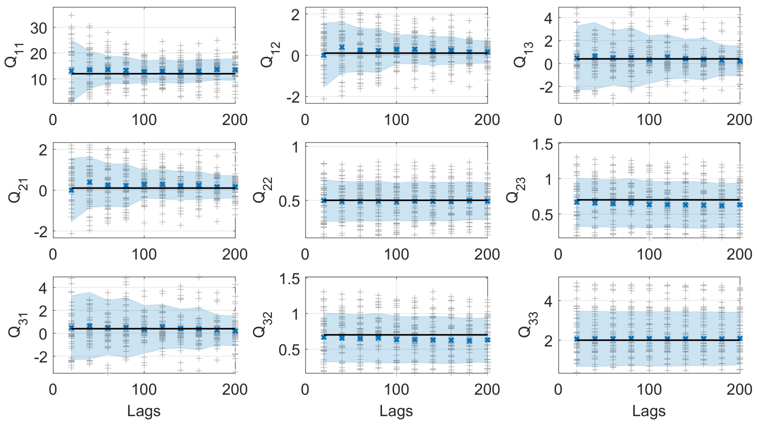

Figure 4.9: Process noise covariance solutions: semidefinite programming, symmetric Q_w.

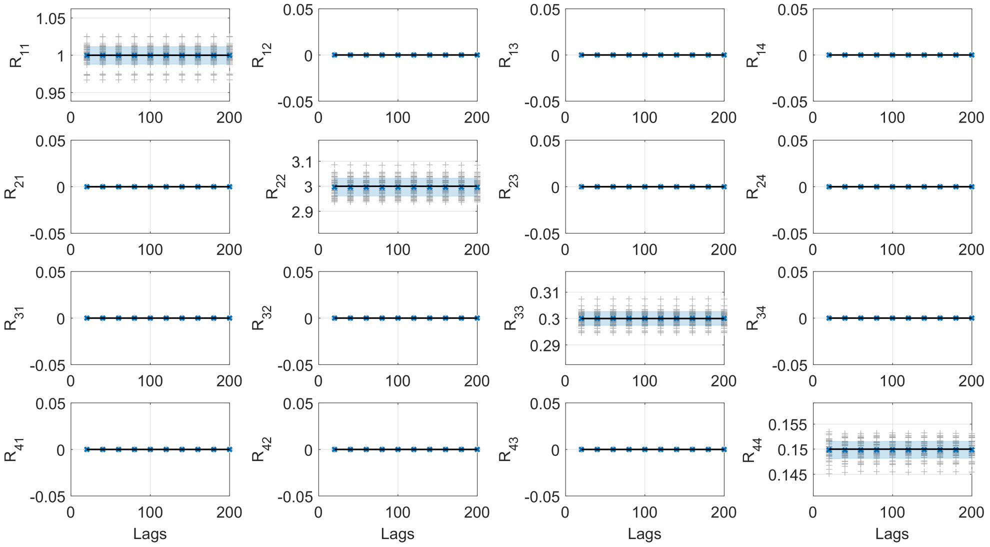

Figure 4.10: Measurement noise covariance solutions: semidefinite programming, symmetric Q_w.

4.1.1 Model Uncertainty

Using the K-L divergence metric, Eq. (3.21) the two Kalman filters for the symmetric process noise case were compared to an ideal Kalman filter tuned with the true process and measurement noise

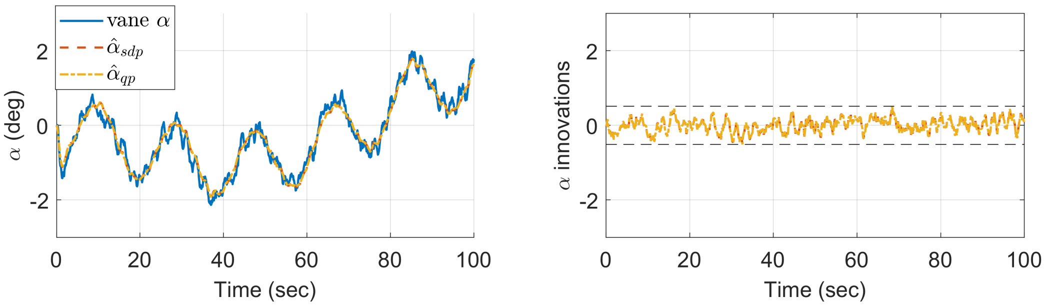

Figure 4.11: Simulated comparison of $\hat{\alpha}$ (from inertial measurements) and vane measured α.

covariances. As shown in Fig. 4.12, all three E_{opt} values were small, indicating good Kalman filter designs. The semidefinite programmings approach was closest to the ideal tuning, the quadratic programming approach was slightly less optimal.

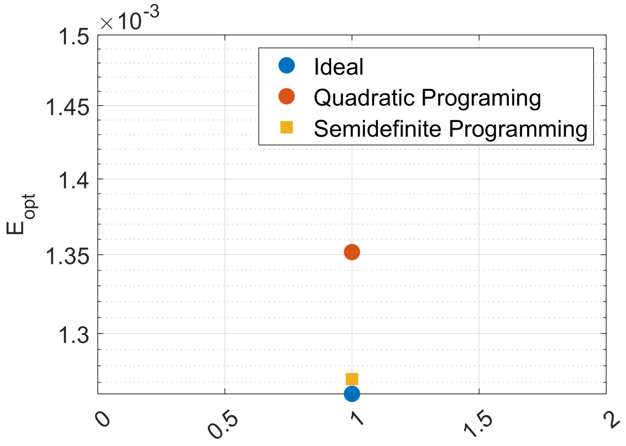

Figure 4.12: Comparison of optimality of estimation.

4.2 Large Wing Wind Tunnel Test-bed

The University of Washington has developed two active control test-beds for gust load alleviation research [88, 89, 90, 82, 91]. The objective was to establish a test-bed for rapid implementation of control algorithms in a repeatable environment. While some control approaches require output feedback, others depend on state feedback. As such, it was desired that each test-bed provide accurate state estimates. The test-bed framework has been established in both the University of Washington 3 ft × 3 ft wind tunnel and the Kirsten Wind Tunnel.

The Kirsten Wind Tunnel Large Wing test-bed, shown in Fig. 4.13, consisted of a half span flexible wing model (originally developed to support NASA's aeroservoelastic research on the variable camber continuous trailing edge flap concept [92, 93]), a gust generation system, and an active control system architecture adapted from the 3 ft × 3 ft wind tunnel test-bed [88]. The highly flexible wing attached at its root to the sidewall of the Kirsten Wind Tunnel. The wing had six actuated trailing edge flaps with control variables denoted $\delta_{f_1}, ..., \delta_{f_6}$. Six sensor bays spanned the wing with bay one closest to the wing root and bay six closest to the wing tip. The test-bed was designed with the ability to select between several sensor configurations. In this work, the sensor set consisted of a total of three accelerometers, two z-direction and one x-direction at the wing tip, following a stability axis with the x-direction into the wind flow, summarized in Table 4.3. The gust generation system was installed at the entrance of the test section and was composed of four synchronous rigid NACA 0015 airfoil vanes spanning the test section horizontally. The gust generation system could generate either a discrete $1 - \cos$ gust or a continuous sinusoidal gust.

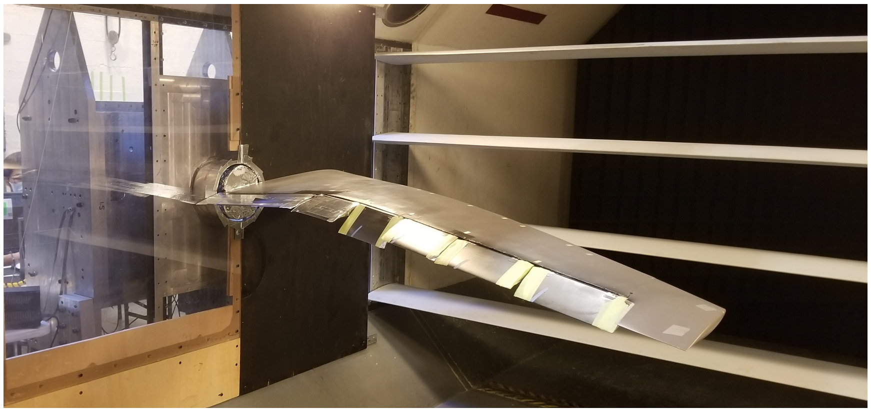

Figure 4.13: Flexible wing and gust generation system of the Kirsten Wind Tunnel test-bed.

An aeroservoelastic model of the flexible wing and gust generation system was modeled using a finite element method and doublet lattice aerodynamics [90, 94]. The unsteady aerodynamic states

Table 4.3: Location and description of sensors.

Measurement	Name	Bay	Location	Orientation
y_1	WT1	6	Forward	z
y_2	WT2	6	Aft	z
y_3	WT3	6	Aft	x

were removed from the model using standard state-space model order reduction techniques. The resulting model had eight states: the four aeroelastic modal displacements and their generalized velocities, seven inputs: the trailing edge flaps and the gust, and three outputs: the sensors in Table 4.3. The four modal frequencies of the analytical model are $\eta = [2.54\,Hz,\ 9.19\,Hz,\ 10.56\,Hz,\ 25.46\,Hz]$.

The resulting model had the form

$$\begin{aligned} x_{k+1} &= Ax_k + Bu_k + Gw_k \\ y_k &= Cx_k + v_k \end{aligned} \tag{4.5}$$

with $x = \begin{bmatrix}\eta_1, \dot{\eta}_1, \eta_2, \dot{\eta}_2, \eta_3, \dot{\eta}_3, \eta_4, \dot{\eta}_4\end{bmatrix}^T$, $u = \begin{bmatrix}\delta_{f_1}, \delta_{f_2}, \delta_{f_3}, \delta_{f_4}, \delta_{f_5}, \delta_{f_6}, \delta_g\end{bmatrix}^T$, and $y = \begin{bmatrix}y_1, y_2, y_3\end{bmatrix}^T$. The state-space matrices, $[A, B, C]$ are provided in Appendix A. The G matrix was defined such that the noise terms enter through the derivative states, [80].

4.2.1 Ill-Conditioned Autocovariance Least Squares

The Kirsten Wind Tunnel Large Wing gust load alleviation test-bed linear analytical model was fully observable. However, construction of the standard ALS problem was ill-conditioned. A study was conducted to understand the impact of output scaling on the accuracy of ALS identified noise covariance, initially with simulated data and then with wind tunnel data. Recall that the optimal weighting of the ALS problem is a function of the true Q_w and true R_v [6]. Therefore the scaling of the simulated problem (with arbitrarily defined noise) is not necessarily appropriate for the real data sets (with unknown noise).

Simulated Evaluation

Fifty data sets were generated at an 100 Hz sample rate by linearly simulating the state space model with random normally distributed process noise and measurement noise with covariances,

$$Q_w = \begin{bmatrix} 1 & 0 & 0 & 0 \\ 0 & 2 & 0 & 0 \\ 0 & 0 & 6 & 0 \\ 0 & 0 & 0 & 3 \end{bmatrix} \times 10^{-2}, \quad R_v = \begin{bmatrix} 9 & 0 & 0 \\ 0 & 6 & 0 \\ 0 & 0 & 4 \end{bmatrix} \times 10^{-5}. \tag{4.6}$$

The ALS problem was solved with a quadratic programming approach for each data set up to 150 lags, or 1.5 seconds back in time (3.8 cycles of the slowest mode), Fig. 4.14. The mean of solutions did not converge to the simulated nose covariances, especially Q_{11} and Q_{33}. To consider

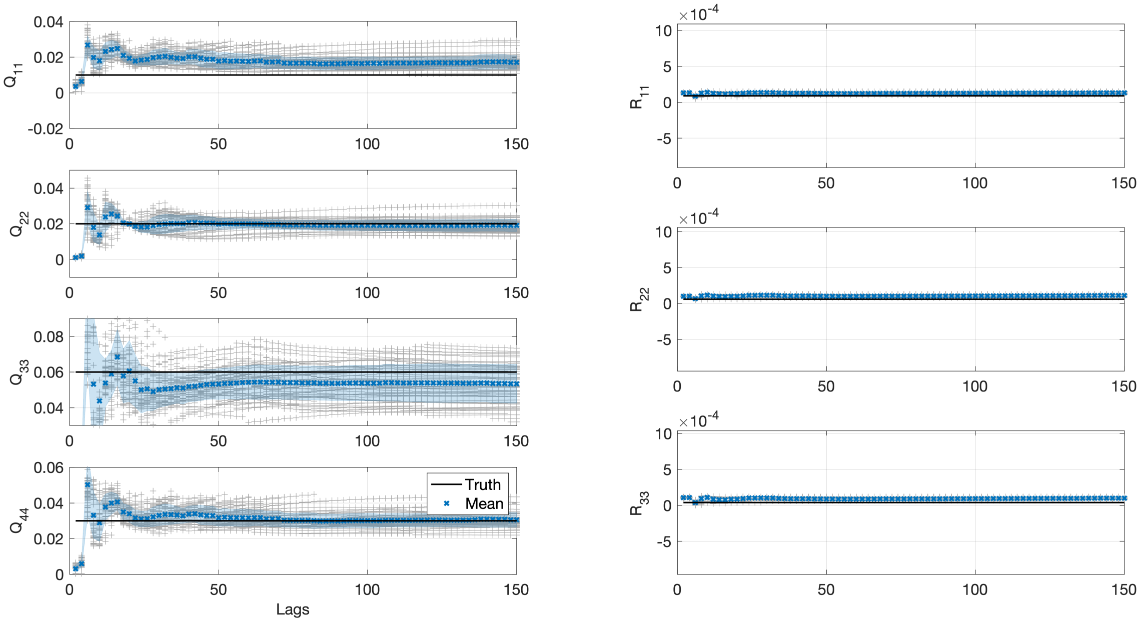

Figure 4.14: Unscaled ALS solutions for the diagonal elements of Q_w (left), and R_v (right).

the conditioning of the ALS problem, the singular values of $\mathscr{A}$ are shown on the left of Fig. 4.15, which result in $\rho_{\mathscr{A}} \geq 10^3$. Notice that the singular values increased with ALS lags initially, but plateau quickly. The three largest singular values were nearly equal (corresponding to the elements of the measurement noise covariance matrix, R_v). The next four singular values were significantly smaller (corresponding to the elements of the process noise covariance matrix, Q_w). A diagonal scaling matrix,

$$\beta = \begin{bmatrix} 10 & 0 & 0 \\ 0 & 200 & 0 \\ 0 & 0 & 1 \end{bmatrix}^{\frac{1}{2}} \tag{4.7}$$

was chosen to improve the conditioning of the ALS problem. Re-evaluating the conditioning, the singular values of $\mathscr{A}_\beta$ are shown on the right of Fig. 4.15, where $\rho_{\mathscr{A}_\beta} < 10^2$ at 150 lags. Now, solving the scaled ALS, Fig. 4.16, showed improved accuracy in the identified process noise and measurement noise covariances. A summary of the ALS solutions with and without scaling is presented in Table 4.4.

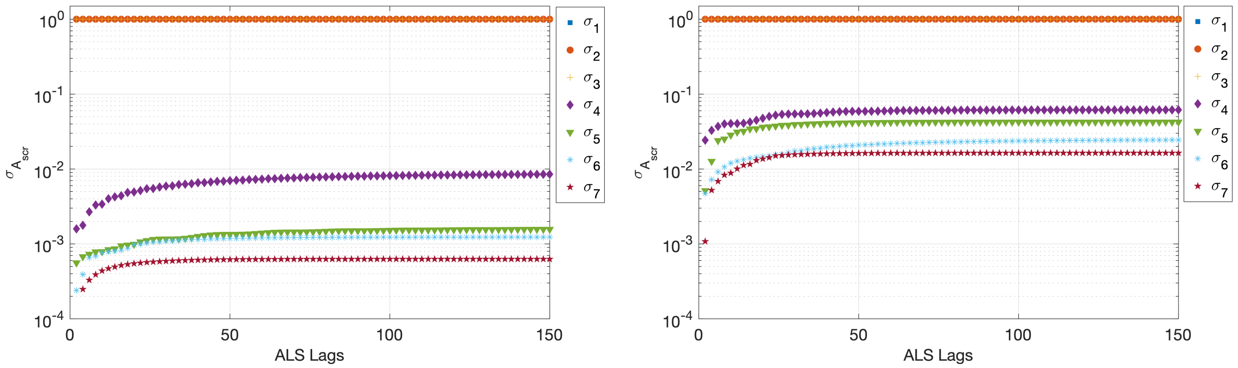

Figure 4.15: Comparison of $\sigma_{\mathscr{A}}$ (left) and $\sigma_{\mathscr{A}\beta}$ (right): Kirsten Wind Tunnel test-bed.

Wind Tunnel Data Evaluation

After the effect of scaling was evaluated for the simulated problem, the scaling on the wind tunnel data sets was evaluated. Inspection of the C matrix guided the initial estimates of scaling matrices. Ultimately the scaling was a balance between improving the conditioning of the least squares problem and corrupting the least squares problem by noise inflation. During a wind tunnel test

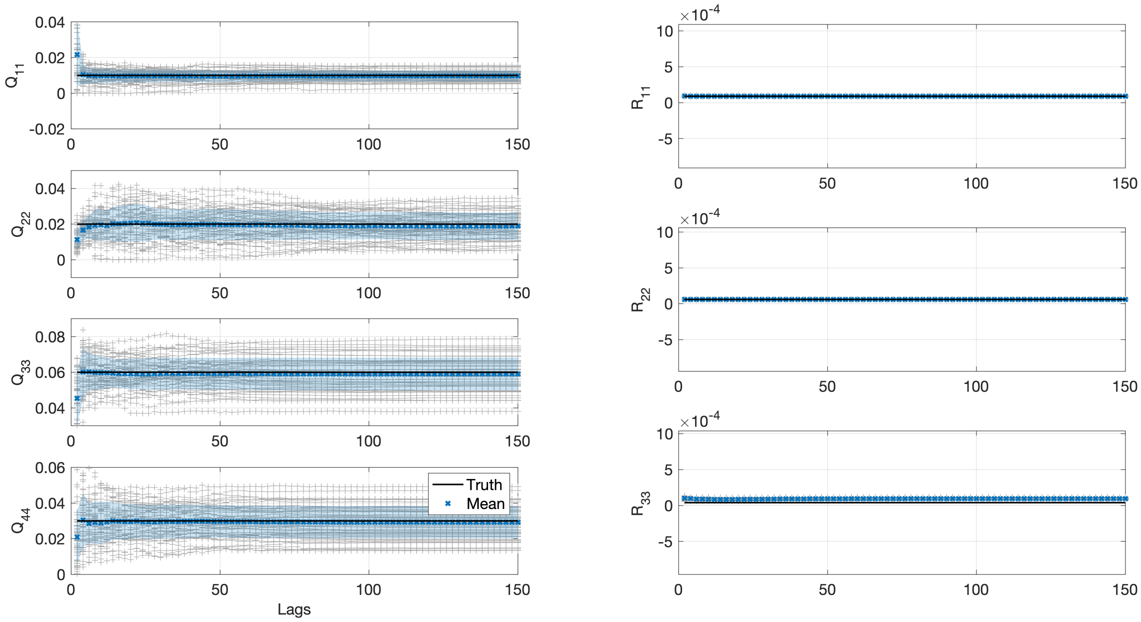

Figure 4.16: β scaled ALS solutions for the diagonal elements of Q_w (left), and R_v (right).

Table 4.4: ALS identified noise covariances for Kirsten Wind Tunnel test-bed: simulation.

	Simulated	Unscaled	β Scaled
Q_{11}	0.0100	0.0610	0.0091
Q_{22}	0.0200	0.0191	0.0189
Q_{33}	0.06	0.0534	0.0591
Q_{44}	0.03	0.0305	0.0292
R_{11}	9.0×10^{-5}	1.3197×10^{-4}	9.0469×10^{-5}
R_{22}	6.0×10^{-5}	1.1157×10^{-4}	6.0068×10^{-5}
R_{33}	4.0×10^{-5}	1.0064×10^{-4}	9.5327×10^{-5}

campaign in the spring of 2021 [82], 29 open loop data sets were collected with the Kirsten Wind Tunnel test-bed. Each data set consisted of a time period of no disturbance followed by a discrete or continuous gust disturbance. The portions of the data with no disturbances were used to identify the process and measurement noise covariance matrices for state estimation. All data were recorded at a dynamic pressure of 10 psf and at an angle of attack at the wing root of three degrees. The wind tunnel data was recorded at 300 Hz and down sampled to 100 Hz for this work to reduce computational load. Several different scale factors, shown in Table 4.5, were evaluated. Generally, the conditioning of the $\mathscr{A}$ matrix improved as the scale factor increased. However for large scale factors the scaled measurement noise became large enough to corrupt the solution. A symptom of this corruption was that one or more of the ALS covariance solutions became zero. Similar to the simulated example, the ALS problem was solved with the quadratic programming approach for 150 lags with each of these scale factors. The identified noise covariances at 150 lags are shown in Figs. 4.17 - 4.19 with error bars representing the standard deviation of the solutions. Figure 4.18 provides a zoomed in view of the fourth diagonal element of the process noise covariance matrix.

Table 4.5: Scaling sets.

Scale Set	Scaling Matrix
1	$diag[10, 100, 1]^{\frac{1}{2}}$
2	$diag[10, 200, 1]^{\frac{1}{2}}$
3	$diag[10, 500, 1]^{\frac{1}{2}}$
4	$diag[10, 1000, 1]^{\frac{1}{2}}$
5	$diag[10, 2000, 1]^{\frac{1}{2}}$

The variance of the solutions of the Q_{22} term increased with increases in the scaling matrix. The Q_{44} solution, shown on the right of Fig. 4.17, was zero for the third - fifth scaling. The variation of the R_v solutions decreased with increases in the scaling matrix. The largest scaling that did not

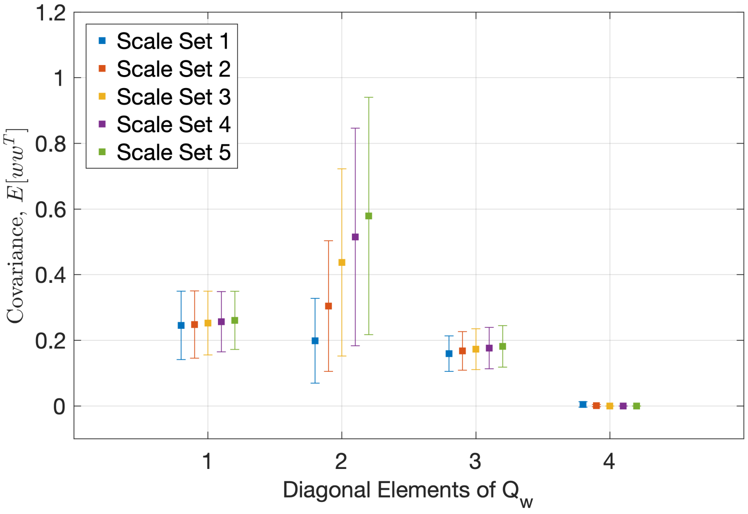

Figure 4.17: Comparison of ALS solutions for scaling sets in Table 4.4: Q_w.

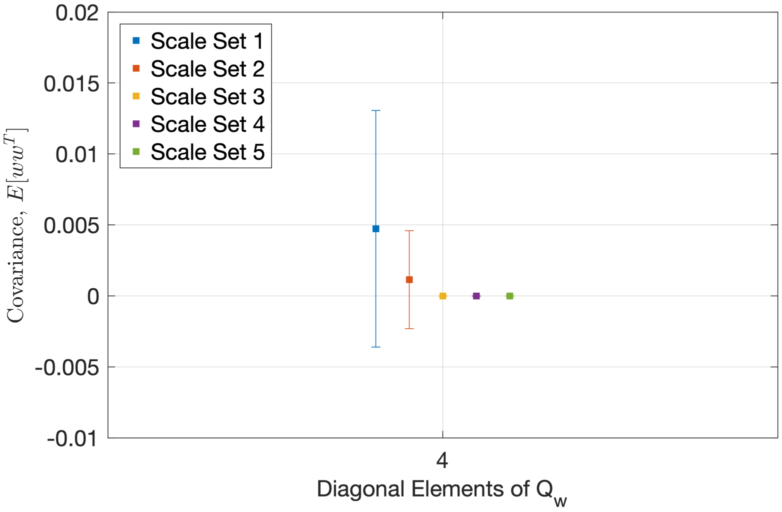

Figure 4.18: Comparison of ALS solutions for scaling sets in Table 4.4: Q_{44} zoomed.

corrupt the solution was selected $\beta = diag(10, 200, 1)^{\frac{1}{2}}$. The identified noise covariances were

$$Q_w = \begin{bmatrix} 0.248 & 0 & 0 & 0 \\ 0 & 0.305 & 0 & 0 \\ 0 & 0 & 0.168 & 0 \\ 0 & 0 & 0 & 0.001 \end{bmatrix} \qquad R_v = \begin{bmatrix} 1.76e-4 & 0 & 0 \\ 0 & 7.52e-05 & 0 \\ 0 & 0 & 1.58e-05 \end{bmatrix}. \tag{4.8}$$

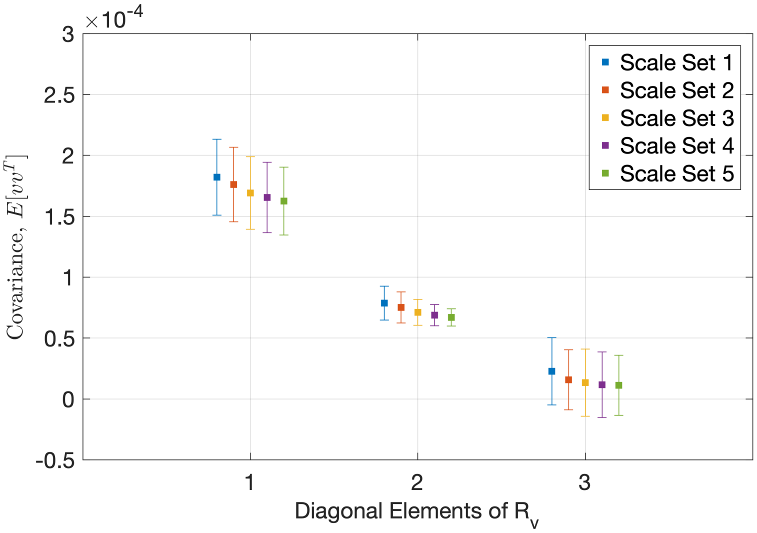

Figure 4.19: Comparison of ALS solutions for scaling sets in Table 4.4: R_v.

4.2.2 Model Uncertainty

It was observed in [82] that the ALS identified process noise covariance was significantly larger when the gust input was at 2.5 Hz, the frequency of the first wing bending mode. This observation led to a hypothesis that there was an error in the modeled damping of the first wing bending mode. Unfortunately, the wind tunnel test had ended and immediately returning to the wind tunnel for system identification testing was not possible due to schedule and budget constraints. To evaluate that model uncertainty, six variations of the state space model were generated corresponding with six first mode damping percentages, $g = [0.5,\ 1.0,\ 1.5,\ 2.0,\ 2.5,\ 3.0]$. The ALS problem was solved for each of the 29 data sets for each of the six damping models. The mean of the ALS solutions for 150 lags are shown in Fig. 4.20 with error bars representing the standard deviation of the solutions. These results showed a change in the first process noise covariance term, Q_{11}, which met expectations due to variation in modeled g for the first mode.

Six Kalman filters were designed with the six model variations and corresponding ALS identified Q_w and R_v matrices. Data from each of the 29 wind tunnel data sets was played through the filters. Using the K-L divergence metric, Eq. (3.21), the performance of estimates was compared in Fig. 4.22 for continuous gust profiles and in Fig. 4.23 for discrete $1 - cos$ gust profiles. The estimate

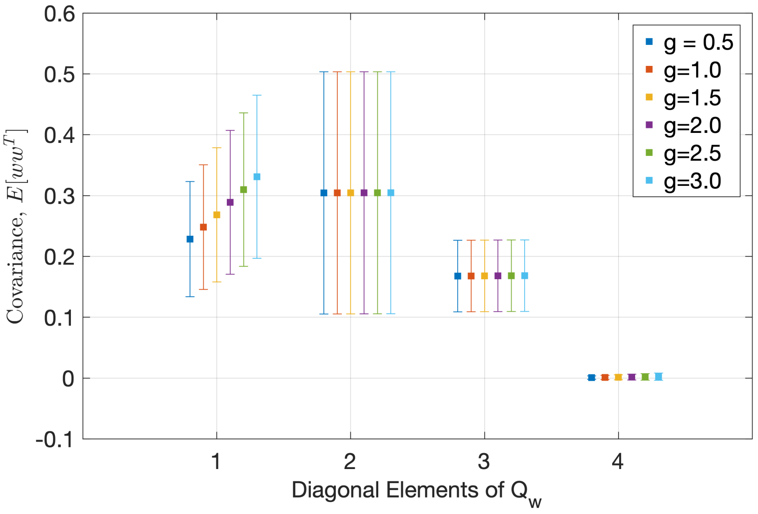

Figure 4.20: Comparison of process noise covariances for modeling error variation.

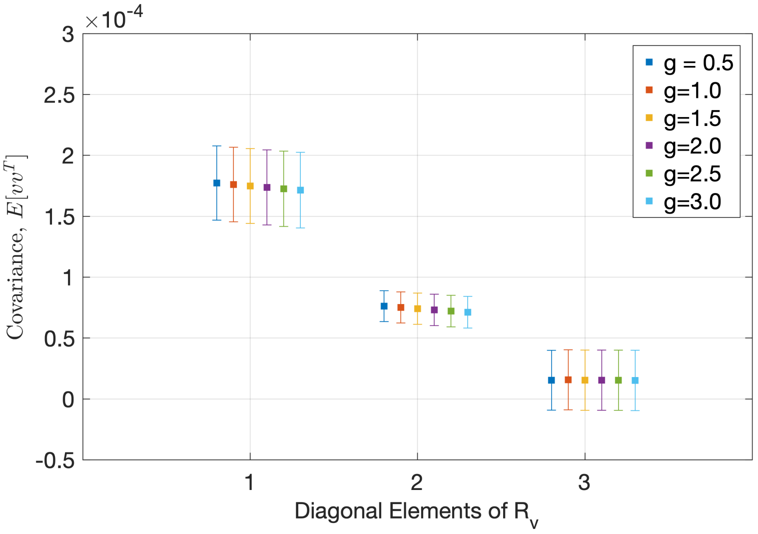

Figure 4.21: Comparison of measurement noise covariances for modeling error variation.

based on the model with $g = 1$ was the best performing estimate, where best was indicated by the lowest E_{opt}, for the range of gust inputs.

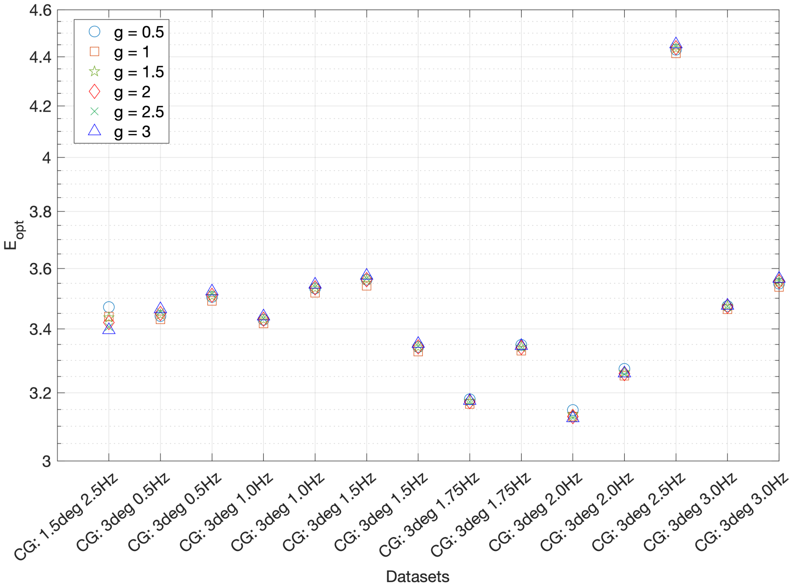

Figure 4.22: Comparison of estimate optimality with modeling error: Continuous Gusts.

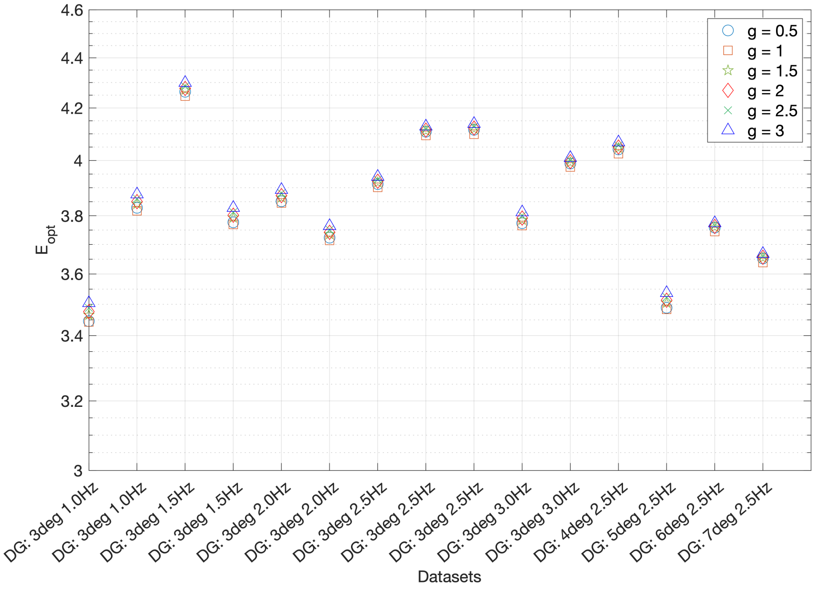

Figure 4.23: Comparison of estimate optimality with modeling error: Discrete Gusts.

4.2.3 Colored Noise Kalman Filter

In the previous subsection, a scaled ALS approach was used to identify Q_w and R_v from wind tunnel data. These data sets were collected with the wind on and no gust or trailing edge flap inputs. Equation (4.5) is modified, as described in Eq. (3.16) and Eq. (3.17), such that the gust is represented as a colored noise disturbance by appending two colored noise states to the estimator,

$$\begin{bmatrix} \hat{x}'(t) \end{bmatrix} = \begin{bmatrix} \dot{\chi}_1'(t) \\ \dot{\chi}_2'(t) \end{bmatrix} = \begin{bmatrix} 0 & 1 \\ \omega_1\omega_2 & -(\omega_1+\omega_2) \end{bmatrix} \begin{bmatrix} \chi_1'(t) \\ \chi_2'(t) \end{bmatrix} + \begin{bmatrix} 0 & 0 \\ 0 & 1 \end{bmatrix} w'(t), \tag{4.9}$$

where $\omega_1 = 0.3\ Hz$ and $\omega_2 = 6\ Hz$ were chosen based on the capabilities of the gust generation system. The control, u_k, was divided into aircraft control surface inputs and atmospheric inputs, $[B]u_k = [B_{cs} \quad B_g][u_{cs} \quad u_g]^T$ and $[D]u_k = [D_{cs} \quad D_g][u_{cs} \quad u_g]^T$. Then B_g became a column of the state-space A matrix to map the augmented gust state to the other states. The process noise identified in Eq. (4.8) was appended with a fifth row and column with the arbitrarily selected value of one for the process noise covariances of the appended colored noise state. The estimate of the second colored noise state, $\mathcal{X}_2$, characterized the atmospheric disturbance. Since the values of G and Q_w for the augmented gust state were arbitrarily selected, the absolute amplitude of the atmospheric estimate was not significant, but it held meaning to relative estimates from other data sets.

This colored noise Kalman filter was evaluated for a variety of gust disturbance data sets. The gust system command was plotted with a 0.12 sec delay to account for the delay in the gust generation system dynamics and the delay in the air flow between the gust generation system and the flexible wing. First, a comparison of the gust system command to gust estimate for five continuous gust data sets is shown in Fig. 4.24. These data sets had a constant command amplitude of 3 deg and increasing frequency (moving down the figure), $[1.0\ Hz,\ 1.5\ Hz,\ 1.75\ Hz,\ 2.0\ Hz,\ 3.0\ Hz]$. The augmented gust state estimate displayed the change in frequency of the input well after an initial convergence. The 1.5 Hz continuous gust exhibited a time shift between the gust command and estimate. It was hypothesized that this was due to inconsistent delay in the gust generation actuation.

In Fig. 4.25, a comparison of the gust system command to gust estimate is shown for four discrete gust data sets. These data sets had a constant frequency of 2.5 Hz and increasing amplitude

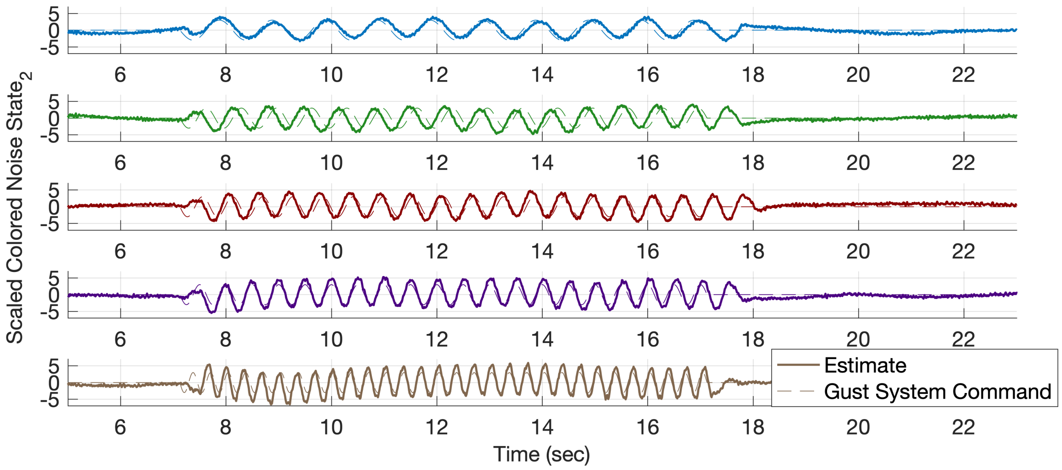

Figure 4.24: Time history of a continuous gust example with colored noise estimator.

[4, 5, 6, 7] deg. The comparison of the gust generation command and colored noise estimate indicated a possible nonlinearity. The 4 degree gust amplitude was under estimated and the 7 degree gust amplitude was over estimated, while the estimates of the 5 and 6 degree gust matched well in amplitude. In the discrete gust estimates comparison, each of the estimates overshot zero in negative direction after the gust. It was hypothesized that this behavior may be an accurate depiction of the disturbance experienced by the flexible wing model. Although the gust vane was commanded to stop at its neutral position, the resulting disturbance in the airflow may have extended in the opposite direction of the original disturbance. A gust profile with similar characteristics, generated by a similar airfoil gust generation system, was measured with a cross hot-wire anemometer in the Swansea University wind tunnel, [95]. These plots show that a colored noise state can be used to observe differences in frequency and amplitude of an atmospheric disturbance with a Kalman filter designed with ALS identified noise covariances.

4.2.4 Time Variant Autocovariance Least Squares

In this section a nonlinear parameter estimation problem is posed for the uncertain damping of the first structural mode. This is an alternative approach to the one taken in Section 4.2.2. Re-framing

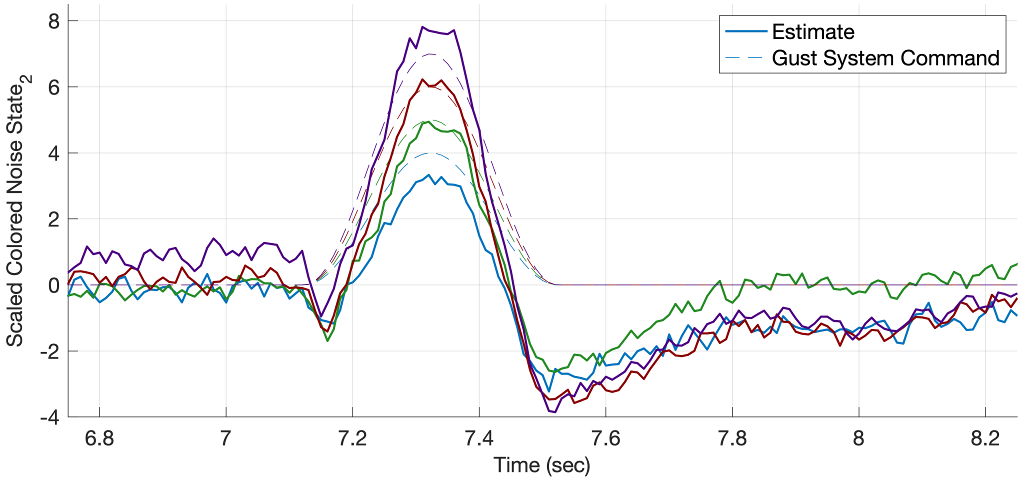

Figure 4.25: Comparison of discrete gust estimates for 4 data sets with 2.5 Hz inputs with amplitudes of 4, 5, 6, 7 deg.

the linear dynamic system from Eq. (4.5) as a nine state nonlinear dynamic system of the form,

$$\begin{aligned} \dot{x}(t) &= f(x(t), u(t), t) + Gw(t) \\ y(t) &= h(x(t), t) + v(t). \end{aligned} \tag{4.10}$$

where the ninth state, x_9, estimates the uncertain damping of the first bending mode of the wing,

$$\begin{aligned} \dot{x}_1(t) &= x_2(t) \\ \dot{x}_2(t) &= A_{21}x_1(t) + x_9(t)x_2(t) + A_{23}x_3(t) + A_{24}x_4(t) + A_{25}x_5(t) + \dots \\ &\qquad \dots + A_{26}x_6(t) + A_{27}x_7(t) + A_{28}x_8(t) + Bu \\ \dot{x}_9(t) &= 0 \end{aligned} \tag{4.11}$$

where A and B are given in Appendix A. The dynamic model of states $x_3 - x_8$ is unchanged from the linear case.

First, a simulated example was considered, where 50 data sets were generated at 100 Hz with the linear equations of motion with $g = 1$. The process and measurement noise covariances were simulated as,

$$Q_w = \begin{bmatrix} 1 & 0 & 0 & 0 \\ 0 & 1 & 0 & 0 \\ 0 & 0 & 1 & 0 \\ 0 & 0 & 0 & 1 \end{bmatrix} \qquad R_v = \begin{bmatrix} 0.001 & 0 & 0 \\ 0 & 0.001 & 0 \\ 0 & 0 & 0.001 \end{bmatrix}. \tag{4.12}$$

In order to improve the conditioning of the autocovariance least squares problem, the outputs were scaled by β as defined in Eq. (4.7). The LTV-ALS problem was solved beginning at time step, $k = 100$ in order to give the Extended Kalman filter time to converge. A sliding window of 50 lags was chosen. The identified noise covariances are shown in Fig. 4.26 and Fig. 4.27.

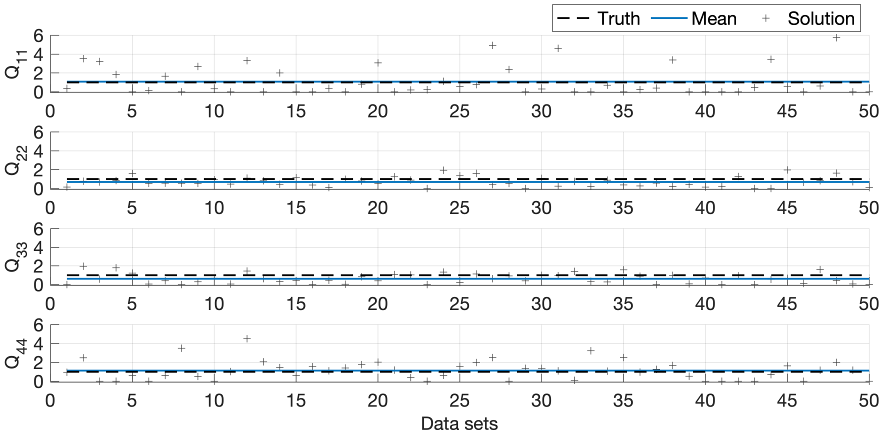

Figure 4.26: β scaled LTV-ALS solutions for the diagonal elements of Q_w: simulated data.

Next, $1 - cos$ discrete gust data sets were used to identify the process and measurement noise covariance from Kirsten Wind Tunnel data sets. There were six of these data sets available with a discrete gust frequency of 2.5 Hz and amplitudes between 3 deg and 7 deg. The discrete gust sets were chosen because an excitation was needed to sufficiently perturb the x_2 state in order to make the x_9 state observable. As the gust response damped out the measurement innovations support LTV-ALS. The LTV-ALS solutions are shown in Fig. 4.28 and Fig. 4.29. The elements of the Q_w

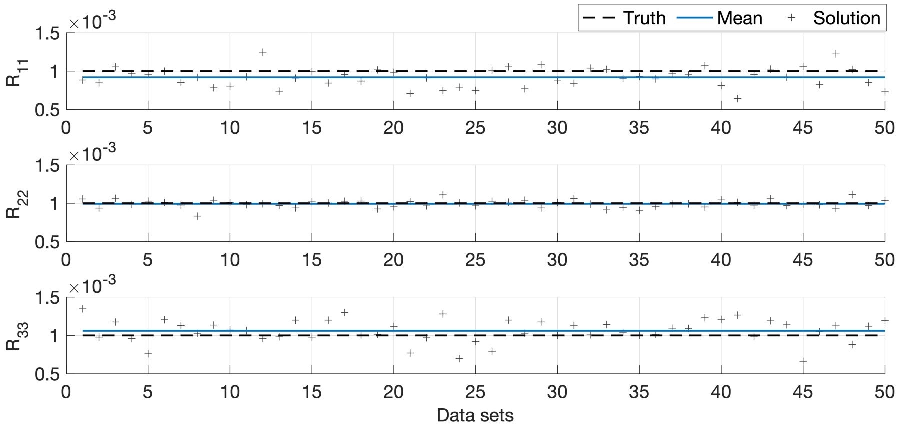

Figure 4.27: β scaled LTV-ALS solutions for the diagonal elements of R_v: simulated data.

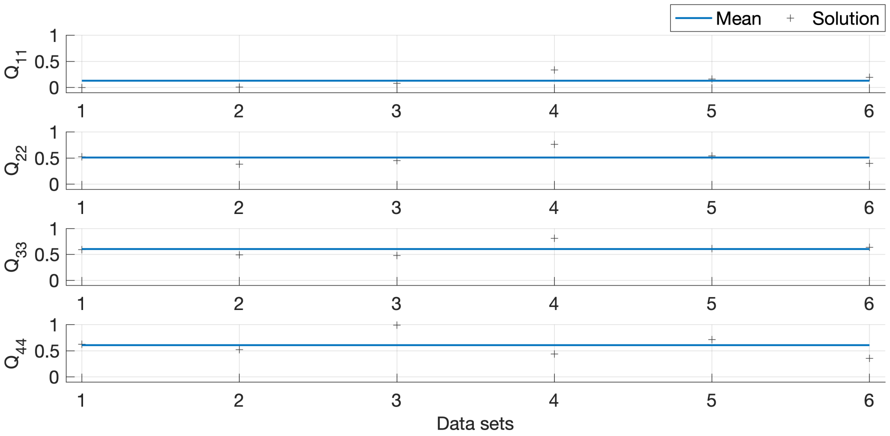

Figure 4.28: β scaled LTV-ALS solutions for the diagonal elements of Q_w: wind tunnel data.

and R_v matrices were chosen as the mean of the LTV-ALS solutions,

$$Q_{wALS} = \begin{bmatrix} 0.1306 & 0 & 0 & 0 \\ 0 & 0.5103 & 0 & 0 \\ 0 & 0 & 0.6048 & 0 \\ 0 & 0 & 0 & 0.6077 \end{bmatrix}$$

$$R_{vALS} = \begin{bmatrix} 4.730 \times 10^{-5} & 0 & 0 \\ 0 & 3.579 \times 10^{-5} & 0 \\ 0 & 0 & 1.777 \times 10^{-8} \end{bmatrix}. \tag{4.13}$$

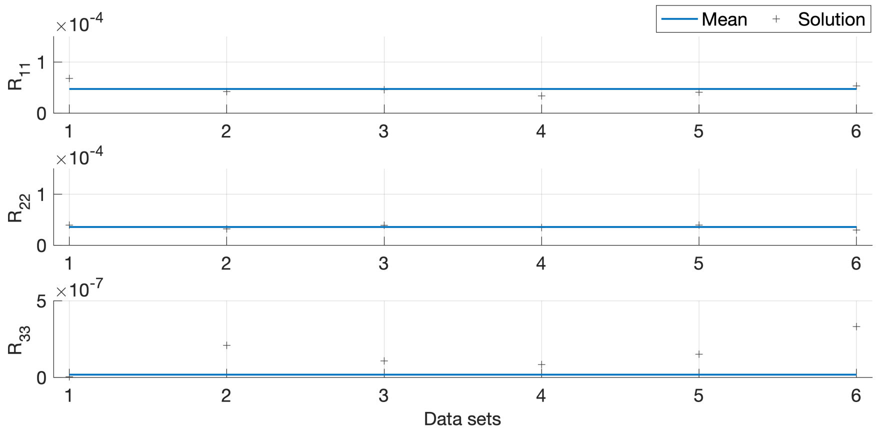

Figure 4.29: β scaled LTV-ALS solutions for the diagonal elements of R_v: wind tunnel data.

The LTV-ALS tuned Extended Kalman filter was compared with three manually tuned Extended Kalman filters,

$$\begin{aligned} EKF_1 &: Q_w = 0.005 \times \mathcal{I}_{4\times 4} \\ EKF_2 &: Q_w = 0.01 \times \mathcal{I}_{4\times 4} \\ EKF_3 &: Q_w = 0.1 \times \mathcal{I}_{4\times 4}. \end{aligned} \tag{4.14}$$

The following parameters were consistent for each of the four Extended Kalman filters,

$$\begin{aligned} Q(5,5) &= 0.01 \\ P(9,9) &= 0.01 \\ R_v &= R_{vALS} \end{aligned} \tag{4.15}$$

The Extended Kalman filter estimates were evaluated for a sustained 2.5 Hz gust with an amplitude of 5 degs. The innovations for the three measurements for each of the Extended Kalman filters are shown in Fig. 4.30. The 3σ error bounds are shown with a black dashed line. The LTV-ALS tuned filter was the closest to satisfying these bounds for the wind tunnel data set. The estimate, $\hat{x}_9$, is shown in Fig. 4.31. The linear model with $g = 1$, which was selected by the K-L divergence method in Section 4.2.2 as the most accurate model, had an $A(2,2)$ term of -2.309 which aligned well with $\hat{x}_9$. All of the Extended Kalman filters converged to similar values. The LTV-ALS tuned Extended Kalman filter estimate has the smallest initial transient and the small oscillations at steady state.

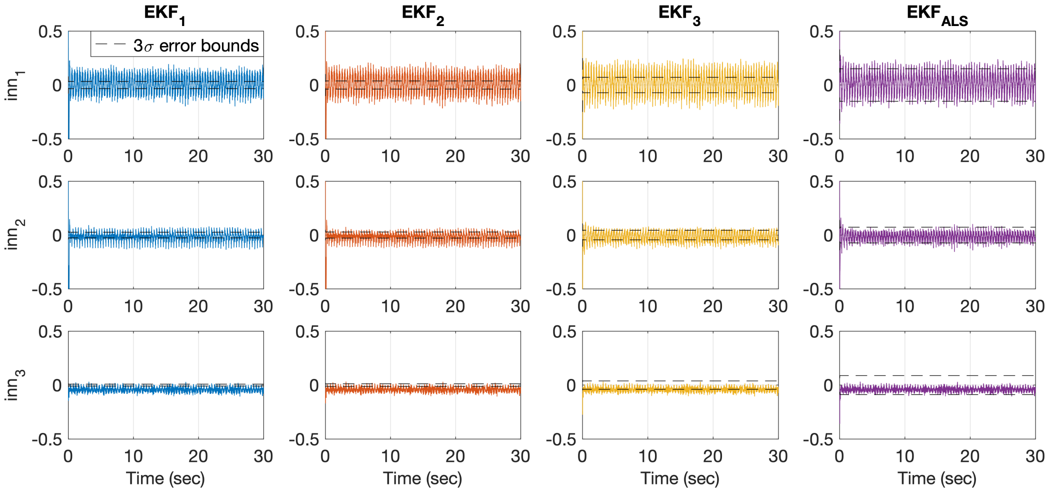

Figure 4.30: Comparison of innovations for 3 Extended Kalman filter designs and the LTV-ALS tuned Extended Kalman filter.

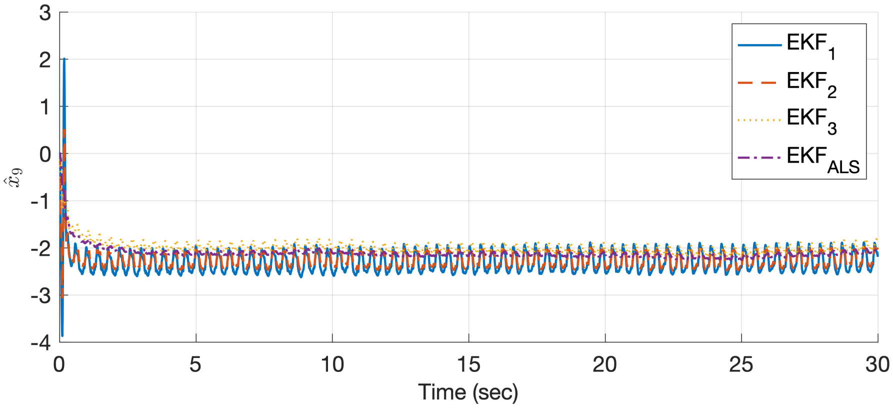

Figure 4.31: Comparison of $\hat{x}_9$ for 3 Extended Kalman filter designs and the LTV-ALS tuned Extended Kalman filter.

In order to compare these filters, the K-L divergence metric was expanded for the time varying case,

$$\begin{aligned}
\Sigma_{tk} =& H_k P_k H_k^T + R_v \\
\Sigma_{mk} =& \frac{1}{N_d}\sum_{i=1}^{N_d} \mathscr{Y}_k \mathscr{Y}_k^T \\
E_{optk} =& \frac{1}{2}(\mathrm{tr}(\Sigma_t^{-1}\Sigma_m) + (\mu_t - \mu_m)^T \Sigma_{tk}^{-1}(\mu_t - \mu_m) - k + \ln\frac{\det(\Sigma_{tk})}{\det(\Sigma_{mk})}.
\end{aligned} \tag{4.16}$$

The E_{opt} for each of the Extended Kalman filters is shown in Fig. 4.32, with the LTV-ALS tuned Extended Kalman filter demonstrating the lowest value.

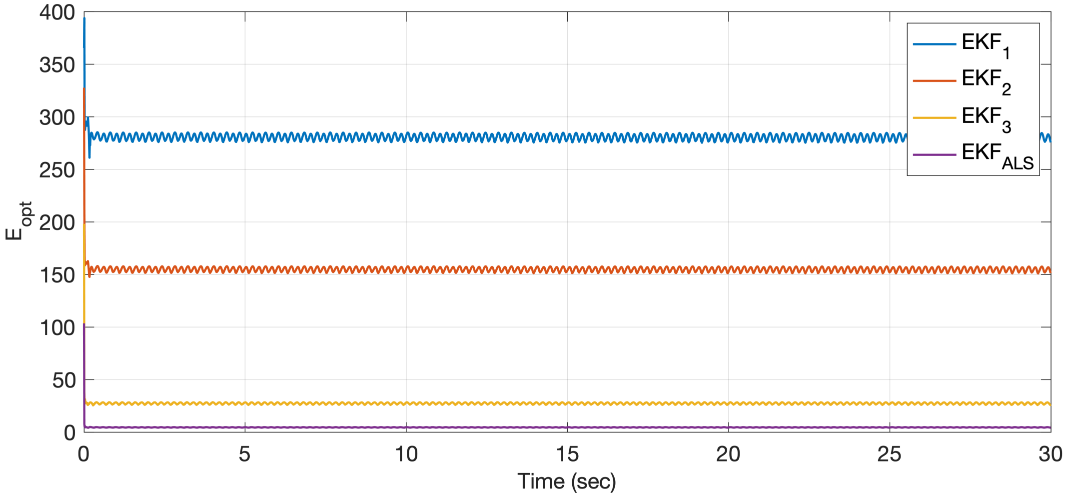

Figure 4.32: K-L divergence metric comparison for 3 Extended Kalman filter designs and the LTV-ALS tuned Extended Kalman filter.

4.3 Model for Aeroelastic Response to Gust Excitation

The Model for Aeroelastic Response to Gust Excitation (MARGE) was developed as a platform to evaluate gust load alleviation control techniques, such as H_∞, [96], and Model Predictive Control, [89], but has also supported other aeroservoelastic studies [91]. The test-bed consisted of a gust generation system, flexible model, and real time active control systems. The flexible model, pictured in Fig. 4.33, was a ceiling mounted, half span, conventional wing-fuselage-tail vehicle. MARGE was free to rotate about its pitch axis. The flexible wing spar was fitted with $3D$ printed *aero-shells* and foam to allow low frequency bending, Fig. 4.34. The flexible mode of interest was the first wing bending mode at 1.45 Hz.

Figure 4.33: MARGE test-bed installed in U. of Washington 3 ft × 3 ft wind tunnel.

The test-bed sensors included a hall effect sensor for pitch rotation, a wing root strain gauge, and wing tip accelerometers. The available controls were two ailerons and an elevator. The wind tunnel supported a range of operating dynamic pressures, $\bar{q}$, enabling test-bed demonstration of maneuvering, gust load alleviation, and active flutter suppression. An analytical model of MARGE based on finite element method and doublet lattice aerodynamics was developed for wind tunnel predictions, [88, 91]. Following wind tunnel data collection, that analytical model was improved using the systems identification software CIFER [97]. The result was a continuous linear state-space models at a range of wind tunnel dynamic pressure operating points following the format,

$$\dot{x}(t) = A_i x(t) + B_i \begin{bmatrix} \delta_{elev}(t) \\ \delta_{ail1}(t) \\ \delta_{ail2}(t) \\ \delta_{gust}(t) \end{bmatrix} + \begin{bmatrix} 0 & 0 \\ 1 & 0 \\ 0 & 0 \\ 0 & 1 \end{bmatrix} w(t), \qquad \begin{bmatrix} \epsilon(t) \\ \theta(t) \\ n_z(t) \end{bmatrix} = C_i x(t) + v(t), \tag{4.17}$$

where $x(t) \in \mathbb{R}^4$, with two rigid body states and two flexible states, and control, $u(t) \in \mathbb{R}^4$, with elevator, inboard/outboard ailerons, and gust. The flexible states were the first wing bending mode

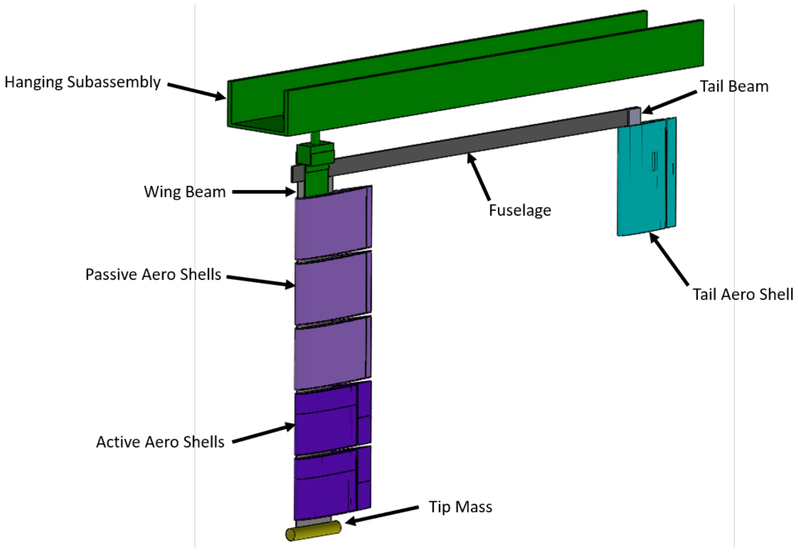

Figure 4.34: MARGE test-bed schematic.

and its derivative. The outputs were strain, ϵ, in units of microstrain, pitch rotation, θ, in units of degrees, and normal acceleration n_z in units of g. The state-space matrices, $[A,\ B,\ C,\ D]$ are provided in Appendix A for a set of dynamic pressure operating conditions.

4.3.1 Ill-Conditioned Autocovariance Least Squares

The MARGE test-bed's linear analytical model was fully observable. However, the standard ALS problem was slightly ill-conditioned. A diagonal scaling matrix,

$$\beta = \begin{bmatrix} 0.02 & 0 & 0 \\ 0 & 500 & 0 \\ 0 & 0 & 10 \end{bmatrix}^{\frac{1}{2}} \tag{4.18}$$

was selected by inspection of the C matrix to improve the ALS problem conditioning as shown in Section 3.1. The initial conditioning is shown in Fig. 4.35 and the improvement in conditioning as a result of the β scaling is shown in Fig. 4.36.

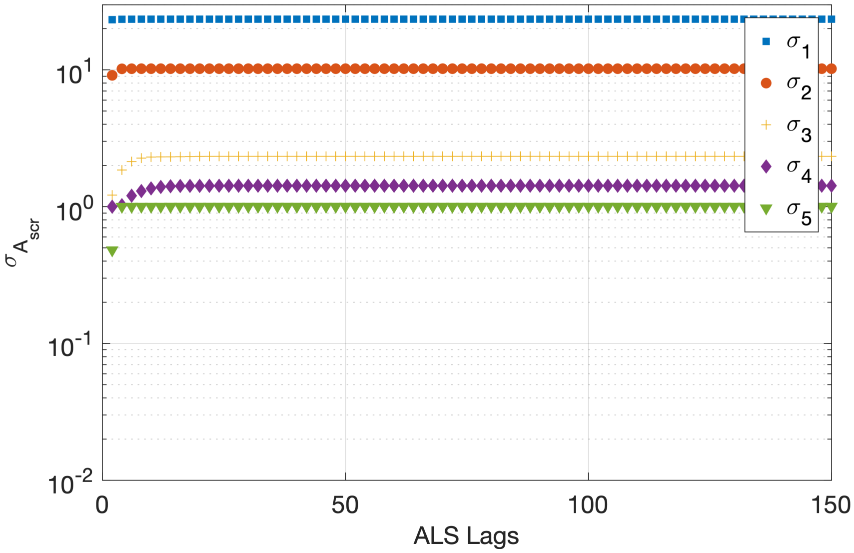

Figure 4.35: ALS singular values, $\sigma_{\mathscr{A}}$: MARGE test-bed.

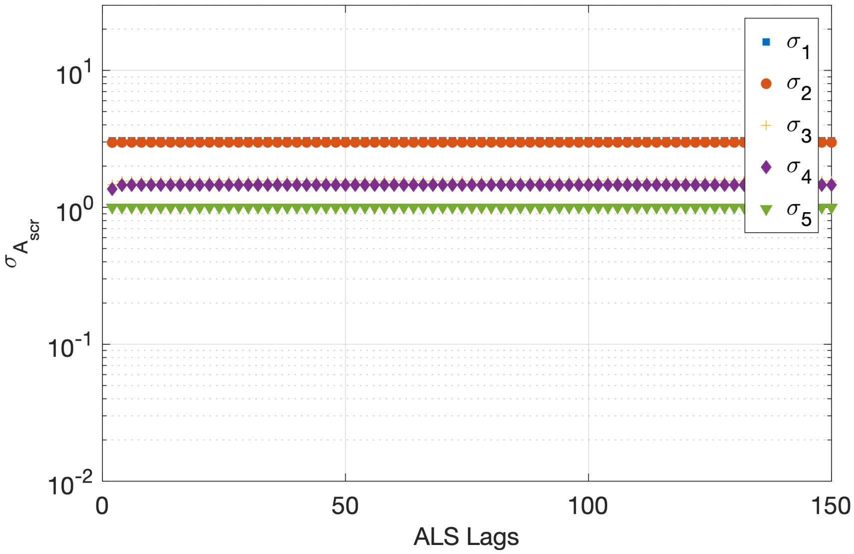

Figure 4.36: Scaled ALS singular values, $\sigma_{\mathscr{A}\beta}$: MARGE test-bed.

4.3.2 Additional Constraints

In order to support state feedback control law demonstrations at each of the 3 ft × 3 ft wind tunnel operating conditions, it was desired to design linear Kalman filters for all of the feasible test conditions. Data were collected at five dynamic pressure operating conditions: $\bar{q} = [166,\ 209,\ 240,\ 281,\ 340]$ Pa. The state-space model matrices are found in Appendix A and [98]. It was observed anecdotally and hypothesized that a major component of the process noise covariance is turbulent flow in the test section. An affine process noise model was proposed as a linear function of dynamic pressure,

$$\begin{aligned} Q_{1i} &= Q_{10} + Q_{1\bar{q}}\bar{q}_i \\ Q_{2i} &= Q_{20} + Q_{2\bar{q}}\bar{q}_i, \quad \forall i. \end{aligned} \tag{4.19}$$

During data reduction, it was observed that the measurements also demonstrated an increase in noise covariance with dynamic pressure. The change in the measurement noise is attributed to the change in operating environment in the wind tunnel. To capture this trend, a structured measurement noise model was also proposed for the measurements,

$$\begin{aligned} R_{1i} &= R_{10} + R_{1\bar{q}}\bar{q}_i \\ R_{2i} &= R_{20} + R_{2\bar{q}}\bar{q}_i \\ R_{3i} &= R_{30} + R_{3\bar{q}}\bar{q}_i, \quad \forall i. \end{aligned} \tag{4.20}$$

Wind tunnel data was collected at 500 Hz and down-sampled to 50 Hz, since the modes of interest are well below 10 Hz. A 25 Hz anti-aliasing filter was applied prior to down-sampling. Different quantities of data were available at each dynamic pressure due to multiple priorities during the wind tunnel test campaign. To balance the ALS problem, 33 equal-length data sets of 4.5 seconds were used at each operating condition. The data set length was chosen because it was long enough to capture the modes of interest while also maximizing the available recorded data. There were no control surface or gust commands issued during or immediately before the data sets. The block diagonal constrained ALS approach, Eq. (3.25), with constraints Eq. (4.19) and Eq. (4.20) was solved with up to 150 lags to identify the elements of noise covariance models. A summary of the 33 constrained ALS solutions is shown in Fig. 4.37. The mean of the constrained solutions is shown with blue ‘o’ and the standard deviation is represented with shading. Truth was unknown for the wind tunnel data. The best knowledge of the noise covariance terms came from solving the single operating condition ALS problem, Eq. (2.10) with all available data, shown by the black dashed line.

Term	Result
Q_{10}	8.9073×10^{-4}
$Q_{1\bar{q}}$	9.3643×10^{-4}
Q_{20}	2.3017×10^{-3}
$Q_{2\bar{q}}$	1.9007×10^{-3}
R_{10}	0.2525
$R_{1\bar{q}}$	0.2590
R_{20}	1.0423×10^{-5}
$R_{2\bar{q}}$	1.2167×10^{-5}
R_{30}	9.6973×10^{-5}
$R_{3\bar{q}}$	6.8783×10^{-5}

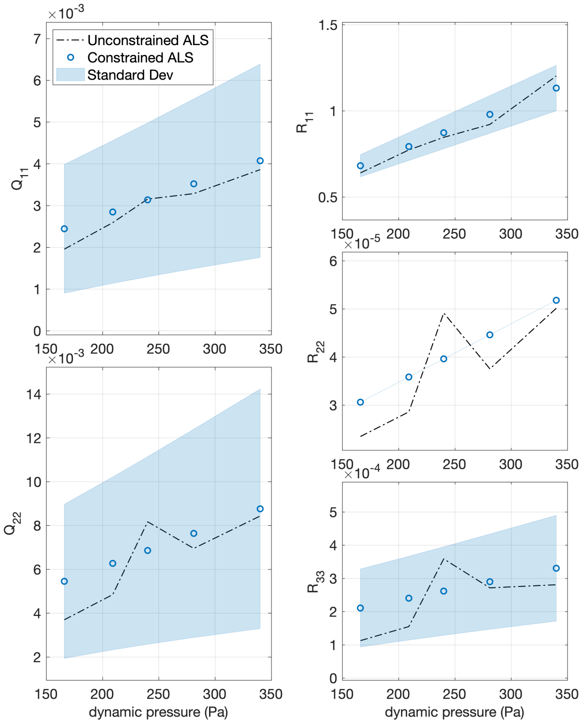

Figure 4.37: Constrained ALS identified noise covariances: MARGE test-bed.

The unconstrained solutions had a positive slope which was approximately linear with a notable outlier at 240 Pa where each of the noise covariance terms was larger than expected given the conditions on either side of it. The constrained solutions aligned reasonably well with the unconstrained solutions. The standard deviations of the constrained solutions encompass the unconstrained solutions for four of the five covariances terms. The change in slope of the unconstrained solutions may be representative of a unmodeled noise characteristic at 240 Pa, however it was hypothesized instead that this was a data quality issue. More data would need to be collected at this dynamic pressure to determine the source of the observed noise covariance. The constrained ALS approach allowed the data collected at other dynamic pressures to influence the solution at 240 Pa.

A set of standard *a priori* recursive Kalman filters, based on the ALS identified Q_i and R_i noise covariance matrices was designed where the state estimate, $\hat{x}_k$, is given by Eq. (1.2). The Kalman filter at one of the design dynamic pressures, 166 Pa is evaluated. The wind tunnel measurements were compared to the measurement estimates, $C\hat{x} + Du$, for a time history with a known $1 - cos$ gust disturbance at 20 seconds, Fig. 4.38. The innovations, $\mathscr{Y}_k$, are shown with the 3σ bounds represented by the black dashed line on the innovation plots, where the expected covariance is $CP^{-}C^{T} + R$. The measurement estimates aligned well with the measurement and the innovations were within the expected bounds.

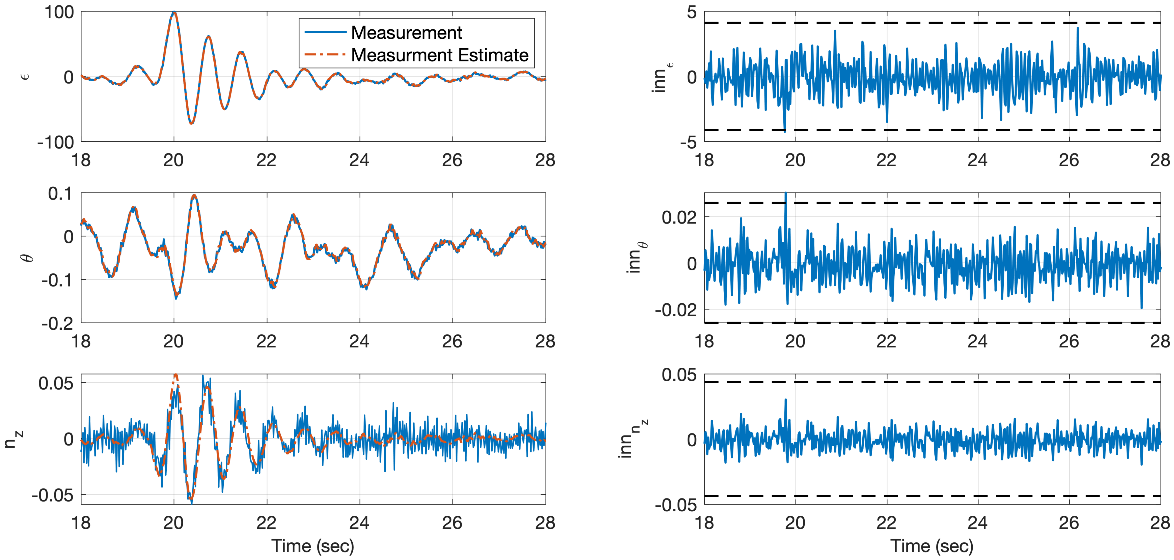

Figure 4.38: $\bar{q} = 166$ Pa: measurement, estimate, and innovations with 3σ error bounds.

Next, a Kalman filter was designed at, $\bar{q} = 268$ kts. This condition was not included in the constrained ALS problem, however it was bounded by the conditions that were. The Kalman gain was chosen by linear interpolation of the values of the Q_i and R_i matrices. This Kalman filter was evaluated on a time history with rapid pulses from each control input. A comparison of the measurement and measurement estimate is shown in Fig. 4.39. The innovations were plotted with the 3σ error bounds and demonstrated good estimate quality.

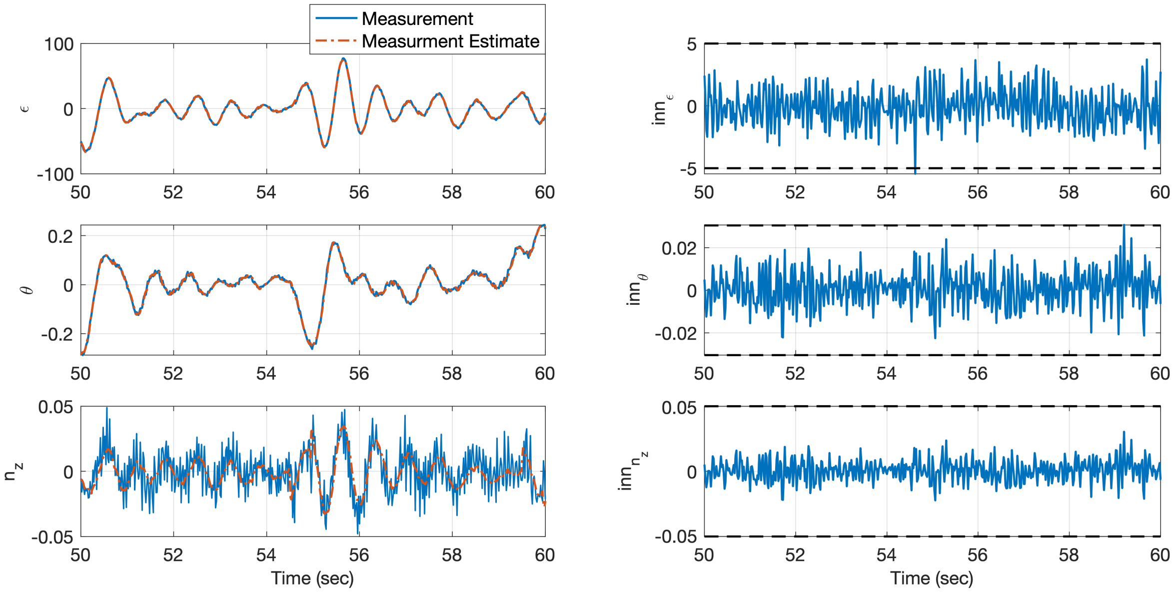

Figure 4.39: $\bar{q} = 268$ Pa: measurement, estimate, and innovations with 3σ error bounds.

4.3.3 Model Uncertainty

Next, the Kalman filter designed for $\bar{q} = 240$ Pa with the constrained noise covariance solution was compared to the Kalman filter designed for the same condition with the unconstrained noise covariance solution. Recall that this was the condition where it was hypothesized that a data quality issue was impacting the solution. The two Kalman filters are compared with the K-L divergence metric, Eq. (3.21).

Eight disturbance profiles were considered, including discrete pulses of the inboard aileron, the outboard aileron, and the elevator, Fig. 4.40. For each data set, the constrained ALS solution was more optimal than the unconstrained ALS solution. This result demonstrated how a constrained ALS approach, utilizing data from across operating conditions, can improve a Kalman filter design.

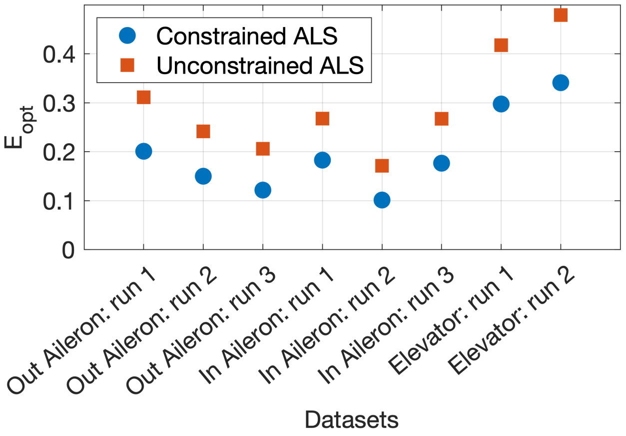

Figure 4.40: K-L divergence metric comparison of constrained and unconstrained ALS solutions: aileron and elevator pulses.

4.4 Wide Body Commercial Aircraft

In this section a conventional wide-body commercial aircraft was used to demonstrate the extension of the colored noise Kalman filter which was applied to the wind tunnel test-bed in Section 4.2 to a fielded aircraft. The flexible dynamics of a commercial aircraft can interfere with pilot workload and handling qualities. While these structural modes are stable without augmentation, they are undesirably lightly damped. The aeroelastic response of aircraft have classically been modeled in the frequency domain with the finite element method and doublet lattice unsteady aerodynamics. The frequency domain unsteady aerodynamics can be converted into a state-space time domain model via a Rational Function Approximation [99, 100, 101, 102, 103]. Typical models for aircraft development would have hundreds of states representing rigid body modes, control surface rigid rotation modes, flexible modes, and unsteady aerodynamics. The model inputs would include each control surface commands as well as atmospheric disturbances.

An observable plant model is necessary for ALS. For the work here, flight test measurements from 18 aircraft sensors were available along the fuselage, wing, and vertical tail as shown in Fig. 4.41, and Table 4.6. The unsteady aerodynamic structural dynamic state model was reduced to be observable with the available sensors. First the unsteady aerodynamic lag states were removed, resulting in a quasi-steady aerodynamic assumption. Next, the model was transformed into a modal realization and states above 12 Hz were eliminated. The resultant model had 106 states and had the form,

$$\begin{aligned} x_{k+1} &= Ax_k + Bu_k + Gw_k \\ y_k &= Cx_k + Du_k + v_k \end{aligned} \tag{4.21}$$

with state, $x_k \in \mathbb{R}^n$, control, $u_k \in \mathbb{R}^m$, process disturbance model, $G \in \mathbb{R}^{n \times g}$, process noise, $w_k \in \mathbb{R}^g$, measurements $y_k \in \mathbb{R}^p$, and measurement noise, $v_k \in \mathbb{R}^p$. The noise, w_k and v_k, was uncorrelated zero-mean, Gaussian white-noise processes with constant covariance matrices, Q_w and R_v. The detailed state-space matrices are proprietary and are not given in this dissertation. Scripts are available in a GitHub repository, [104], for the reader to reproduce the results using the state-space model for the Kirsten Wind Tunnel Large Wing test-bed, [80].

Table 4.6: Flight test measurement locations.

	Location	Sensors
1	Fuselage	lateral acceleration (N_y), normal acceleration (N_z)
2	Fuselage	lateral acceleration (N_y), roll rate (p), yaw rate (r), bank angle (ϕ)
3	Fuselage	normal acceleration (N_z)
4	Fuselage	lateral acceleration (N_y), roll rate (p), yaw rate (r)
5	Fuselage	lateral acceleration (N_y), normal acceleration (N_z)
6	Left nacelle	lateral acceleration (N_y), normal acceleration (N_z)
7	Right nacelle	lateral acceleration (N_y), normal acceleration (N_z)
8	Left wing tip	normal acceleration (N_z)
9	Vertical stabilizer	delta pressure (δ_p)

4.4.1 Ill-Conditioned Autocovariance Least Squares

In order to study the convergence and the conditioning of the ALS problem for the flexible aircraft model considered here, an investigation with simulated data was conducted. Following the simulated

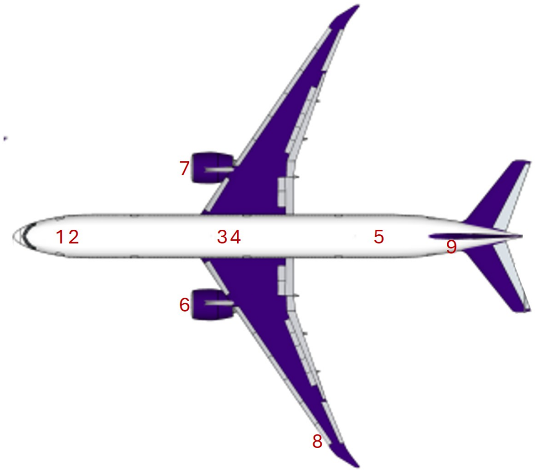

Figure 4.41: Approximate location of sensors from Table 4.6 shown on the Generic Wide Body aircraft [105]. Locations 1, 2, 4, 5, 6, and 7 represent inertial sensing in multiple axes.

data study, the ALS problem was solved with flight test data to identify the process noise covariance, Q_w, and measurement noise covariance, R_v, of the flexible aircraft model in operational flight conditions. The flight test data sets were recorded in smooth air at a single airspeed, altitude, and payload.

Simulated Results

Fifty simulated data sets were created by simulating the reduced plant model as given in Eq. (4.21). The simulated white noise covariances were arbitrarily chosen to be,

$$G = \mathbb{I}^{n\times n}, \qquad Q = \begin{bmatrix} 0.05 & \cdots & 0 \\ 0 & \ddots & 0 \\ 0 & \cdots & 0.05 \end{bmatrix} \in \mathbb{R}^{106\times 106}, \qquad R = \begin{bmatrix} 0.005 & 0 & \cdots & 0 \\ 0 & 0.01 & \cdots & 0 \\ 0 & 0 & \ddots & 0 \\ 0 & 0 & \cdots & 0.09 \end{bmatrix} \in \mathbb{R}^{18\times 18}. \quad (4.22)$$

The ALS problem was solved for each data set for up to $N = 140$ lags. The solutions for the process noise covariance are shown in Fig. 4.42 and for the measurement noise covariance in Fig. 4.43. As discussed in Section 3.1, the standard deviations in the solutions of the

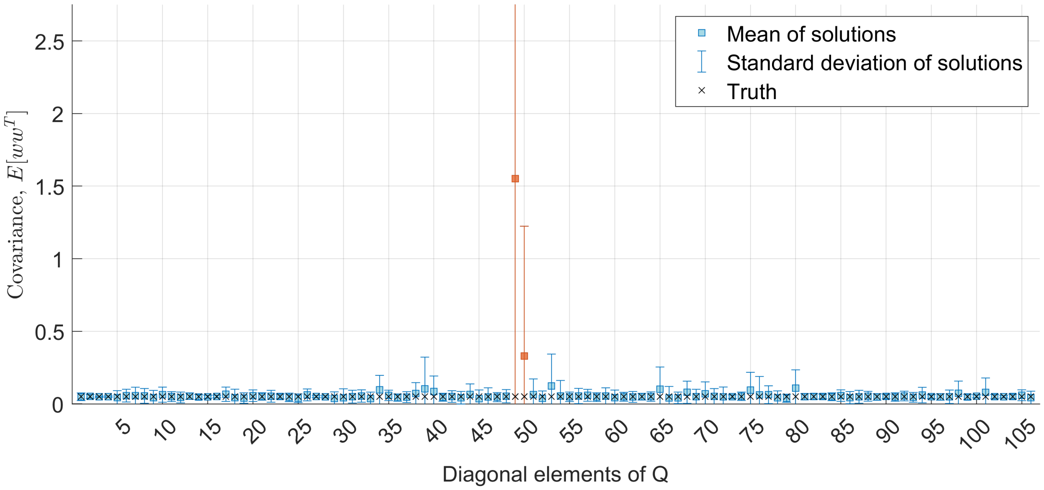

Figure 4.42: ALS identified elements of process noise covariance matrix, Q_w, for 140 lags, simulated data.

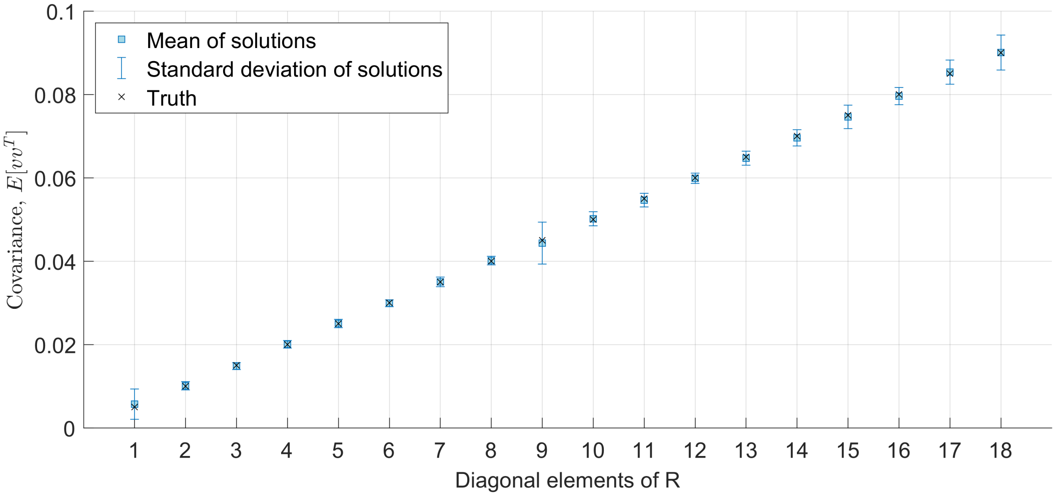

Figure 4.43: ALS identified elements of measurement noise covariance matrix, R_v, for 140 lags, simulated data.

ALS problem were dictated by the singular values, $\sigma_{\mathscr{A}}$, of $\mathscr{A}$. In general, singular values within two orders of magnitude of each other led to a reasonably balanced set of solutions.

The conditioning of an ALS problem improved slightly with increasing lags, N, and could be improved significantly by scaling the outputs through the C matrix. In Fig. 4.44 the singular values of the ALS problem considered here at $N = 140$ lags are shown. The problem was well conditioned, with the majority of singular values falling within 10^2 of each other. There were 19 values that were poorly conditioned, and the expectation was that the corresponding elements of the ALS problem would demonstrate larger standard deviations in their solution sets. The effects of this conditioning is seen in Fig. 4.42, where for the linear case, with simulated white noise, the standard deviation of the ALS solutions is large for the ill-conditioned states. The smallest singular value, shown in red, corresponds with the 49th and 50th elements of Q_w.

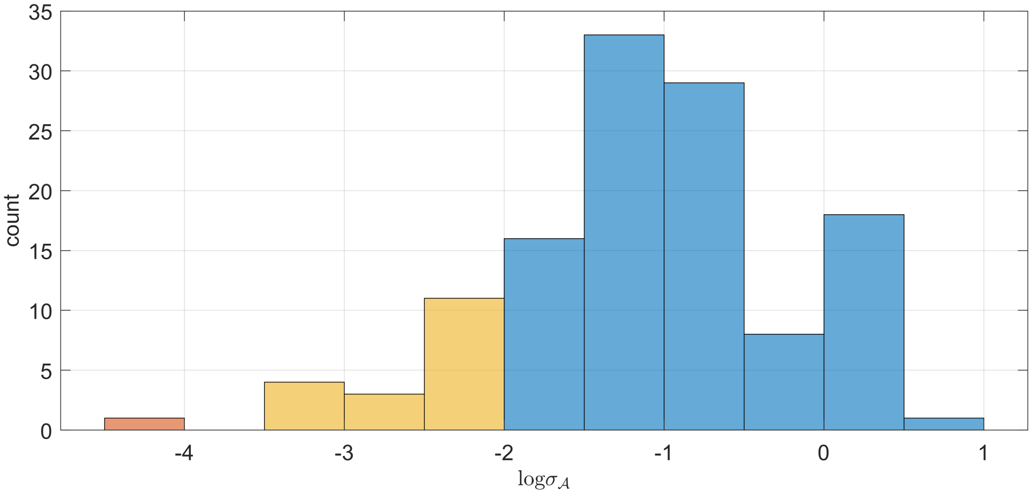

Figure 4.44: Histogram of singular values of $\mathscr{A}$. Poorly conditioned singular values are shown in gold and red.

Flight Test Results

Flight test data was collected during cruising flight through smooth air at a single airspeed, altitude, and payload. Data sets for cruising flight in calm air were selected to identify the noise covariances of the flexible aircraft model during typical flight. The ALS algorithm was solved for 78 sets of flight test data. Each data set was 12 seconds long and recorded at 100 Hz. Data sets were manually selected to remove instances of atmospheric disturbances and maneuvering inputs. The 12 second duration was chosen to maximize available data from flight test by balancing a desire for longer data sets against the prevalence of inputs and disturbances in the recorded data. The ALS problem was solved for each data set for up to $N = 200$ lags. The solutions for the process noise covariance are shown in Fig. 4.45 and for measurement noise covariance in Fig. 4.46.

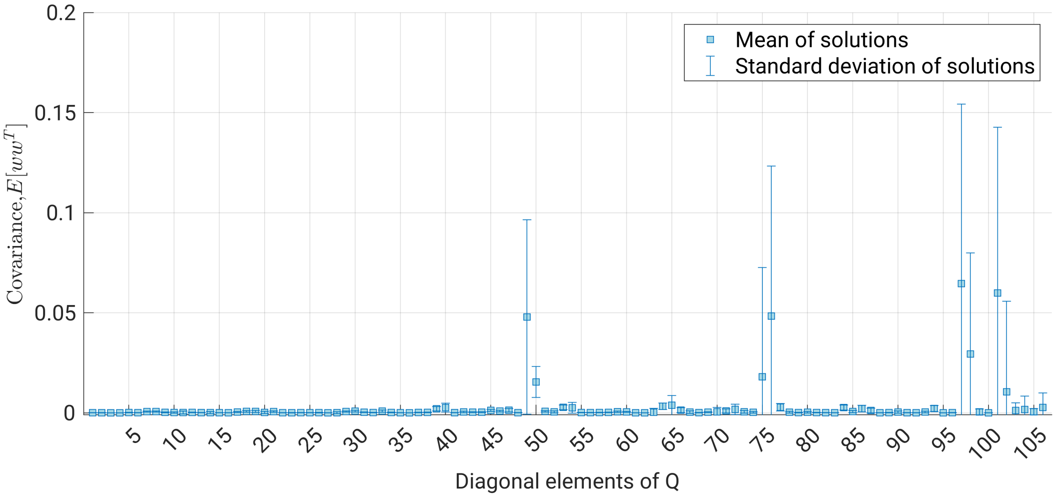

Figure 4.45: ALS identified elements of process noise covariance matrix, Q_w, for 200 lags, flight test data.

As expected from the simulated results and singular value analysis, larger standard deviations were seen in the 49th and 50th states. Additional states showing larger standard deviations in their solution set than the simulated case, [75, 76, 97, 98, 101, 102], were attributed to a combination of:

1. Ill-conditioning of the ALS problem,
2. Inaccuracies between the true dynamics and the reduced order flexible aircraft model

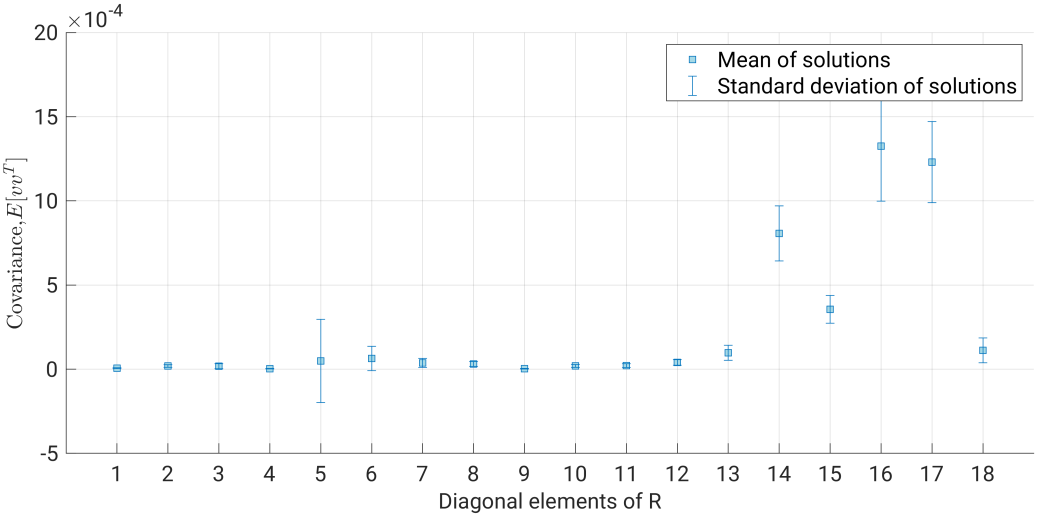

Figure 4.46: ALS identified elements of measurement noise covariance matrix, R_v, for 200 lags, flight test data.

which may include the neglected unsteady aerodynamics, higher frequency modes, or nonlinear equations of motion, and

3. Deviations from the nominal condition in the data sets.

Validation of these results was not possible because the true covariances were unknown, however these results aligned with high level expectation. With the exception of the ill-conditioned states, the process noise covariances had similar magnitude, which was expected due to a consistent dynamic modeling approach. Additionally, the magnitude of the measurement noise covariance terms aligned with expectation of the units for those measurements.

4.4.2 Colored Noise Kalman Filter

An ALS tuned Kalman filter with the colored noise shaping filter, Section 3.2, was used in Section 4.2 to estimate the gust imparted on the Kirsten Wind Tunnel test-bed by a gust generation system. Those results showed promise that this approach could be expanded to fielded aircraft.

Simulated Results

Three Kalman filter designs were compared for the simulated problem:

1. The ideal tuning, using the known simulated noise covariances from Eq. (4.22),
2. The ALS tuning, with identified noise covariances from Fig. 4.42, and
3. The ALS tuned colored noise Kalman filter as described in Eq. (3.17).

The process noise covariance of the augmented state was arbitrarily selected as $Q' = 1$. The measurement and measurement estimates of lateral acceleration at the first fuselage location are shown in Fig. 4.47. Inspection of the time domain results shows that all three Kalman filters performed comparably even though the colored noise Kalman filter did not have an optimal guarantee due to the addition of the random bias shaping filter. The 3σ measurement estimate error bounds of the ideal filter were met as shown by the black dashed line on the innovations plot.

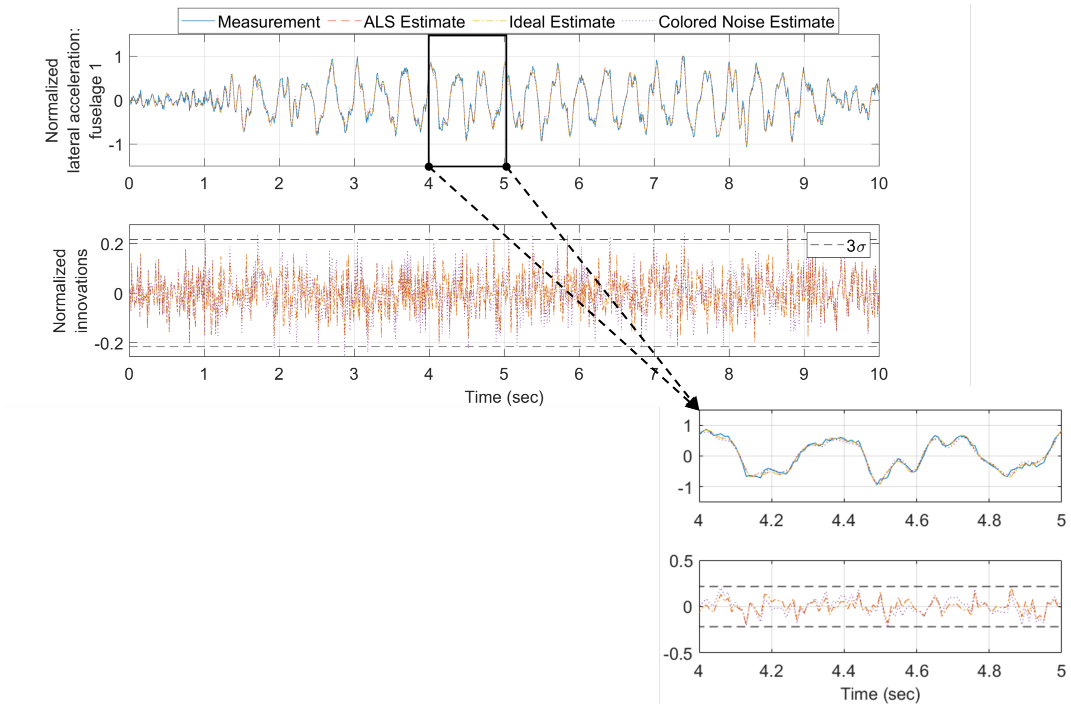

Figure 4.47: Comparison of estimation of n_y at the fuselage location 1, simulated data.

The optimality of the resulting Kalman filters were evaluated using a K-L divergence metric, Eq. (3.21). A comparison of this K-L divergence metric is shown in Fig. 4.48 for the ideal Kalman filter, the ALS tuned Kalman filter, and the ALS tuned colored noise Kalman filter. A smaller E_{opt} indicates an estimate closer to optimal. The E_{opt} of the ALS tuned Kalman filter approaches the E_{opt} of the ideal Kalman filter. However, the loss of optimality with the colored noise Kalman filter is reflected in the K-L divergence metric.

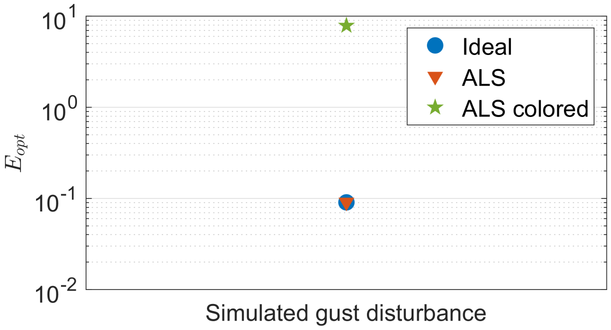

Figure 4.48: Comparison of optimality of estimation, simulated data.

The ALS tuned colored noise Kalman filter approximated the gust input as an augmented state. To assess the ability of this estimation technique to capture frequency and relative amplitude of the disturbance in the augmented state estimate, a 3 Hz sinusoidal gust at three different disturbance amplitudes was evaluated. Fig. 4.49 shows a time domain comparison of the disturbance and estimate of the augmented state. The augmented state estimate captured the amplitude well for all three gust disturbance magnitudes. The augmented state estimate also aligned reasonably well in frequency. There is initial error in the augmented state estimate during the first cycle of the disturbance while the Kalman filter converges.

Flight Test Results

The underlying flight test data used in this analysis are proprietary. The results shared in this section have been normalized and non-dimensionalized.

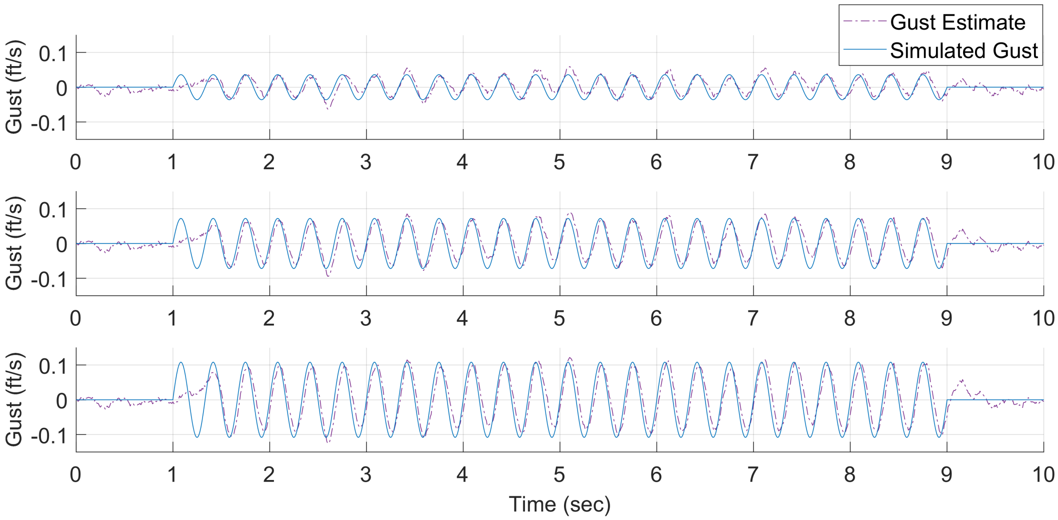

Figure 4.49: Colored noise Kalman filter estimate of the gust disturbance, simulated data.

The flight test data sets required additional considerations, as discussed in Section 4.4.1, including the accuracy of the model used by the Kalman filter as a result of the reduced order modeling, nonlinearities, and continuous to discrete transformations. The flight condition and payload were held approximately constant between the smooth air data collection and the disturbance conditions. The ALS colored noise Kalman filter approach was evaluated with flight test data in two scenarios; first with a known disturbance, then with unknown turbulence.

The first evaluation step considered the ALS colored noise Kalman filter with a known disturbance. The augmented ALS tuned Kalman filter, Eq. (3.16), was modified for a control surface input as the colored noise disturbance. Flight test recorded data from a control surface frequency sweep was played through the augmented ALS tuned Kalman filter to estimate the control surface sweep as an augmented state. This known disturbance case allowed a quantitative comparison between the estimate and a known disturbance. Fig. 4.50 shows that the resulting estimate was able to capture varying frequencies, but underestimated the amplitude of the disturbance with an error that varies with the frequency.

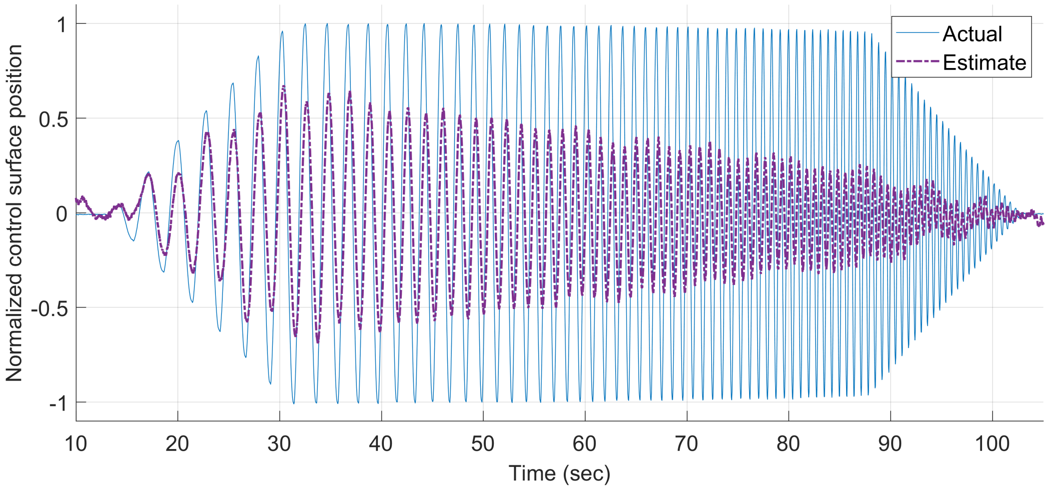

Figure 4.50: Colored noise Kalman filter estimate of the control surface sweep, flight test data.

Next, data sets from 17 passes though moderate turbulence were played through the augmented state ALS tuned Kalman filter in order to estimate the atmospheric gust as the augmented state. These data sets were collected with three different ride quality (RQ) improvement control law techniques. In Fig. 4.51 the power spectral density of the estimated atmospheric gust is compared to the Dryden and von Kármán continuous gust models. As described by Hoblit [53], both models roll off with a sharper knee when compared to experimentally measured gusts. This comparison shows that all of the atmospheric gust estimates contain unexpected frequency content at frequencies where the atmospheric models expected a smoother roll off. This behavior was attributed to the suboptimal performance of the Kalman filter that results from the addition of the augmented state and the reduced order dynamic model.

To compare the performance of the three unique ride quality control techniques, RQ1, RQ2, and RQ3, a fast Fourier transform was used to construct the transfer function from estimated gust to lateral acceleration at fuselage location 1, Fig. 4.52. A successful ride quality

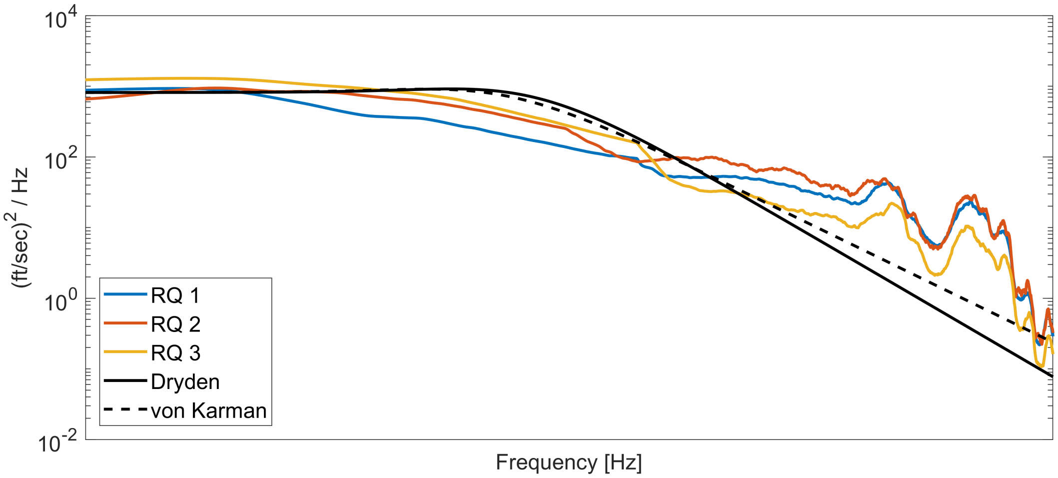

Figure 4.51: Power spectral density of flight test gust estimates, $V = 625$ ft/sec.

control design would reduce the gain of this transfer function at the critical frequencies for human comfort, including pilot fatigue and passenger airsickness. Although the ride quality control approaches were flown in unique atmospheric conditions, quantitative comparisons were possible by using the gust estimate as the transfer function input. Recalling from Fig. 4.49 and Fig. 4.50, the ALS colored noise Kalman filter approach was demonstrated to estimate changes in amplitude at a given frequency. However, the accuracy of the estimate amplitude varied across frequencies. The results showed that each of the ride quality control laws were most effective (smallest gain) in a different frequency range. In a representative region of interest, shaded on Fig. 4.52, RQ1 and RQ2 perform the best. RQ2 shows a notable gain reduction, greater that 5 dB from the other control laws, at the low end of the shaded frequency region.

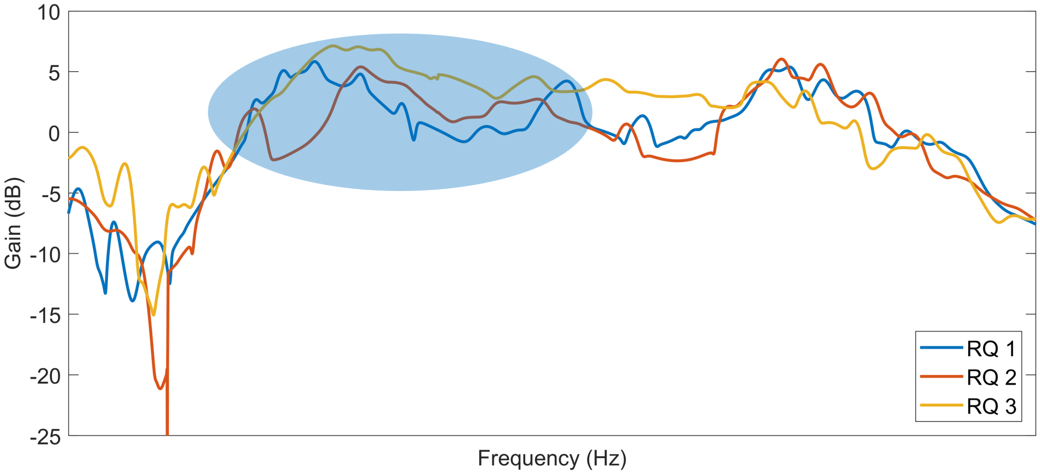

Figure 4.52: Comparison of three ride quality control law approaches. Shading highlights a representative frequency range of interest.

Chapter 5

CONCLUSIONS

In this dissertation four extensions to the ALS problem are introduced and demonstrated. These extensions address shortcomings in the algorithm encountered while identifying noise covariances for aerospace vehicles, however they can be applied to a much larger set of dynamic systems. The extensions improve performance in the presence of:

1. Vehicle dynamics that span a large frequency range,
2. Atmospheric inputs that are challenging to measure,
3. Analytical models that require dedicated system identification data collection, and
4. An operational envelope for which data is difficult or expensive to collect.

The ALS technique is intrinsically tied to the availability of experimental data sets, and as a result its performance is intertwined with the unavoidable realities of imperfect, limited data sets, nonlinear dynamics, and modeling inaccuracies.

The first contribution of this work is the β scaling technique for ill-conditioned ALS problems. This approach was demonstrated on the Kirsten Wind Tunnel Large Wing test-bed and the MARGE test-bed through identification of the noise covariance matrices from wind tunnel data. This technique is necessary when the singular values of the ALS $\mathscr{A}$ matrix span more than 10^2. A β scaling matrix chosen heuristically through inspection of the state-space matrices was shown to effectively increase the accuracy of the ALS solution and enable state estimation. An ideal β to maximally improve conditioning of the generic ALS problem is a topic for future study.

The next contribution combines the improved accuracy of state estimates from the β scaling technique with a colored noise Kalman filter approach for estimating unknown atmospheric disturbances. This extension is demonstrated on the Kirsten Wind Tunnel test-bed and the wide body commercial aircraft. In these applications a colored noise state is appended to the Kalman filter state-space model to estimate the atmospheric disturbances. This technique can be expanded to estimate any unknown input to a dynamic system.

The gust generation system of the Kirsten Wind Tunnel Large Wing test-bed enables a direct comparison between the commanded gust and the gust estimate. The resulting state estimation is presented for discrete $1 - cos$ gusts and continuous sinusoidal gusts at a range of frequencies and amplitudes. The estimates compare well to the commanded gust but also suggest that the commanded vane motion may not be imparting a $1 - cos$ shaped disturbance in the test section.

A Kalman filter tuned with ALS identified covariances and augmented with a colored noise state was used to identify the atmospheric disturbance experienced in flight test. The results demonstrated that while the estimates were suboptimal, they could be used to quantitatively compare control techniques. For the three ride quality control laws considered, relative performance as a function of frequency was assessed. In this application, the ALS technique improved the Kalman filter design and supported the objective to obtain a quantitative estimate of the atmospheric disturbance. These results with a commercial vehicle with flight test data demonstrate that ALS can be successful for aerospace vehicles with a large number of states.

The K-L divergence metric is proposed and demonstrated to quantify the quality of the state estimation for each of the four aerospace platforms discussed. A set of Kalman filters with a parametric variation in the damping of the first wing bending mode are compared for the Kirsten Wind Tunnel Large Wing test-bed. The highest performing estimates were based on the better system model which was shown by a small number for the K-L divergence metric. Through this technique, the analytical model was improved without additional system identification test conditions. This result was reinforced by the LTV-ALS solution when these dynamics are posed as a nonlinear parameter estimation Extended Kalman filter problem.

An expanded ALS problem was derived and solved for the elements of the noise covariance matrices of a system across a set of operating conditions. This approach relies on a designer defined process noise constraint. The constraint serves as a structure for a model of the noise covariance matrices used to determine the Kalman gain. This approach was demonstrated on the MARGE gust load alleviation wind tunnel test-bed. An affine noise covariance model was proposed, and the solutions fit the model well. The performance of the resulting Kalman filters was demonstrated at a condition not used in the ALS problem, but bounded by the condition set. The constrained ALS tuned Kalman filter demonstrated the expected 3σ innovations bounds. A K-L divergence metric comparison of the constrained and unconstrained ALS solution tuned Kalman filter at $\bar{q} = 240$ Pa demonstrated that the constrained ALS approach can be advantageous when there are limited data available or there are data quality concerns.

By expanding the set of problems for which the noise covariance matrices can be identified, these extensions enable accurate state estimation where it was previously challenging or sub-optimal. In turn, accurate state estimates strengthen state feedback control performance and enable decision making based on systems states. In comparison with heuristic tuning for sub-optimal state estimation, the ALS technique can be implemented algorithmically for large state systems with large operating envelopes and solved programmatically. These techniques support the contributions of this dissertation, sensor selection and management, atmospheric disturbance characterization, and model uncertainty.

BIBLIOGRAPHY

[1] J. L. Crassidis and J. L. Junkins, *Optimal Estimation of Dynamic Systems*. Chapman & Hall/CRC Boca Raton, FL, 2 ed., 2011.

[2] R. K. Mehra, "Approaches to adaptive filtering," *IEEE Transactions on Automatic Control*, vol. 17, no. 5, pp. 693–698, 1970.

[3] L. Zhang, D. Sidoti, A. Bienkowski, K. R. Pattipati, Y. Bar-Shalom, and D. L. Kleinman, "On the identification of noise covariances and adaptive Kalman filtering: A new look at a 50 year-old problem," *IEEE Access*, vol. 8, pp. 59362–59388, 2020.

[4] B. J. Odelson, *Estimating disturbance covariances from data for improved control performnace*. PhD thesis, University of Wisconsin-Madison, 2003.

[5] B. J. Odelson, M. R. Rajamani, and J. B. Rawlings, "A new autocovariance least-squares method for estimating noise covariances," *Automatica*, vol. 42, no. 2, pp. 303–308, 2006.

[6] M. R. Rajamani, *Data-based Techniques to Improve State Estimation in Model Predictive Control*. PhD thesis, University of Wisconsin-Madison, 2007.

[7] M. R. Rajamani and J. B. Rawlings, "Estimation of the disturbance structure from data using semidefinite programming and optimal weighting," *Automatica*, pp. 142–148, 2009.

[8] J. Roskam, *Airplane Flight Dynamics and Automatic Flight Controls*. No. p. 1 in Airplane Flight Dynamics and Automatic Flight Controls, Design Analysis and Research Corporation, 1998.

[9] D. K. Schmidt, *Modern Flight Dynamics*. McGraw-Hill New York, 2012.

[10] S. J. Julier and J. K. Uhlmann, "Unscented filtering and nonlinear estimation," *Proceedings of the IEEE*, vol. 92, no. 3, pp. 401–422, 2004.

[11] R. E. Kalman, "A new approach to linear filtering and prediction problems," *Journal of Basic Engineering*, vol. 82, no. 1, pp. 35–45, 1960.

[12] R. E. Kalman and R. S. Bucy, “New results in linear filtering and prediction theory,” *Journal of Basic Engineering*, pp. 95–108, 1961.

[13] M. Avzayesh, M. Abdel-Hafez, M. AlShabi, and S. A. Gadsden, “The smooth variable structure filter: A comprehensive review,” *Digital Signal Processing*, vol. 110, p. 102912, 2021.

[14] “Apollo navigation ground and onboard capabilities,” Technical Report 65-AN-2.0, NASA, Apollo Navigation Working Group, September 1965.

[15] A. Gelb, *Applied Optimal Estimation.* MIT Press, 1974.

[16] T. Kailath, A. H. Sayed, and B. Hassibi, *Linear Estimation.* Prentice Hall, 2000.

[17] F. Lewis, *Optimal Estimation with an Introduction to Stochastic Control Theory.* John Wiley and Sons, 1986.

[18] D. Fraser and J. Potter, “The optimum linear smoother as a combination of two optimum linear filters,” *IEEE Transactions on Automatic Control*, vol. 14, no. 4, pp. 387–390, 1969.

[19] G. M. and E. C. Kerrigan, “Noise covariance estimation for time varying and nonlinear systems,” *The International Federation of Automatic Control*, pp. 9545–9550, 2014.

[20] G. L. Smith, S. F. Schmidt, and L. A. McGee, *Application of statistical filter theory to the optimal estimation of position and velocity on board a circumlunar vehicle*, vol. 135. National Aeronautics and Space Administration, 1962.

[21] H. Heffes, “The effect of erroneous models on the kalman filter response,” *IEEE Transactions on Automatic Control*, vol. 11, no. 3, pp. 541–543, 1966.

[22] T. Nishimura, “Error bounds of continuous kalman filters and the application to orbit determination problems,” *IEEE Transactions on Automatic Control*, vol. 12, no. 3, pp. 268–275, 1967.

[23] R. K. Mehra, “On the identification of variances and adaptive filtering,” *IEEE Transactions on Automatic Control*, vol. 15, no. 2, pp. 175–1184, 1970.

[24] J. Dunik, O. Straka, O. Kost, and J. Havlich, “Noise covariance matrices in state-space models: A survey and comparison of estimation methods - part I,” *International Journal of Adaptive Control and Signal processing*, vol. 31, pp. 1505–1543, 2017.

[25] H. Li and Y.-H. Ni, "Policy optimization of finite-horizon Kalman filter with unknown noise covariance," *arXiv Preprint arXiv:2310.15467*, 2023.

[26] S. Talebi, A. Taghvaei, and M. Mesbahi, "Data-driven optimal filtering for linear systems with unknown noise covariances," *Advances in Neural Information Processing Systems*, vol. 36, pp. 69546–69585, 2023.

[27] S. Talebi, A. Taghvaei, and M. Mesbahi, "Duality-based stochastic policy optimization for estimation with unknown noise covariances," in *2023 American Control Conference*, pp. 622–627, IEEE, 2023.

[28] T. Berry and T. Sauer, "Adaptive ensemble kalman filtering of non-linear systems," *Tellus A: Dynamic Meteorology and Oceanography*, p. 65, 2013.

[29] P. R. Bélanger, "Estimation of noise covariance matrices for a linear time-varying stochastic process," *Automatica*, pp. 267–275, 1974.

[30] C. Neethling and P. Young, "Comments on" identification of optimum filter steady-state gain for systems with unknown noise covariances"," *IEEE Transactions on Automatic Control*, vol. 19, no. 5, pp. 623–625, 1974.

[31] R. Kashyap, "Maximum likelihood identification of stochastic linear systems," *IEEE Transactions on Automatic Control*, vol. 15, no. 1, pp. 25–34, 1970.

[32] N. Gupta and R. Mehra, "Computational aspects of maximum likelihood estimation and reduction in sensitivity function calculations," *IEEE Transactions on Automatic Control*, vol. 19, no. 6, pp. 774–783, 1974.

[33] A. P. Dempster, N. M. Laird, and D. B. Rubin, "Maximum likelihood from incomplete data via the em algorithm," *Journal of the Royal Statistical Society: Series B (methodological)*, vol. 39, no. 1, pp. 1–22, 1977.

[34] R. H. Shumway and D. S. Stoffer, "An approach to time series smoothing and forecasting using the em algorithm," *Journal of Time Series Analysis*, vol. 3, no. 4, pp. 253–264, 1982.

[35] D. T. Magill, "Optimal adaptive estimation of sampled stochastic processes," *IEEE Transactions in Automatic Control*, pp. 434–439, 1965.

[36] C. G. Hilborn and D. G. Lainiotis, "Optimal estimation in the presence of unknown parameters," *IEEE Transactions on Systems Science and Cybernetics*, vol. 5, no. 1, pp. 38–43, 1969.

[37] P. Matisko and V. Havlena, “Noise covariance estimation for kalman filter tuning using bayesian approach and monte carlo,” *International Journal of Adaptive Control and Signal Processing*, vol. 27, no. 11, pp. 957–973, 2013.

[38] K. A. Myers and B. D. Tapley, “Adaptive sequential estimation with unknown noise statistics,” *IEEE Transactions in Automatic Control*, pp. 520–523, 1976.

[39] B. J. Odelson, A. Lutz, and J. B. Rawlings, “The autocovariance least-squares method for estimating covariances: application to model-based control of chemical reactors,” *IEEE Transactions on Control Systems Technology*, vol. 14, no. 3, pp. 532–540, 2006.

[40] M. A. Zagrobelny and J. B. Rawlings, “Practical improvements to autocovariance least-squares,” *AIChE Journal*, vol. 61, no. 6, pp. 1840–1855, 2015.

[41] F. V. Lima and J. B. Rawlings, “Nonlinear stochastic modeling to improve state estimation in process monitoring and control,” *AIChE Journal*, vol. 57, no. 4, pp. 996–1007, 2011.

[42] M. F. Abdel-Hafez, “The autocovariance least-squares technique for gps measurement noise estimation,” *IEEE Transactions on Vehicular Technology*, vol. 59, no. 2, pp. 574–588, 2009.

[43] Z. Gao, C. Cecati, and S. X. Ding, “A survey of fault diagnosis and fault-tolerant techniques—part I: Fault diagnosis with model-based and signal-based approaches,” *IEEE Transactions on Industrial Electronics*, vol. 62, no. 6, pp. 3757–3767, 2015.

[44] A. S. Willsky, “A survey of design methods for failure detection in dynamic systems,” *Automatica*, vol. 12, no. 6, pp. 601–611, 1976.

[45] Federal Aviation Administration, *Advisory Circular: AC No:25.1309-1B*. U.S. Department of Transportation, Federal Aviation Administration: Washington, DC, USA, 2024.

[46] P. M. Frank, “Fault diagnosis in dynamic systems using analytical and knowledge-based redundancy: A survey and some new results,” *Automatica*, vol. 26, no. 3, pp. 459–474, 1990.

[47] K. Hinson and K. Morgansen, “Autocovariance least squares with constrained noise covariance model identification,” in *IEEE Conference on Control Technology and Applications*, 2025 (in press).

[48] S. M. Hoppe, “Gust alleviation using direct gust measurement,” Tech. Rep. 20010014869, National Aeronautice and Space Administration, 2000.

[49] F. Fonte, S. Ricci, and P. Mantegazza, “Gust load alleviation for a regional aircraft through a static output feedback,” *Journal of Aircraft*, vol. 52, no. 5, pp. 1559–1574, 2015.

[50] E. B. Wilson, “Theory of an aeroplane encountering gusts,” *NACA Report*, 1915.

[51] B. Etkin, “Turbulent and wind and its effect on flight,” *Journal of Aircraft*, vol. 18, no. 5, pp. 327–345, 1981.

[52] J. C. Houbolt, R. Steiner, and K. G. Pratt, “Dynamic response of airplanes to atmospheric turbulence including flight data on input and response,” *National Aeronautics and Space Administration*, 1964.

[53] F. Hoblit, *Gust Loads on Aircraft: Concepts and Applications.* American Institute of Aeronautics and Astronautics, 1988.

[54] H. W. Liepmann, “On the application of statistical concepts to the buffeting problem,” *Journal of the Aeronautical Sciences*, vol. 19, no. 12, pp. 793–800, 1952.

[55] F. W. Diederich and J. A. Drischler, “Effect of spanwise variations in gust intensity on the lift due to atmospheric turbulence,” *NACA TN 3920*, 1957.

[56] D. J. Moorhouse and R. J. Woodcock, *Background information and user guide for MIL-F-8785C, military specification-flying qualities of piloted airplanes.* Flight Dynamics Laboratory, 1982.

[57] E. Livne, “Aircraft active flutter suppression: State of the art and technology maturation needs,” *Journal of Aircraft*, vol. 55, no. 1, pp. 410–452, 2018.

[58] R. L. Swaim, “Ride quality flight testing,” *Journal of Guidance and Control*, vol. 1, no. 2, pp. 159–160, 1978.

[59] F. Pradko, R. Lee, and V. Kaluza, “Theory of human vibration response,” in *Proceedings of the 1966 Army Science Conference, United States Military Academy, West Point, NY, 14-17 June 1966*, vol. 2, p. 215, Office of the Chief of Research and Development, 1966.

[60] C. D. Regan and C. V. Jutte, “Survey of applications of active control technology for gust alleviation and new challenges for lighter-weight aircraft,” *National Aeronautics and Space Administration*, 2012.

[61] J. Wykes and A. Mori, "Techniques and results of an analytical investigation into controlling the structural modes of flexible aircraft," in *Symposium on Structural Dynamics and Aeroelasticity*, p. 1140, 1965.

[62] J. B. Dempset and J. I. Arnold, "Flight test evaluation of an advanced stability augmentation system for b-52 aircraft.," *Journal of Aircraft*, vol. 6, no. 4, pp. 343–348, 1969.

[63] D. L. Raney, B. E. Jackson, and C. S. Buttrill, "Simulation study of impact of aeroelastic characteristics of flying qualities of a high speed civil transport," Technical Publication NASA/TP-2002-211943, NASA, Langley Research Center, Hampton VA 23681-2199, USA, October 2002.

[64] M. Idan and S. J. Merhav, "Biodynamic coupling on the human operator model," *Journal of Guidance, Control, and Dynamics*, vol. 13, no. 4, pp. 630–637, 1990.

[65] A. Chakravarty, "Inflight evaluation of a modal suppression yaw damper," in *Guidance, Navigation and Control Conference*, p. 2257, 1987.

[66] J. K. Ho, S. R. Cooper, C. B. Tran, and A. Chakravarty, "On the design of robust compensators for airplane modal control," in *American Control Conference*, no. 24, pp. 397–398, 1987.

[67] D. Gangsaas and U. Ly, "Application of a modified linear quadratic Gaussian design to active control of a transport airplane," in *Guidance and Control Conference*, p. 1746, 1979.

[68] D. Gangsaas, U. Ly, and D. Norman, "Practical gust load alleviation and flutter suppression control laws based on a lqg methodology," in *19th Aerospace Sciences Meeting*, p. 21, 1981.

[69] J. D. Leatherwood, T. K. Dempsey, and S. A. Clevenson, "A design tool for estimating passenger ride discomfort within complex ride environments," *Human Factors*, vol. 22, no. 3, pp. 291–312, 1980.

[70] N. T. Nguyen and K. E. Hashemi, "Multi-objective flight control for ride quality improvement for flexible aircraft," in *AIAA SciTech 2020 Forum*, p. 1623, 2020.

[71] Federal Aviation Administration, *Aviation Weather Handbook (2024): FAA-H-8083-28*. Skyhorse, 2024.

[72] L. B. Cornman, G. Meymaris, and M. Limber, “An update on the faa aviation weather research program’s in situ turbulence measurement and reporting system,” in *11th AMS Conference on Aviation, Range, and Aerospace Meteorology*, 2004.

[73] R. Sharman, L. Cornman, G. Meymaris, J. Pearson, and T. Farrar, “Description and derived climatologies of automated in situ eddy-dissipation-rate reports of atmospheric turbulence,” *Journal of Applied Meteorology and Climatology*, vol. 53, no. 6, pp. 1416–1432, 2014.

[74] P. A. Hunter, C. C. Kraft, and W. L. Alford, *A Flight Investigation of an Automatic Gust-Alleviation System in a Transport Airplane*, vol. 532. National Aeronautics and Space Administration, 1961.

[75] E. H. Teets Jr, C. Ashburn, J. Ehernberger, and R. Bogue, “Turbulence and mountain wave conditions observed with an airborne 2-micron LIDAR,” in *Lidar Technologies, Techniques, and Measurements for Atmospheric Remote Sensing II*, vol. 6367, pp. 179–187, SPIE, 2006.

[76] N. P. Schmitt, W. Rehm, T. Pistner, P. Zeller, H. Diehl, and P. Navé, “The awiator airborne LIDAR turbulence sensor,” *Aerospace Science and Technology*, vol. 11, no. 7-8, pp. 546–552, 2007.

[77] H. Inokuchi, H. Tanaka, and T. Ando, “Development of an onboard doppler LIDAR for flight safety,” *Journal of Aircraft*, vol. 46, no. 4, pp. 1411–1415, 2009.

[78] P. Vrancken, M. Wirth, G. Ehret, H. Barny, P. Rondeau, and H. Veerman, “Airborne forward-pointing uv rayleigh LIDAR for remote clear air turbulence detection: system design and performance,” *Applied Optics*, vol. 55, no. 32, pp. 9314–9328, 2016.

[79] R. Takase, K. Fujita, Y. Hamada, T. Tsuchiya, T. Shimomura, and S. Suzuki, “Robust C* control law design augmented with LIDAR based gust information,” *IFAC PapersOnLine*, vol. 52-12, p. 122–127, 2019.

[80] K. Hinson and K. Morgansen, “Ill-conditioned autocovariance least square noise covariance identification for colored noise gust estimation,” in *AIAA SciTech 2024 Forum*, 2024.

[81] K. Hinson and K. Morgansen, “Estimation of atmospheric disturbances encountered by a large commercial aircraft,” *Journal of Guidance, Control, and Dynamics*, under review.

[82] K. Hinson, K. Morgansen, and E. Livne, “Autocovariance least squares noise covariance estimation for a gust load alleviation test-bed,” in *AIAA SciTech 2022 Forum*, 2022.

[83] K. A. Hinson and K. A. Morgansen, “A flexible wing model uncertainty evaluation based on an autocovariance least squares tuned optimal estimate,” in *American Control Conference*, pp. 2146–2151, IEEE, 2024.

[84] S. Boyd, *Convex Optimization.* Cambridge University Press, 2004.

[85] R. Penrose, “On best approximate solutions of linear matrix equations,” *Mathematical Proceedings of the Cambridge Philosophical Society*, vol. 52, no. 1, p. 17–19, 1956.

[86] Y. Zhang, J. Pan, L. K. Li, W. Liu, Z. Chen, X. Liu, and J. Wang, “On the properties of kullback-leibler divergence between multivariate gaussian distributions,” *Advances in Neural Information Processing Systems*, vol. 36, pp. 58152–58165, 2023.

[87] The Boeing Company, “Boeing ecodemonstrator overview.” `https://www.boeing.com/sustainability/environment/ecodemonstrator#overview`. 02/07/2025.

[88] J. Quenzer, B. Barzgaran, A. Zongolowicz, K. Hinson, M. Mesbahi, K. Morgansen, and E. Livne, “Model for aeroelastic response to gust excitation,” in *AIAA SciTech 2019 Forum*, 2019.

[89] B. Barzgaran, J. D. Quenzer, M. Mesbahi, E. Livne, and K. A. Morgansen, “Real-time model predictive control for gust load alleviation on an aeroelastic wind tunnel test article,” in *AIAA SciTech 2021 Forum*, 2021.

[90] J. Berg, K.-Y. Ting, T. J. Mundt, M. Mor, E. Livne, and K. A. Morgansen, “Exploratory wind tunnel gust alleviation tests of a multiple-flap flexible wing,” in *AIAA SciTech 2022 Forum*, 2021.

[91] J. Berg, K.-Y. Ting, E. Livne, and K. A. Morgansen, “A destabilize/stabilize approach to experimental active flutter suppression technology development,” in *AIAA SciTech 2025 Forum*, p. 1852, 2025.

[92] T. Mundt, “Development of an active aeroelastic continuous trailing edge wind tunnel wing model for drag and gust load minimization,” Master’s thesis, University of Washington, 2019.

[93] N. T. Nguyen, N. B. Cramer, K. E. Hashemi, M. C. Drew, J. Xiong, T. Mundt, M. Mor, and E. Livne, “Progress on gust load alleviation wind tunnel experiment and aeroservoelastic model validation for a flexible wing with variable camber continuous trailing edge flap system,” in *AIAA SciTech 2020 Forum*, p. 0214, 2020.

[94] J. Berg, K.-Y. Ting, M. Mor, and E. Livne, "Test/analysis active control exploration using the university of washington's multiple control surface large flexiblewing," in *AIAA SciTech 2025 Forum*, p. 1854, 2025.

[95] D. Balatti, H. Haddad Khodaparast, M. I. Friswell, and M. Manolesos, "Improving wind tunnel "1-cos" gust profiles," *Journal of Aircraft*, vol. 59, no. 6, pp. 1514–1528, 2022.

[96] K. Ting, M. Mesbahi, and E. Livne, "Aeroservoelastic wind tunnel evaluation of preview h2 and h-infinity gust load alleviation," *Journal of Guidance, Control, and Dynamics*, vol. 46, August 2023.

[97] M. B. Tischler and R. K. Remple, *Aircraft and rotorcraft system identification : engineering methods with flight-test examples.* Reston, VA: American Institute of Aeronautics and Astronautics, 1 ed., 2006.

[98] K. A. Hinson and K. A. Morgansen, "Github: Constrainednoisecovariancemodelid." `https://github.com/uwaa-ndcl/ConstrainedNoiseCovarianceModelId`, 2025.

[99] K. L. Roger, "Airplane math modeling methods for active control design.," *AGARD CP-228, Neuilly-Sur-Seine, France, Defense Technical Information Center DTIC AD A 045242*, pp. 4–1–4–11, 1977.

[100] M. Karpel, "Time-domain aeroservoelastic modeling using weighted unsteady aerodynamic forces," *Journal of Guidance, Control, and Dynamics*, vol. 13, pp. 30–37, 1990.

[101] B. Winther, P. Goggin, and J. Dykman, "Reduced-order dynamic aeroelastic model development and integration with nonlinear simulation," *Journal of Aircraft*, vol. 37, no. 5, pp. 833–839, 2000.

[102] D. K. Schmidt, "Matlab-based flight-dynamics and flutter modeling of a flexible flying-wing research drone," *Journal of Aircraft*, vol. 53, no. 4, pp. 1045–1055, 2016.

[103] M. Karpel and D. J. Neil, "An efficient interdisciplinary rational funciton approximation for closed loop aeroelastic response," in *AIAA SciTech 2024 Forum*, 2024.

[104] K. A. Hinson and K. A. Morgansen, "Estimation-of-atmospheric-disturbances." `https://github.com/kimberhinson/Estimation-of-Atmospheric-Disturbances`, 2025.

[105] J. Quenzer, B. Barzgaran, M. Mesbahi, and K. Morgansen, "The generic wide body aircraft model," in *2018 AIAA Guidance, Navigation, and Control Conference*, p. 0877, 2018.

Appendix A

STATE-SPACE MATRICES

The continuous time linear state-space model matrices for the University of Washington gust load alleviation test-beds are documented in this appendix. They are also available digitally in public repositories on the Nonlinear Dynamic Control Lab GitHub [104, 98].

A.1 Kirsten Wind Tunnel Large Wing test-bed

Kirsten Wind Tunnel test-bed state space matrices, Eq. (4.5), for a dynamic pressure of 10 psf and an angle of attack at the wing root of three degrees.

$$A = \begin{bmatrix} 0 & 1 & 0 & 0 & 0 & 0 & 0 & 0 \\ -254.984 & \eta_1 & -2.063 & -0.224 & -37.729 & 1.016 & 94.512 & -1.132 \\ 0 & 0 & 0 & 1 & 0 & 0 & 0 & 0 \\ -9.050 & \eta_2 & -3332.482 & -1.938 & -3.454 & 0.707 & -25.330 & -0.287 \\ 0 & 0 & 0 & 0 & 0 & 1 & 0 & 0 \\ 45.728 & \eta_3 & 13.709 & 0.814 & -4404.052 & -4.941 & 49.493 & 1.004 \\ 0 & 0 & 0 & 0 & 0 & 0 & 0 & 1 \\ 11.877 & \eta_4 & 23.161 & 0.593 & -41.445 & -1.793 & -21720.471 & -7.546 \end{bmatrix}$$

The change in first wing bending mode damping, shown by η varies across the six models considered,

$$\eta_1 = \begin{bmatrix} -2.165 & -2.309 & -2.453 & -2.596 & -2.740 & -2.884 \end{bmatrix}$$

$$\eta_2 = \begin{bmatrix} 0.295 & 0.295 & 0.295 & 0.295 & 0.294 & 0.294 \end{bmatrix}$$

$$\eta_3 = \begin{bmatrix} 1.537 & 1.536 & 1.535 & 1.535 & 1.534 & 1.533 \end{bmatrix}$$

$$\eta_4 = \begin{bmatrix} 0.074 & 0.073 & 0.073 & 0.073 & 0.073 & 0.073 \end{bmatrix}$$

.

$$B = \begin{bmatrix} 0 & 0 & 0 & 0 & 0 & 0 & 0 \\ -31.242 & -25.703 & -39.958 & -57.023 & -70.761 & -66.991 & -154.309 \\ 0 & 0 & 0 & 0 & 0 & 0 & 0 \\ -22.026 & -19.728 & -25.521 & -23.146 & -11.992 & 1.683 & -59.335 \\ 0 & 0 & 0 & 0 & 0 & 0 & 0 \\ 91.811 & 73.751 & 95.156 & 94.276 & 60.0197 & 4.745 & 282.754 \\ 0 & 0 & 0 & 0 & 0 & 0 & 0 \\ 138.417 & 89.978 & 58.563 & -13.842 & -54.125 & -20.871 & 315.010 \end{bmatrix}$$

$$C = \begin{bmatrix} 4.455 & \lambda_1 & -8.501 & -0.004 & 29.787 & 0.008 & -94.250 & -0.018 \\ 4.312 & \lambda_2 & -6.212 & -0.004 & 20.201 & 0.008 & 30.600 & 0.027 \\ 0.017 & \lambda_3 & 49.587 & 0.025 & 20.401 & 0.012 & 2.720 & 0.001 \end{bmatrix}.$$

The change in first wing bending mode damping, shown by λ, varies across the six models considered,

$$\lambda_1 = \begin{bmatrix} 0.029 & 0.032 & 0.034 & 0.037 & 0.040 & 0.042 \end{bmatrix}$$
$$\lambda_2 = \begin{bmatrix} 0.031 & 0.034 & 0.037 & 0.039 & 0.042 & 0.044 \end{bmatrix}$$
$$\lambda_3 = \begin{bmatrix} -0.002 & -0.002 & -0.002 & -0.002 & -0.002 & -0.002 \end{bmatrix}$$

.

$$D = \begin{bmatrix} 0.500 & 0.318 & 0.292 & 0.314 & 0.654 & 1.127 & 2.168 \\ -0.097 & -0.039 & 0.157 & 0.579 & 1.056 & 1.209 & 0.921 \\ -0.101 & -0.048 & -0.051 & -0.068 & -0.066 & -0.020 & -0.402 \end{bmatrix}$$

A.2 $3\,ft \times 3\,ft$ ***Wind Tunnel MARGE test-bed***

MARGE Wind Tunnel test-bed state space matrices, Eq. (4.17) for the six dynamic pressures.

A.2.1 MARGE state-space matrices for $\bar{q} = 166\ Pa$

$$A = \begin{bmatrix} 0 & 1 & 0 & 0 \\ -31.032 & -2.124 & 7.366 & -0.192 \\ 0 & 0 & 0 & 1 \\ 40.498 & 0.133 & -77.013 & -1.603 \end{bmatrix} \qquad B = \begin{bmatrix} 0 & 0 & 0 & 0 \\ -0.055 & -0.009 & -0.009 & -0.013 \\ 0 & 0 & 0 & 0 \\ 0.001 & 0.023 & 0.017 & 0.084 \end{bmatrix}$$

$$C = \begin{bmatrix} 2256.588 & 0 & 16478.240 & 0 \\ 127.969 & 0 & -0.005 & 0 \\ -6.086 & -0.031 & 11.285 & 0.233 \end{bmatrix} \qquad D = \begin{bmatrix} 0 & 0 & 0 & 0 \\ 0 & 0 & 0 & 0 \\ -0.001 & -0.003 & -0.002 & -0.012 \end{bmatrix}$$

A.2.2 MARGE state-space matrices for $\bar{q} = 209\ Pa$

$$A = \begin{bmatrix} 0 & 1 & 0 & 0 \\ -38.192 & -2.472 & 6.797 & -0.210 \\ 0 & 0 & 0 & 1 \\ 49.321 & 0.090 & -74.464 & -1.906 \end{bmatrix} \qquad B = \begin{bmatrix} 0 & 0 & 0 & 0 \\ -0.076 & -0.013 & -0.013 & -0.012 \\ 0 & 0 & 0 & 0 \\ 0.003 & 0.030 & 0.021 & 0.097 \end{bmatrix}$$

$$C = \begin{bmatrix} 3922.544 & 0 & 17455.676 & 0 \\ 127.969 & 0 & -0.005 & 0 \\ -7.415 & -0.027 & 10.910 & 0.277 \end{bmatrix} \qquad D = \begin{bmatrix} 0 & 0 & 0 & 0 \\ 0 & 0 & 0 & 0 \\ -0.001 & -0.004 & -0.003 & -0.014 \end{bmatrix}$$

A.2.3 MARGE state-space matrices for $\bar{q} = 240\ Pa$

$$A = \begin{bmatrix} 0 & 1 & 0 & 0 \\ -43.009 & -2.523 & 6.412 & -0.222 \\ 0 & 0 & 0 & 1 \\ 57.140 & 0.052 & -73.113 & -2.022 \end{bmatrix} \qquad B = \begin{bmatrix} 0 & 0 & 0 & 0 \\ -0.079 & -0.014 & -0.014 & -0.013 \\ 0 & 0 & 0 & 0 \\ 0.003 & 0.031 & 0.021 & 0.107 \end{bmatrix}$$

$$C = \begin{bmatrix} 4176.552 & 0 & 18192.035 & 0 \\ 127.969 & 0 & -0.005 & 0 \\ -8.583 & -0.022 & 10.710 & 0.294 \end{bmatrix} \qquad D = \begin{bmatrix} 0 & 0 & 0 & 0 \\ 0 & 0 & 0 & 0 \\ -0.001 & -0.005 & -0.003 & -0.016 \end{bmatrix}$$

A.2.4 MARGE state-space matrices for $\bar{q} = 268$ *Pa*

$$A = \begin{bmatrix} 0 & 1 & 0 & 0 \\ -47.360 & -2.569 & 6.064 & -0.232 \\ 0 & 0 & 0 & 1 \\ 64.203 & 0.018 & -71.892 & -2.127 \end{bmatrix} \qquad B = \begin{bmatrix} 0 & 0 & 0 & 0 \\ -0.081 & -0.015 & -0.014 & -0.013 \\ 0 & 0 & 0 & 0 \\ 0.004 & 0.032 & 0.021 & 0.115 \end{bmatrix}$$

$$C = \begin{bmatrix} 4405.979 & 0 & 18857.133 & 0 \\ 127.969 & 0 & -0.005 & 0 \\ -9.639 & -0.017 & 10.530 & 0.309 \end{bmatrix} \qquad D = \begin{bmatrix} 0 & 0 & 0 & 0 \\ 0 & 0 & 0 & 0 \\ -0.001 & -0.005 & -0.003 & -0.017 \end{bmatrix}$$

A.2.5 MARGE state-space matrices for $\bar{q} = 281$ *Pa*

$$A = \begin{bmatrix} 0 & 1 & 0 & 0 \\ -49.380 & -2.591 & 5.903 & -0.237 \\ 0 & 0 & 0 & 1 \\ 67.482 & 0.002 & -71.326 & -2.176 \end{bmatrix} \qquad B = \begin{bmatrix} 0 & 0 & 0 & 0 \\ -0.082 & -0.018 & -0.015 & -0.014 \\ 0 & 0 & 0 & 0 \\ 0.004 & 0.032 & 0.021 & 0.120 \end{bmatrix}$$

$$C = \begin{bmatrix} 4512.498 & 0 & 19165.929 & 0 \\ 127.969 & 0 & -0.005 & 0 \\ -10.129 & -0.015 & 10.447 & 0.316 \end{bmatrix} \qquad D = \begin{bmatrix} 0 & 0 & 0 & 0 \\ 0 & 0 & 0 & 0 \\ -0.001 & -0.005 & -0.003 & -0.018 \end{bmatrix}$$

A.2.6 MARGE state-space matrices for $\bar{q} = 340$ *Pa*

$$A = \begin{bmatrix} 0 & 1 & 0 & 0 \\ -54.778 & -2.800 & 4.514 & -0.307 \\ 0 & 0 & 0 & 1 \\ 87.345 & -0.383 & -68.837 & -2.546 \end{bmatrix} \qquad B = \begin{bmatrix} 0 & 0 & 0 & 0 \\ -0.099 & -0.018 & -0.017 & -0.012 \\ 0 & 0 & 0 & 0 \\ 0.015 & 0.038 & 0.023 & 0.155 \end{bmatrix}$$

$$C = \begin{bmatrix} 5134.129 & 0 & 17929.939 & 0 \\ 127.969 & 0 & -0.005 & 0 \\ -13.059 & 0.040 & 10.076 & 0.370 \end{bmatrix} \qquad D = \begin{bmatrix} 0 & 0 & 0 & 0 \\ 0 & 0 & 0 & 0 \\ -0.001 & -0.004 & -0.003 & -0.014 \end{bmatrix}$$